GA Technologies MASTER

GA-A17267

INERTIAL CONFINEMENT FUSION REACTION CHAMBER AND POWER CONVERSION SYSTEM STUDY

by

I. MAYA, K.R. SCHULTZ, and PROJECT STAFF

SEPTEMBER 1984

DISCLAIMER

GA Technologies

INERTIAL CONFINEMENT FUSION REACTION CHAMBER AND POWER CONVERSION SYSTEM STUDY

by

I. MAYA	D.F. ROELANT***
K.R. SCHULTZ	H.W. SANCHEZ
J.M. BATTAGLIA	S.A. SCHRADER
J.J. BUKSA*	H.L. SCHUSTER
R.L. CREEDON	D.L. SONN
O.D. ERLANDSON	E.O. WINKLER
H.E. LEVINE**	C.P.C. WONG

*Present Address: University of New Mexico
**Present Address: Massachusetts Institute of Technology
***Present Address: University of Michigan

ABSTRACT

A novel concept for the design of an Inertial Confinement Fusion (ICF) reactor called Cascade has been developed by Lawrence Livermore National Laboratory. It utilizes a rotating drum within which the ICF pellet explosions occur. A moving bed of Li_2O, held against the drum walls by the centrifugal force of rotation, serves to breed tritium, capture the fusion energy released, and transport the energy out of the chamber to the power conversion system.

GA Technologies has developed a conceptual ICF reactor system based on the Cascade rotating-bed reaction chamber concept. Unique features of the system design include the use of low activation SiC in a reaction chamber constructed of box-shaped tiles held together in compression by prestressing tendons of $SiC_{/}Al$ composite. This design allows radiative cooling of the chamber and tendons to the vacuum chamber (*i.e.*, active cooling of the rotating chamber is not necessary). Circulating Li_2O granules serve as the tritium breeding and energy transport material, cascading down the sides of the reaction chamber to capture the fusion energy and then transporting this energy out of the chamber to the power conversion system. The total tritium inventory of the system is 6 kg; tritium recovery is accomplished directly from the granules via the vacuum system.

A system for centrifugal throw transport of the hot Li_2O granules from the reaction chamber to the power conversion system has been developed. The granules gravity-flow through the heat exchanger, giving up their heat before returning to the reaction chamber. Two primary side alternatives were explored — Li_2O in vacuum, and Li_2O with helium to improve heat transfer and vacuum locks to isolate the heat exchanger from the reaction chamber vacuum. Both approaches appear viable.

iii

Because of the high Li_2O temperatures, either a steam cycle or a closed cycle gas turbine power conversion system could be used.

A number of issues were evaluated during the course of this study. These include the response of first-layer granules to the intense microexplosion surface heat flux, cost effective fabrication of Li_2O granules, tritium inventory and recovery issues, the thermodynamics of solids-flow options, vacuum versus helium-medium heat transfer, and the tradeoffs of capital cost versus efficiency for alternate heat exchange and power conversion system option. The resultant design options appear to be economically competitive, safe, and environmentally attractive.

CONTENTS

FIGURES

TABLES

1. EXECUTIVE SUMMARY

1.1. INTRODUCTION

Before fusion reactors can move ahead to commercial development, technically sound approaches must be developed that are economicaly competitive, safe, and environmentally attractive. Innovative concepts are needed in many areas to facilitate commercial application. Lawrence Livermore National Laboratory has developed a novel concept for the design of an Inertial Confinement Fusion (ICF) reactor called Cascade (Ref. 1-1). It utilizes a moving bed of solid lithium compound granules, held against the walls of a rotating drum by centrifugal force, to capture and transport the fusion energy. We present here a low activation reaction chamber concept using a circulating solid lithium compound as the tritium breeding and energy transport material, which, applied to the Cascade concept, represents such innovation for ICF reactors.

Circulation of solid breeder granules in structures incorporating low activation materials is fundamental in reaching the above goals. Solid breeders avoid the fire and compatibility hazards associated with liquid lithium systems. Granules are excellent candidates for withstanding the harsh environment of ICF reaction chambers. Unlike static systems that require downtime for the periodic replacement of first walls and other structures that experience radiation and other damage processes, recirculating granules can be replaced online, outside of the reaction chamber. Ceramic lithium compounds have high temperature capability, which in turn leads to high thermal efficiency. Finally, the concomitant use of low activation material brings benefits in reactor safety, maintenance, and waste management, and thus offers the potential for reduced system capital cost.

1-1

This report summarizes the results of the first year of a study to develop new concepts for ICF reaction chambers and power conversion systems. The goal of this program is to develop technically sound designs that are inexpensive, including both capital and operating costs, safe, and environmentally acceptable. Specifically, GA Technologies Inc. (GA) accomplished the following tasks:

- Developed a number of solid breeder reaction chamber concepts, identifying limitations on temperature, heat transfer, efficiency, and materials.

- Determined cost-effective manufacturing methods for solid particle breeding materials.

- Identified and evaluated tritium inventory and recovery.

- Developed concepts for power conversion that included solid particle heat exchangers for either high-temperature gas turbines or steam cycles.

- Developed options for the primary heat transport system, comparing costs of additional plant components against associated gains in efficiency.

1.2. SUMMARY AND CONCLUSIONS

An ICF reaction chamber must absorb the products of the fusion reaction, convert the pulsed energy released into a steady flow of heat at a temperature suitable for the associated power conversion system, and breed new tritium for fuel. A number of solid breeder reaction chambers were considered in this study. The preferred chamber conceptual design is the Cascade rotating-bed chamber concept developed by LLNL, using Li_2O as the solid lithium breeder (Ref. 1-1).

Mechanical Design. The Cascade concept, configured as two conical frustrums attached at their major radii, offers inherent simplicity in the mechanical design and a number of favorable stress characteristics in its structural design. These include

- Low irradiation-induced swelling stresses and materials embrittlement,
- Modest microexplosion-derived forces, and

1-2

- Major load-carrying members can be located externally to the blanket.

The structured design of a ceramic chamber composed of radiatively-cooled SiC tiles held in compression by prestressing SiC/Al composite tendons appears practical. We propose here a low activation chamber constructed of 2 cm thick silicon carbide box-shaped tiles, about 50 cm square and 10 cm high, and held together in compression by longitudinal and circumferential prestressing tendons of SiC/Al composite, 3 cm in diameter. The corners of the box form 15 cm high pylons that act as support for the cables stretched both around and along the chamber. Ceramic SiC can operate at high temperature, avoiding the need for active chamber cooling. It is also very abrasion resistant. The chamber is ringed circumferentially with a pair of 40-cm-deep SiC/Al composite girders that serve both to externally support the chamber and to provide a surface for driving chamber rotation.

The maximum expected chamber stress of 59 MPa is acceptable in comparison to the 200 MPa tensile strength expected in the SiC tiles. Shear stresses are 4 MPa compared to the tiles' 400 MPa rupture stress and 8 GPa critical buckling stress. Tendon dimensions are set by the preload required to maintain the SiC tiles in compression.

The maximum temperatures in the chamber and tendons assuming only radiative cooling to the external vacuum chamber are 860 K and 710 K, within the allowable use temperatures of 1800 K and 800 K for SiC and SiC/Al composite materials, respectively. Thermal insulation is used between the chamber and the tendons to maintain the required tendon temperature.

The capital cost of the ceramic chamber is $9 million compared to $3 million for a metallic chamber. The increase may be justified on the basis of improved abrasion resistance, elimination of active cooling requirements, low activation, and a 30 year life based on radiation damage.

The dynamics of the flowing granule blanket within the chamber are as follows. Basic motion of the blanket is brought about by over-steepening the slope of the

chamber wall with respect to the ~30 deg stability angle of the Li_2O granules. Material is input at the small diameter of the cone-shaped chamber and slides toward the large. The bed of solid breeder granules flows "down" the sides of the chamber toward an exit slot at the chamber equator and issues into a shelf. This would plug the exit slot, stopping the flow. In actuality, a stationary scoop continuously removes material from the rotating exit shelf, allowing for blanket flow continuity.

Granule Design and Fabrication. The first few layers of granules in the blanket, located closest to the fusion energy source, will experience a surface heat flux which might consist of alpha particles, reflected laser light, X-rays, and pellet debris. The intensity of this surface heat flux is such that it is not feasible to avoid melting and vaporization by increasing the size of the chamber. In the limiting case, if the surface heat flux is assumed to deposit at a granule surface (without a deposition profile within the granule), thermal stress contours of Li_2O granules are ten times greater than the fracture strength. Granules would thus crack, partially melt and vaporize, and possibly agglomerate. Experiments are needed to fully characterize the effect. A special surface layer of granules of another material could potentially exhibit improved response to the thermal and stress effects. SiC would be an excellent candidate in such an application due to its factor of seven lower thermal expansion coefficient, factor of ten to twenty greater irradiated fracture strength, and factor of ten greater thermal conductivity compared to Li_2O.

Three processes for the fabrication of lithium oxide granules were identified. The VSM process (Ref. 1-2) is based on melting and spheroidizing irregularly-shaped lithium oxide feed granules. The second process, the lithium hydroxide process, is one patented by Research Dynamics Inc. (Ref. 1-3), which spheroidizes liquified lithium hydroxide, but would use GA's sphere forming technology. The third process is a lithium carbonate sol-gel process proposed herein based on sol-gel technology developed for making spherical fuel particles for the High Temperature Gas-Cooled Reactor (HTGR). Li_2O granule production costs are 170, 50, and 40 \$/kg via the VSM, LiOH, and Li_2CO_3 processes, respectively. All three processes should be cost effective in the

manufacture of the Li_2O granule blanket. Alternate manufacturing techniques must be identified for cost-effective refabrication if surface granules do not maintain their integrity during the fusion pulse.

Tritium. Within the chamber, the granules absorb the neutrons released from laser-induced fusion reactions, producing tritium. The total tritium inventory in the Cascade system is 6 kg. The most important design parameter in determining the inventory is granule size. Granules up to 3 mm diameter would satisfy current fusion safety guidance on tritium inventory (Ref. 1-4). The tritium inventory was found to be relatively insensitive to changes in blanket temperature and porosity, and the background tritium vapor pressure within the reaction chamber. Tritium recovery can be accomplished via the chamber vacuum system. Finally, due to the time scale for tritium diffusion out of a Li_2O granule, the major portion of the inventory is considered secure. Thus, instantaneous release in an accident scenario is not mechanistically possible

Thermodynamics. In addition to breeding tritium, the circulating bed of Li_2O granules serves as the heat generating, transport, and exchange medium. Due to the steep radial heat generation rate, the overall thermodynamic efficiency of the Cascade reactor is very much dependent on the flow distribution and degree of granule mixing within the blanket. Three solid flow options were explored: total mixing, laminar layer, and slug flow with a separate surface layer. Both radial mixing and layered flow control can ideally achieve mixed mean outlet temperatures approaching the 1270 K limit assumed for Li_2O based on LiOT mass transport considerations, but both require developmental work. Slug flow results in a mixed mean blanket outlet temperature of 910 K, assuming a 770 K inlet Li_2O temperature and 1270 K maximum Li_2O temperature. A higher temperature first layer, such as SiC, would result in a higher outlet temperature.

Heat Exchanger Design. The heat exchangers used to recover the energy from the stream of solid Li_2O granules initially flowing in a vacuum are a key feature of

the Cascade power conversion system. Three heat exchanger concepts with helium thermal contact medium appear feasible:

- Immersed-tube fluid bed.
- Direct contact fluid bed.
- Cascade gravity flow.

Fluid-bed heat exchangers with immersed tubes offer relatively high bed-to-surface heat transfer coefficients, very good bed mixing, and fluid-like solids transport capabilities. Smaller granules are preferred. On the negative side, tube abrasion, vibration, and solids dusting can be troublesome for long term power plant operations.

The high effective surface area of a fluid-bed direct contactor is ideal for the transfer of heat from particulate solid to a fluid. However, in the case of solid-to-gas exchange, the large disadvantage in heat capacity of the gas requires high pressure and large frontal area to keep gas velocity sufficiently below the terminal velocity of the particles to maintain a stable fluidized bed. In this case, larger particles are preferred.

Gravity-induced flow of particulate solids over heat exchanger surfaces provides mixing similar to fluidization. The degree of enhancement of the surface-to-wall heat transfer coefficient is dependent for a given particle-gas combination on the average contact time. Cascade flow-splitter type distributors proposed herein can provide relatively short residence times for the hot Li_2O granules while maintaining uniform flow conditions over all surfaces. Furthermore, the concept can operate under vacuum conditions.

The three heat exchangers were evaluated for uniform reference conditions of 1170 K Li_2O inlet to the heat exchanger, 770 K Li_2O outlet, and steam-side conditions similar to the Fort St. Vrain steam generator (Ref. 1-5). The results show that the fluid-bed heat transfer area is not significantly different than in the Cascade gravity-flow with helium heat transfer due to good agitation and short particle contact time in the latter. With vacuum heat transfer the Cascade gravity-flow heat exchanger

requires three times the surface area. The direct contact heat exchanger requires a helium pressure ≥ 5 MPa with a pumping power of approximately 44 MW.

Heat exchanger concepts which involve interstitial helium gas or helium fluidization gas require a transfer lock system through which to pass the Li_2O granules from the high vacuum reaction chamber to the heat exchanger system, and to return the cooled Li_2O to the reaction chamber. Conceptually, a transfer lock for this general function is not particularly unique. However, the very large volume transfer rate required at high proposed operating temperatures presents an interesting challenge. Although the large scale of the system to handle the 2700 kg/s Li_2O mass flow rate required for a 3000 MWt plant is unique, the power requirements are acceptable – 2 to 3 MWe for helium pressures into the 5 MPa range. However, transfer system complexity vis-à-vis a larger but passive heat exchanger may not be justified. It is difficult to evaluate at this time the tradeoffs of increase heat exchanger capital cost versus the potential increase in operating cost which might result from the decrease in reliability associated wih 3-minute-cycle solids gating with gas valving, the large number of pump sets, and other associated equipment.

Granule Transport. The granule transport system provides the interface between the Cascade reaction chamber and the power conversion system. It was determined that the centrifugal acceleration of the reaction chamber rotating at 40 rpm will throw the granules to a height of 10 to 15 m. This would be adequate to transport particles to the elevation required for vacuum heat transfer. With a helium heat transfer medium, the heights dictated by surge tanks, vacuum and pressurizing tanks, pumps, etc., require that the centrifugal throw system be augmented by an additional lift system. Since these systems employ helium gas, this lift function might also be incorporated into its heat transfer enhancement function.

Power Conversion System Comparisons. Though the Cascade concept is inherently simple, it also offers the potential for very high blanket temperatures. It thus can potentially achieve both low cost and high efficiency. We compared the steam

cycle and helium gas turbine cycle options, using capital cost estimates and thermal efficiency to make an overall economic comparison.

For each of these two options we considered the range of outlet temperatures that may be achieved in the Li_2O granule bed. The "moderate temperature" design is based on an upper Li_2O temperature limit of 1270 K and the assumption of flow mixing or flow zoning in the blanket, giving an Li_2O mixed-mean outlet temperature of 1170 K. If flow mixing or zoning is not achieved, we may be limited to a "low temperature" design with 910 K Li_2O average outlet temperature. If higher Li_2O peak temperatures are allowed and excellent flow mixing is achieved, we may be able to use a "high temperature" design with 1400 K average outlet temperature. We have considered low and moderate temperature designs for the steam cycle option, and moderate and high temperature designs for the gas turbine cycle option. In addition, for each of the above combinations, we evaluated the trade-off between vacuum transport of Li_2O through the heat exchangers and helium transport.

To compare the performance of the various options, we included the effects of different capital costs and efficiencies. The results of this economic evaluation are shown on Table 1-1.

A number of interesting and very useful conclusions can be drawn from this preliminary comparison of Cascade power conversion system options. First, relative to the reference option, the use of a helium transport system results in a capital cost savings of $19M. This is at the expense of greatly increased complexity. We believe that detailed design and costing of the vacuum lock system will result in cost increases.

Flow mixing or zoning of the Li_2O increases outlet temperature by 260°C. This is worth $120 to $157M on capital cost and thus is well worth working toward. If flow mixing cannot be achieved it is better to use larger heat exchangers and vacuum transport at a cost of $157M rather than to operate with lower efficiency at an equivalent capital cost of $584M. At the low temperature conditions the relative penalty of using vacuum heat exchangers is increased to $37M. We still believe this penalty is worth the improvement in system simplicity.

TABLE 1-1
CASCADE POWER CONVERSION SYSTEM COST SUMMARY

Option	Efficiency	Additional Capital Cost[a] (Direct + Indirect) ($)	Additional Capital Cost[a] Equivalent of Efficiency ($)	Net Extra Cost[a] ($)
1. Moderate temperature Li$_2$O, moderate temperature steam cycle, vacuum transport (reference)	43%	—	—	—
2. Moderate temperature Li$_2$O, moderate temperature steam cycle, helium transport	43%	-18.5M	0	-18.5M
3. Low temperature Li$_2$O, moderate temperature steam cycle, vacuum transport	43%	+157M	0	+157M
4. Low temperature Li$_2$O, moderate temperature steam cycle, helium transport	43%	+120M	0	+120M
5. Low temperature Li$_2$O, low temperature steam cycle, vacuum transport	34%	0	+584M	+584M
6. Moderate temperature Li$_2$O, moderate temperature, gas turbine cycle, helium transport	42%	+222M	+73M	+295M
7. High temperature Li$_2$O, high temperature gas turbine cycle, helium transport	49%	+303M	-511M	-208M

[a]Relative to reference design

The moderate temperature gas turbine cycle (without a bottoming cycle) results in a small decrease in efficiency and in an increased capital cost due to the need for high temperature materials in the heat exchanger and vacuum lock. This results in a net overall penalty of $295M.

If high temperature can be achieved, the gas turbine system can achieve net thermal efficiencies of 50% to 60%. Effective cost savings of $208M can result. This gives strong incentive to pursue this goal, but the present system concept using a direct contactor and vacuum locks greatly increases system complexity and technical risk.

The moderate temperature, steam cycle, vacuum transport option is simple, uses proven power conversion system materials and technology, and offers reasonably high efficiency. The high temperature gas turbine cycle is exciting and offers the potential for very high efficiency. We recommend that some additional scoping work be done to determine if a self-consistent system can be assembled that uses a SiC blanket layer to get high peak outlet temperatures and ceramic heat exchangers to avoid the need for a vacuum lock system. If this is possible, and if preliminary performance and cost estimates look favorable, the high temperature gas turbine system could make an attractive power conversion system for Cascade. If this is combined with the Cascade rotating-bed reaction chamber using a low activation SiC chamber, we can obtain a reactor design concept that offers the potential to be economically competitive, safe, and environmentally attractive.

References for Chapter 1

1-1. J.H. Pitts, "Cascade: A Centrifugal-Action Solid-Breeder Reaction Chamber," *Nuclear Technology/Fusion*, Vol. 4, No. 2, part 3, September 1983, p. 967.

1-2. R.C. Noren, "Fabrication of Li_2O Microspheres," Personal Communication to H.E. Levine, August 8, 1983.

1-3. J.H. Anno, "Method of Producing Porous Lithium Oxide," U.S. Patent No. 4,221,755 to Research Dynamics, Inc., September 9, 1980.

1-4. M.A. Abdou *et al.* "Blanket Comparison and Selection Study," Argonne National Laboratory Report ANL/FPP-83-1. Vol. II, October 1983, pp. XI-8 through XI-13.

2. SOLID-BREEDER CASCADE REACTION CHAMBER DESIGN

2.1. INTRODUCTION

This section presents the conceptual design of a Cascade ceramic reaction chamber. An ICF reaction chamber must absorb the products of the fusion reaction, convert the pulsed energy released into a steady flow of heat at a temperature suitable for the associated power conversion system, and breed new tritium for fuel. It must be able to withstand the high temperatures and thermal and dynamic stresses imposed by the very high peak energy fluxes inherent in ICF reactors. The chamber should deliver a high blanket outlet temperature and minimize blanket material inventories. These objectives can be accommodated by developing a clever chamber configuration.

The major concerns in designing the reaction chamber are:

- Accommodating the mechanical and thermal stresses from the microexplosion and blanket mass loads.
- Obtaining adequate granule mixing and flow behavior.
- Satisfying material temperature limits and cooling requirements.
- Maximizing the abrasion resistance of the chamber wall material.
- Minimizing structural activation.

These concerns are discussed in the remainder of this chapter.

The design of the chamber requires the integration of the dynamics of solids flow with the mechanical requirements imposed on the structure. The principal considerations are presented in Section 2.2. The thermal analysis of the chamber is presented in Section 2.3. Section 2.4 presents the thermodynamic analysis of the effect of different

chamber designs on the system efficiency. Section 2.5 discusses preliminary consider-
ations of the constraints which determine the maximum allowable temperature with
Li$_2$O granules as the tritium breeder and energy transport material.

2.2. MECHANICAL AND STRUCTURAL DESIGN

2.2.1. Introduction

The Cascade rotating-bed chamber concept (Ref. 2-1) offers inherent simplicity
in the mechanical design of the reaction chamber and a number of favorable stress
characteristics in its structural design. First, a major advantage over most reactors
operating in a radiation environment is that the structure sees only approximately 1%
of the neutron flux. The benefit is that concerns such as swelling-induced stresses and
radiation embrittlement are minimized. Second, with a 50% porosity solid-breeder
blanket, the microexplosion-derived pressure pulse imposes only modest forces on the
structural shell (Ref. 2-2). Third, the shape-deflecting blanket mass loads and grav-
ity and centrifugal forces can be carried by major roller structural supports located
externally to the blanket. A summary of Cascade reactor reference parameters are
shown in Table 2-1.

The mechanical design of the chamber is influenced by the flow mechanics of its
contents. The shape of the chamber itself is influenced by the stability angle (or angle
of repose) of the blanket material within. The necessity for internal structure, such as
vanes, multiple feed points or exit orifices and mechanisms for agitation is influenced
by the degree of granule mixing required for maximizing the outlet temperature.
These influences must be integrated into the chamber design.

In this section, we present the selected reaction chamber design and the major
factors contributing to the design choices.

2-2

TABLE 2-1
REFERENCE CASCADE REACTOR DESIGN PARAMETERS

Fusion power	3000 MW
Pellet energy yield	600 MJ
Frequency	5 Hz
Chamber rotational speed	40 rpm
Blanket	
Material	Li_2O granules
Granule diameter	1 mm
Mass	2×10^5 kg
Porosity	50%
Mass flow rate	2700 kg/s
Inlet temperature	770 K (500°C)
Outlet temperature	1170 K (900°C)

2.2.2. Chamber Structural Design

Overview. A number of solid breeder reaction chambers were considered in this study and are presented in Section 2.2.3. The preferred chamber conceptual design is shown in Fig. 2-1. It is a shell of revolution about a horizontal axis. Its shape is dependent upon experimental investigation of the internal material flows, but is presently configured as two attached conical frustrums of 5 m major radius, 2 m minor radius, and 10 m total length (i.e., a 30% half-angle). At each small end, a hole centrally disposed about the axis admits the solid breeder blanket material in the form of granules, the fusion pellet, and the laser beams. Centrifugal force allows the granules to rotate with the reaction chamber, slide toward the outlet slots, and exit to the power conversion system.

We propose here a low activation chamber constructed of 2 cm thick silicon carbide (SiC) box-shaped tiles (Fig. 2-2), about 50 cm on a side, and held together in compression by 3 cm longitudinal and circumferential prestressing tendons of SiC/Al

3 cm DIA ALUMINUM COMPOSITE
TENDON NET

40 cm AL RING GIRDER

INSULATING POSTS

INSULATION COVER

PRESTRESSED
CERAMIC (SiC) SHELL
5 m MAJOR RADIUS
2 m MINOR RADIUS
10 m TOTAL LENGTH

OPENING FOR
FUEL PELLETS,
LASER BEAM AND
LI_2O PARTICLE FEED

PARTICLE OUTLETS

SUPPORT ROLLERS (24)

Fig. 2-1. Ceramic Cascade reaction chamber. SiC shell is prestressed and held in compression with Al-SiC composite tendons. (Solid-breeder granule blanket is contained with the shell but is not shown in this view.)

SiC–AI COMPOSITE TENDONS
3.0 cm DIA. (SiC FIBERS IN AI MATRIX)

10 cm HEIGHT
SIDE FLANGE

15 cm HEIGHT
CORNER POST

REAR OF PANEL IS
THERMALLY INSULATED
TO PROTECT TENDONS

REGISTRATION

FACES BEDDED
IN GREEN SiC

2 cm THICKNESS SiC
PANEL, 50 cm X 50 cm

CHAMBER STRUCTURE DETAIL

SPECIAL TILE
AT GIRDER

INSULATION

INSULATION
POSTS

40 cm DEEP ALUMINIUM
COMPOSITE RING GIRDER

GIRDER DETAIL

Fig. 2-2. SiC panel and girder details.

composite. Ceramic SiC can operate at high temperatures, thus avoiding the need for external cooling and achieves the goal of minimal neutron activation. It is also very abrasion resistant. The bottom of the boxes form the chamber wall and are positioned to collectively achieve the desired chamber shape. The sides of each box (10 cm high) form faces which butt against one another. The joints between them include a compliant bond, possibly an uncured ceramic compound that is fired during operation to form a permanent joint.

The corners of each box are higher (15 cm), forming a pylon that acts as a support for the cables stretched both around and along the chamber. This creates a net that can be prestressed to ensure that in operation the ceramic is in compression. All loads resulting from internal pressure are taken by the prestressing system. There is insulation between the chamber and the tendons to maintain their temperature within their usable range.

The chamber is ringed circumferentially with a pair of 40-cm-deep aluminum composite girders (Fig. 2-2) that serve both to support the chamber and to provide a surface for rotation. The girders are mounted on 24 supporting wheels — six axles carrying two wheels on each ring. Four of the 12 axles are motor-driven.

Blanket material slides along the chamber wall under centrifugal action and issues from the chamber through an equatorial slot onto an exposed shelf on the outside of the chamber facing away from the chamber mid-plane (Fig. 2-3). A controllable scoop (Fig. 2-3) removes material from the shelf and provides the primary reactor flow rate and power level control.

Details of the design are presented below.

Materials. Examining the materials for the chamber, a SiC ceramic used in a modular prestressed form offers some very useful advantages. Its properties are summarized in Table 2-2. First, the configuration lends itself perfectly to prestressing techniques. At 1300 K, the flexural strength of chemical vapor deposited (CVD) β-SiC is 500 to 1000 MPa (70 to 140 ksi) for small samples (Ref. 2-3). In an application similar to the present and by applying proof-testing techniques as described

SHELF DETAIL

SLOT

MATERIAL FROM SLOT
RESTS ON SHELF AT
ANGLE OF REPOSE TO
CENTRIFUGAL FIELD

CHAMBER WALL

POSITION CONTROL
CYLINDERS

VARIABLE POSITION BLADE IS PRIMARY
REACTOR FLOW RATE CONTROL
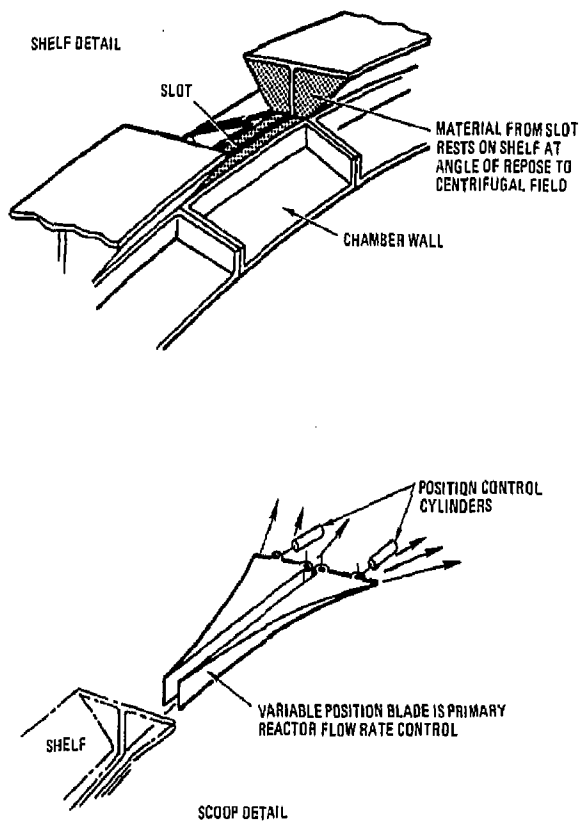
SHELF

SCOOP DETAIL

Fig. 2-3. SiC shelf and scoop details

in Ref. 2-3, α-SiC material has a design tensile stress allowable of 200 MPa (30 ksi) and a compressive stress allowable which is 4 to 5 times greater. Its Young's modulus is 360 GPa and its critical buckling stress is 8 GPa assuming a value for Poison's ratio of 0.3. The rupture stress is greater than 400 MPa. Consequently, the design has very high allowable prestress and applied working stress. Second, SiC has very high abrasion resistance. This is a very useful attribute, particularly in the present application in which a high mix power input is desired. Third, its activation is very low, even with presently achievable impurity levels, allowing hands-on maintenance, providing high inherent public safety and permitting shallow land burial of wastes at end-of-life (Ref. 2-6).

TABLE 2-2
MATERIAL PROPERTIES

SiC[a]. 1300 K

Density	3.21×10^3 kg/m^3
Thermal expansivity	4.9×10^{-6} K^{-1}
Thermal conductivity	50 W/m-K
Young's modulus	360 GPa
Flexural strength, CVD-β, small sample	500 to 1000 MPa
Tensile strength, α, proof-tested large sample	200 MPa

Avco SiC/Aluminum[b], continuous fiber
45 to 50% volume reinforcement, 700 K

Density	2.85×10^3 kg/m^3
0°fiber axial modulus	170 GPa
0°axial tensile strength	970 MPa

Nicalon SiC/Aluminum[c], 30% fiber fraction
volume, 6061 Al, 700 K

Tensile strength	400 MPa

[a]Ref. 2-3.
[b]Ref. 2-4.
[c]Ref. 2-5.

2-8

Steels or other materials are, of course, usable and chambers of 2-1/4 Cr-1 Mo were proposed in Refs. 2-1 and 2-2. However, by using a properly prestressed and insulated ceramic, the structure and prestressing tendons can be radiatively cooled, as shown in Section 2.3. The resultant temperatures and temperature gradients produce negligible thermal stresses and avoid the active cooling systems associated with a metal chamber.

The proposed prestressing tendon material is a Avco SiC unidirectional fiber/Al composite. At a 45% to 50% fiber volume fraction in aluminum, this material has an axial tensile strength of approximately 970 MPa (140 ksi) at 700 K (Ref. 2-4). A composite with 6063 Al alloy is preferred in the present application, since it has only low-activation alloying elements, and it is assumed that such a composite would have comparable strength.

The proposed insulation material is fibrous-type thermal insulation such as Fiber-frax (Ref. 2-7) or Min-K (Ref. 2-8). Foil-type insulators (Ref. 2-9) though superior to the fibrous-type with factors of 10 lower thermal conductivities are not recommended since these commonly employ thoria, zirconia, and other metals which would result in higher activation levels.

Stress Analysis. The sources contributing to the total stress in the Cascade reaction chamber were identified and calculated for a metallic chamber design in Refs. 2-1, 2-2, and 2-10. Following the methodology and equations presented in the references, the stresses were calculated for a SiC ceramic chamber with 2 cm wall thickness and a 1 m thick Li_2O blanket rotating at 4.2 rad/s (40 rpm).

Mechanical stress from centrifugal action was calculated using

$$\Gamma_c = \frac{m_B \omega^2 R^2}{A t \cos \theta} ,$$

where

Γ_c = hoop stress in the chamber wall = 20 MPa

m_B = blanket mass = 200,000 kg

ω = chamber rotational speed = 4.2 rad/s

R = the maximum chamber wall radius = 5 m

A = chamber surface area = 250 m^2

t = chamber tile thickness = 0.02 cm, and

θ = chamber wall half-angle = 30^c

Thermal stress was calculated using

$$\Gamma_{th} - \frac{\alpha E \Delta T_w}{2(1 - \nu)} \,,$$

where

Γ_{th} = thermal stress in the chamber wall = 5 MPa

α = SiC coefficient of thermal expansion = $4.9 \times 10^{-6} \ K^{-1}$

E = Young's modulus = 360 GPa

ΔT_w = temperature difference across the chamber wall = 4 K

ν = Poisson's ratio = 0.3 (assumed)

The stresses due to pressure from vaporized material and shock due to X-rays, debris, etc., were scaled from Ref. 2-10 to the present chamber wall thickness and material properties. The results are summarized in Table 2-3.

The maximum stress of 59 MPa (8.6 ksi) is acceptable in comparison to the 200 MPa tensile strength expected in the SiC tiles constituting the reaction chamber. In fact, the tiles would be preloaded in compression to the 54 MPa stress level expected from the centrifugal action and the microexplosion-induced shock wave. Thus the maximum tensile stress borne by the tiles is the 5 MPa thermal stress.

The shear stresses on the tiles were calculated by noting that the ring girder and shell form a four-shear system, each carrying one-fourth of the 200,000 kg system mass. The shear can be assumed to concentrate on a maximum of 3 m of shell in each of 2 paths. The maximum shear stresses on the 0.02 m tiles are thus 4 MPa, compared

TABLE 2-3

SUMMARY OF THE REACTION CHAMBER HOOP STRESS

Source of Stress	Level of Stress (MPa)
Centrifugal action[a]	20
Thermal stress[b]	5
Pressure from vaporized material[a,c,d]	18
Shock caused by X-rays, debris, and neutrons (600-MJ, 5-Hz chamber)[a,e]	34
Total stress	43 to 59

[a]Primary stresses.

[b]Secondary stress.

[c]Stress caused by pressure from ablated material assumes no heat transfer. The value included here is twice the static value, which accounts for dynamic loading.

[d]Peak stress caused by pressure from ablated material occurs at a later time than the peak stress caused by shock interaction; therefore, pressure and shock stresses are not additive. Totals shown include one or the other of these stresses.

[e]Shock-caused stresses are calculated at cylindrical limit. Our value for Cascade should be lower.

---

to the 400 MPa rupture stress and 8 GPa critical buckling stress. Therefore, the tiles are not expected to either rupture or buckle. Since considerable flexibility exists in the structural design of the tiles, the 2 cm wall thickness is chosen on the basis of ease of fabrication.

The tendon dimension is set by the maximum 54 MPa preload. Assuming single cables of Avco SiC/Al composite at 700 K prestressed to 80% of their tensile strength, longitudinally and circumferentially along all tile interfaces, the tendon diameter is 3.0 cm. As shown in Section 2.3, the allowable heat generation rate in the tendon is inversely proportional to the tendon diameter. The tradeoff on tile dimension and

number of cables per interface versus heat transfer requirements should be investigated in future design efforts.

Because of its large size, the stresses in the reaction chamber shell are comparatively small; however, the support requirement generates large forces virtually normal to the shell, which it is not well equipped to take. To distribute these local forces, a pair of 40 cm deep Nicalon SiC/Al composite girders rings the chamber at two positions, providing a track for the rotation equipment. These girders take the support reaction and distribute it into the prestressed shell in the form of shears which are easily carried in the shell at a stress of 4 MPa.

The stress analysis of the support rings shows that the rotating chamber can be supported by two rings of I-shaped cross-section, mounted on a set of wheels. The configuration and the nature of the loading result in a statically indeterminate structure which can be readily analyzed if the following assumptions are made.

1. Radius of ring $\gg$ radial thickness of ring.
2. Supporting pressure produced by the wheels is uniform.

The results are given by Roark (Ref. 2-12). Assuming the reaction loads are distributed over an angle of 60 deg, the maximum moment, M_{max}, and shear, V_{max} along the circumference of the ring are 3.3×10^5 N-m and 2.5×10^5 N, respectively.

The design of the ring girder is based on the requirements of the AISC (Ref. 2-12), using the following allowables.

$$F_b = \text{allowable bending stress} = 0.6 \ F_y = 150 \text{ MPa}$$

$$F_v = \text{allowable shear stress} = 0.4 \ F_y = 100 \text{ MPa}$$

$$F_y = \text{yield stress} = 250 \text{ MPa}$$

The yield stress of the Nicalon SiC/Al composite was assumed to be approximately 2/3 of its tensile strength at 700 K. A girder composed of 23 cm by 2.5 cm flanges and a 1.3 cm $\times$ 36 cm web satisfies the requirements on stress allowables and geometric constraints of the AISC. Calculated bending stress in the flanges is 140 MPa, and the shear stress in the web is 55 MPa.

Support Wheels. In line with railway practice, a wheel load of around 80,000 N is used which requires 24 supporting wheels. Accordingly, a preliminary estimate of the diameter is approximately 0.75 m. Six axles each carrying two wheels are required on each ring, the axles will tilt and also be adjustably sprung to give control of the force per wheel and compensate for possible ring girder out of round. Much railway practice is relevant here. The biggest difference is the cooling requirements on the bearings due to the thermal deposition from radiation. Cooling can be accomplished by water or gas circulating through the bearing housings and no elaborate mechanical sealing appears necessary.

Drive System. The presently favored configuration for the drive system has the entire power input both for the chamber and for the blanket circulating system via 4 of the 12 axles on which the wheels are mounted. The direct power to lift a blanket circulation of 2700 kg/s to a height of 17 m is 450 kW, but considerable internal friction is anticipated and thus 225 kW on each of 4 shafts is a reasonable installed requirement. The shaft speed is 320 rpm. Since the motors are external to the vacuum chamber, the drive shaft penetrations should incorporate radiation shielded oil flooded vacuum seals. The size of Nicalon SiC/Al composite drive shafts is less than 8 cm diameter.

2.2.3. Mechanics of Contents

Introduction. The determination of the acceptable angle for an embankment has been a matter of historic study and has a strong presentation in the present literature of soil mechanics. Appropriate assumptions can be made for the Cascade particles which will be acceptably accurate and which will form a useful basis for design. However, the dynamics of flowing particles is less well documented and Cascade represents a considerable control task. The basic motion of the blanket is brought about by over-steepening the slope of the chamber wall with respect to the stability angle. This will cause some form of cylindrical slip where a buried surface shears due to the moment of the material above it about the surface. In a shallow mass such

2-13

as our blanket, the chamber wall itself is very likely to form a large fraction of the surface of slip. Without special measures, therefore, "slug" flow is to be expected with the possible exception of a talus near the large diameter. The flow in a talus has not been investigated, but there is reason to believe that mixing will only take place at the break point.

The flow pattern has been envisaged as follows. Material is deposited at the small diameter and slides toward the larger, assuming a smooth chamber. Radial and circumferential motions are expected to be small. The acceleration due to Coriolis effects is only about 0.04 G maximum, so the path curvature is small. A given surface will change shape but not area as it moves out, becoming wider in the direction of rotation and losing axial speed and length to give flow continuity.

None of these motions will promote mixing. As the large diameter is approached, it is possible that the surface may break due to vestigial cylindrical slippages. Certainly surface material will eventually submerge to the exit orifices. Since the radial power deposition profile is radially quite steep, this exit mixing will not help to reduce the temperature spread between the surface and rear of the bed. A discussion of the methodology for inducing mixing into this pattern is given below.

A problem to be encountered in the design of the chamber is definition of the amount by which chamber angle must exceed the static equilibrium angle to give enough drive force to effect the required flow. This is currently being investigated (Refs. 2-13 and 2-14). While the static angle will not vary with centrifugal force field, as the latter increases, the work available from a given excess angle will change. It is thus possible that a small variation from the simple cone is required even in the simplest of chambers to keep a good drive force. Extra energy will already be required where mixing is happening, i.e., near the exits which indicates that a higher angle is needed there, the converse of the above effect.

The last aspect of the soil mechanics issues which requires discussion is the outflow control. A basis exists for "hourglass" calculations and recent work (Ref. 2-13)

indicates that no major difficulties are expected in implementing control of the mass flow.

The mechanics of material flow in the Cascade chamber is envisioned as follows. The bed of Li_2O granules flows "down" the sides of the chamber from the small ends of the cones at the axis of rotation toward the exit slot at the equator. The material leaving the slot piles up on the shelf that circles the equator (Fig. 2-3). This plugs the exit slot and stops the flow which is bottom controlled. As the chamber rotates, material on the shelf encounters a stationary scoop that removes the Li_2O granules from the shelf. This makes it possible for additional Li_2O to flow out of the chamber onto the shelf, ready for the next revolution past the scoop. The depth to which the scoop cuts into the pile of Li_2O on the shelf can be adjusted (Fig. 2-3) to control the overall flow rate.

Summarizing the above design issues, two major factors appear. First, the conventional simple chamber will not promote mixing. Second, there is no complete body of theory which covers all the design objectives of the chamber solid dynamics. A number of chamber concepts are outlined below, and a first preference defined.

Chamber Configurations Considered. Brief descriptions and significant characteristics of the Cascade chamber configurations considered are presented in Fig. 2-4. The preferred design is the compound vane configuration shown in Fig. 2-5. The compound vane allows control of the material at the repose angle on surfaces which are much steeper, as shown in Fig. 2-6. The walls of the cone-shaped chamber are set at 45 deg to the chamber axis. The vanes are set at 57 deg to an axial plane along the walls (Fig. 2-5). This allows the Li_2O to see an effective angle of 27 deg (the expected angle of repose) along the vanes, "down" the wall from the entrance to the exit at the chamber equator. The flow along the vanes is bottom controlled by the shelf and scoop arrangement at the exit slot at the equator. The possibility exists for a thin, fast moving, top controlled surface layer that would flow directly down the 45 deg sides, slipping over the top of the more slowly-moving material flowing along
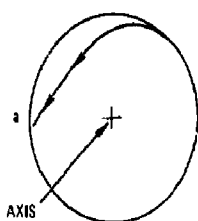
GRAVITY MIXED

• LOW CENTRIFUGAL FORCE ALLOWS FREE FALL OF BLANKET.

• DIFFICULT TO CONTROL AND EFFECTIVE AT LIMITED RADIUS RANGE.

AXIS
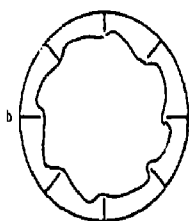
CORIOLIS STIR

• CORIOLIS ACCELERATIONS CAUSE DRIFT ACROSS VANES

• CORIOLIS FORCE ARE WEAK.
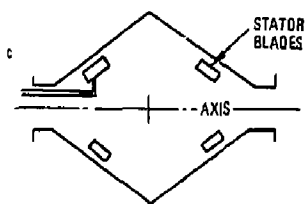
STATOR BLADES

STATOR BLADES

• BLADES STIR BLANKET MATERIAL.

• STATOR MOUNTS BURN

• COMPLEX

AXIS

Fig. 2-4. Chamber configurations considered.

OPTIONAL
BLADES

d
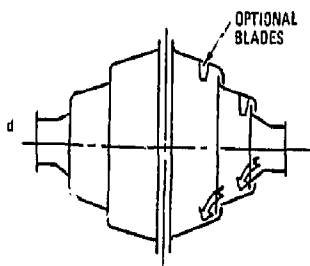
MULTIPLE FALL CHAMBER
● COUNTER ROTATING SECTIONS SPIN
MATERIAL INTO EACH OTHER.

● COMPLEX–MIXING IN WRONG PLANE.

e
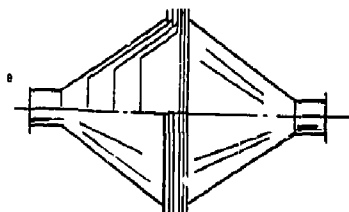
LAMINAR CHAMBER
● CHAMBER IS DIVIDED INTO LAMINAE
WITH INDIVIDUALLY CONTROLLED
SPEEDS.

● MAY BE PRACTICAL–CERAMIC ONLY.

f
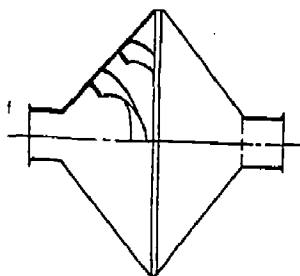
COMPOUND VANED CHAMBER
● 45° CONE SLOPE FOR COMPACTNESS.
57° TO AXIS VANES GIVE 27°
EFFECTIVE CHAMBER ANGLE.

● SELECTED DESIGN.

Fig. 2-4. (Cont'd) Chamber configuration considered.

90° INCLUDED
CONE ANGLE

INTERNAL VANES CROSS
AXIAL PLANES AT 57°

57°

PITCH OF VANES IS TIED TO CONE
ANGLE; NUMBER AND DEPTH OF VANES
TO BE EXPERIMENTALLY DETERMINED.

FILL CYLINDER

57°

₵ ROTATION
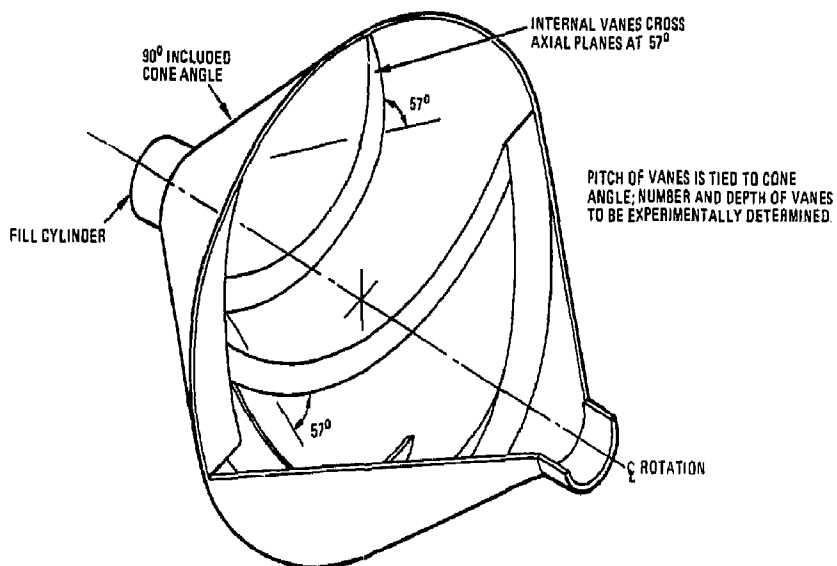
Fig. 2-5. Compound vane Cascade reaction chamber.
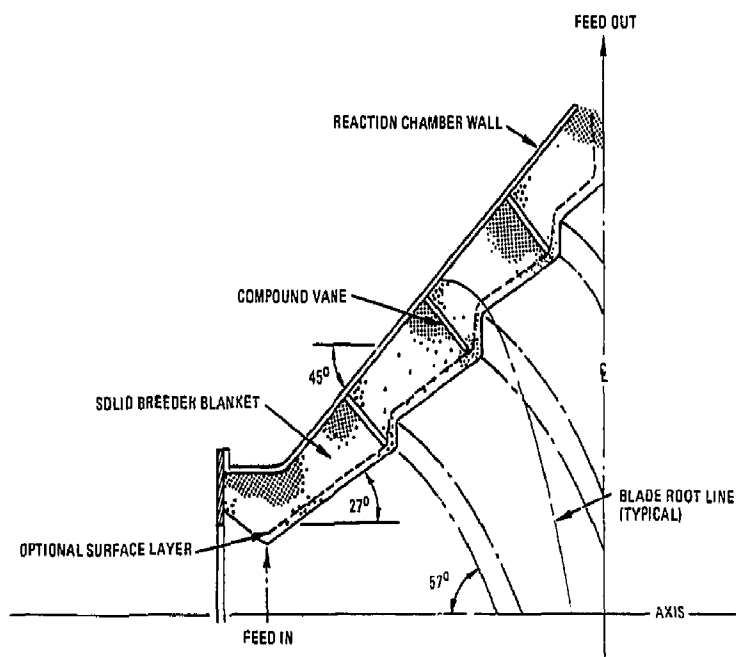
Fig. 2-6. Cross section of compound vane Cascade reaction chamber.

the vanes. The compound vane has the advantage that the chamber can be much more compact, and the microexplosion blast can be nearly normal to the blanket surface, thus not inhibiting blanket material flows. The compound chamber concept does not by itself induce any flow mixing. A disadvantage is that the vane's inner edge sees a higher neutron flux and the consequent radiation damage may necessitate its replacement.

The desire for flow mixing is due to the very steep radial gradient in power density in the Li_2O bed. This is discussed in Section 2.4 below and various potential techniques to achieve a more uniform Li_2O outlet temperature distribution are introduced. Flow mixing would be perhaps the most desirable method, but we have not identified a viable approach to achieve significant mixing of the bed flow by chamber design alone. Some form of layer flow control, as discussed in Section 2.4, will be needed if simple slug flow with a possible separate surface layer is not adequate.

Particle Removal from the Chamber. A narrow slit in the chamber around its large diameter allows the blanket particles to escape from the bottom of the blanket layer. Around the chamber waistline is a centrally disposed cylinder which acts as a shelf (see Fig. 2-3). The particles escape from the chamber until the shelf forms a heap to the level of the slit at which point the flow will be bottom controlled and stop. Further removal of material from the chamber is then entirely dependent on material being removed from the shelf.

On the rising side of the chamber, a scoop (see Fig. 2-3) is disposed either side of the heaped shelf. As the shelf travels past at about 25 m/s, the scoop reaches in either side and clears off the shelf, allowing it to recharge. A shelf dimension of 50 cm (each side) is adequate to clear the Li_2O throughput of 2.7 m^3/s in one revolution at 40 rpm.

2.3. HEAT TRANSFER

The majority of the fusion energy produced in Cascade is deposited in the bed of Li_2O granules and thus transported out of the reaction chamber, to the power

conversion system. Some energy, however, is deposited in the chamber itself and some heat is transmitted from the Li$_2$O bed to the chamber. The thermal and heat transfer analysis of the chamber is presented in this section.

2.3.1. Introduction

A one-dimensional heat transfer model was prepared in order to determine equilibrium temperatures in the ICF Cascade chamber design. Figure 2-7 is a schematic diagram of this model.

Conductive heat transfer was modeled using Fourier's Law:

$$q_{ij} = k_{ij} A_{ij} \frac{dT}{dX}.\qquad (1)$$

where

$$q_{ij} = \text{heat flow from } i \text{ to } j$$

$$k_{ij} = \text{material thermal conductivity}$$

$$A_{ij} = \text{mean surface area}$$

$$\frac{dT}{dX} = \text{temperature gradient}$$

Radiative heat transfer was modeled using the equation

$$q_{ij} = \frac{\sigma A_i \left(T_i^4 - T_j^4 \right)}{\frac{1}{F_{ij}} + \left(\frac{1}{\epsilon_i} - 1 \right) + \frac{A_i}{A_j} \left(\frac{1}{\epsilon_j} - 1 \right)}.\qquad (2)$$

where

$$F_{ij} = \text{view factor (i to j)}$$

$$\epsilon_i = \text{emissivity}$$

$$A_i = \text{surface area}$$

2-21

VACUUM
CHAMBER

TENDONS

6a = FREE
6b = AT POST

TENDON SUPPORT
POST

THERMAL INSULATION

SiC CHAMBER

Li_2O GRANULE ZONE
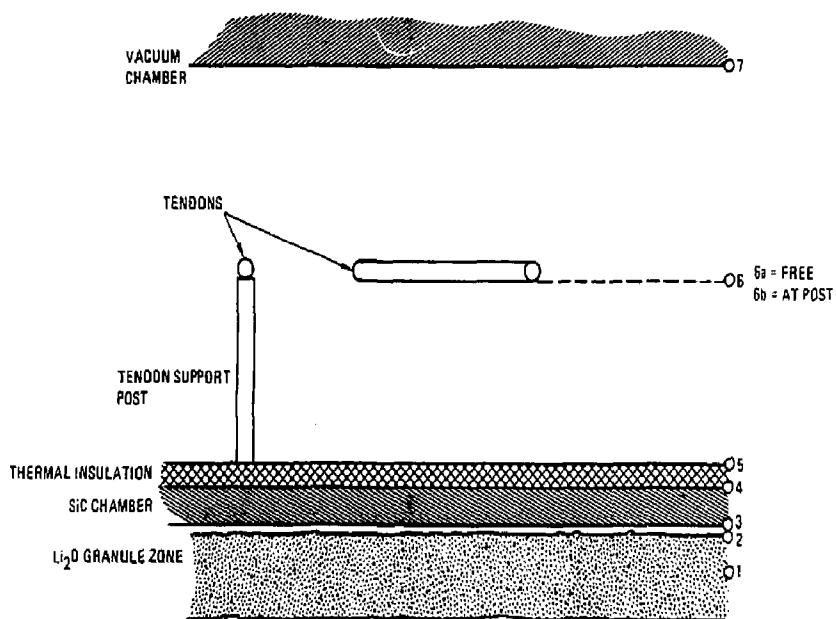
Fig. 2-7. Heat transfer model schematic.

T_i = surface temperature

σ = Stephan – Boltzman constant.

Convective heat transfer was assumed to be negligible due to near-vacuum conditions.

A steady-state analysis was used to determine equilibrium temperatures for each surface. The equilibrium temperatures are determined by simultaneous solution of the heat flow equations. The assumptions made in the development of the results are summarized in Table 2-4.

2.3.2. Model Development

The heat transfer model used in this analysis is developed in this section. The subscripts denote the locations as given in the schematic diagram, Fig. 2-7. The model is developed from the last granule zone out to the vacuum chamber.

Heat Flow in the Last Granule Zone. Since blanket flow mixing is not expected, one way to achieve a uniform outlet temperature distribution in the blanket in the presence of the radial heat granulation profile is to have a zoned blanket, as described in Section 2.4. For conservatism, a five-zone blanket of 20 cm layers was assumed for the heat transfer analysis. The temperature at the midpoint of the last granule zone at the exit of the chamber is the point of highest temperature in the bed and thus represents the worst case for heat transfer analysis. This corresponds to point 1 in the schematic drawing, Fig. 2-7. From the equation for the heat generation in the granule layer, we can calculate a temperature at the outer layer of the granule bed, point 2. We assume the granule bed is moving in laminar or plug flow, and that lateral heat flow within the blanket (perpendicular to the flow direction of the bed) is negligible. Since the granule bed is the working medium for the ultimate heat transfer of the system, we would expect that an optimized design would have the bed carrying away nearly all of the heat generated. Therefore, our assumption should be

2-23

TABLE 2-4
SUMMARY OF BASELINE CONDITIONS, ASSUMPTIONS, and ESTIMATES

Assumptions

1. Convective heat transfer is negligible.
2. Lateral heat flow in the granule blanket is negligible.
3. Granule blanket-to-wall interface heat transfer is that of Schlunder (Ref. 2-15).
4. SiC chamber and insulation heat generation is small compared to vacuum chamber heat flow.
5. Tendon heat generation is small compared to the reaction chamber-to-vacuum chamber heat flow.

Reference Parameters

T_{inlet} granules = 770 K

T_1 (midpoint of last granule zone at outlet) = 1170 K

$\Delta X_{SiCchamber}$ = 0.02 m

A_3 (reaction chamber surface area) = A_4 = 260 m^2

ΔX_{45} (insulation) = 0.15 m

A_5 (insulation outside surface area) = 270 m^2

d_{tendon} = 0.03 m

L (tendon length) = 1100 m

A_6 (tendon surface area) = 100 m^2

$\dot{q}'''_{tendon}$ = 6.5 × 10^5 W/m^3

T_7 (vacuum chamber) = 300 K

A_7 (vacuum chamber surface area) = 3500 m^2 (from Fig. 5-13)

σ (Stephan-Boltzman Constant) = 5.67 × 10^{-8} W/m^2-K^4

$U_{23} \simeq$ 2 W/m^2-K

k_{34} (SiC) = 50 W/m-K

k_{45} (Fiberfrax) = 0.1 W/m-K

ϵ_5 (insulation) = 0.4

ϵ_6 (tendons) = 0.2 (oxidized aluminum plate)

ϵ_7 (vacuum chamber) = 0.6 (steel)

$\overline{F}_{57}$ = 0.8

$\overline{F}_{65}$ = 0.6

$\overline{F}_{67}$ = 0.85

---

reasonable, and we can proceed with the determination of T_2, the outer granule bed temperature.

The steady-state heat flow equation for the bed is

$$q = \dot{m} c_p \Delta T.$$ (3)

where

q = internally generated heat

$\dot{m}$ = mass flowrate of the bed

c_p = heat capacity of the bed

ΔT = outlet temperature – inlet temperature.

Since q varies with the radial distance from the center of the reaction chamber and radial heat transfer within the blanket is neglected, we know that $q = q(r)$ and $T = T(r)$. With this we have

$$q(r) = \dot{m} c_p \left[T(r) - T_{inlet} \right].$$ (4)

The inlet temperature of the granules is assumed to be 770 K. Since we further assume that the outlet temperature at $r = 4.875$ (point 1) is 1170 K, we get

$$q(4.875) = \dot{m} c_p (1170 - 770) = \dot{m} c_p (400).$$ (5)

If we divide $q(r)$ by $q(4.875)$, we get

$$\frac{q(r)}{q(4.875)} = \frac{\dot{m} c_p \left[T(r) - 770 \right]}{\dot{m} c_p (400)}.$$ (6)

Solving for $T(r)$, we have

$$T(r) = 400 \frac{q(r)}{q(4.875)} + 770 \text{ K}.$$ (7)

The radial dependence of the volumetric heat generation rate was estimated based on a numerical fit of the neutronics data of Ref. 2-16. This was determined to be

$$q(r) \; \alpha \; \frac{e^{-3.5r}}{r^2} \; .$$

Substituting this expression for the heat generation rate into Eq. (7), we have

$$T(r) = 400 \frac{e^{-3.5r}}{r^2} \cdot \frac{4.875^2}{e^{(-3.5)(4.875)}} + 770 \text{ K} , \qquad (8)$$

which reduces to

$$T(r) = 2.44 \times 10^{11} \frac{e^{-3.5r}}{r^2} + 770 \text{ K} . \qquad (9)$$

At the outside of the last granule layer, point 2, $r = 5$ m and $T_2 = 1020$ K.

Heat Flow Between the Granule Blanket and Reaction Chamber Wall.
The heat flow from the blanket to the reaction chamber wall can be modelled as a psuedo-convective heat transport situation. Thus, we have

$$q_{23} = U_{23} A_{23} (\Delta T) = U_{23} A_{23} (T_2 - T_3) \qquad (10)$$

There are correlations for determining the heat transfer coefficient, U, in particle systems such as this. A correlation from Schlunder (Ref. 2-15) is presented below in the development of the baseline calculations.

Heat Flow in the Reaction Chamber Wall. This is simple conductive heat transfer so that

$$q_{34} = k_{34}A_{34}\frac{\Delta T_{34}}{\Delta X_{34}} = \frac{k_{34}A_{34}}{\Delta X_{34}}(T_3 - T_4) . \qquad (11)$$

This assumes that the heat generation within the SiC is small compared to the heat flow from the blanket.

Heat Flow in the Insulation Layer. Again, we have conductive heat transfer so that

$$q_{45} = \frac{k_{45}A_{45}}{\Delta X_{45}}(T_4 - T_5) . \qquad (12)$$

Heat Flow Between the Insulation and the Vacuum Chamber. This is a radiative heat transfer situation so that we have

$$q_{57} = \frac{\sigma A_5 \left(T_5^4 - T_7^4\right)}{\frac{1}{F_{57}} + \left(\frac{1}{\epsilon_5} - 1\right) + \frac{A_5}{A_7}\left(\frac{1}{\epsilon_7} - 1\right)} . \qquad (13)$$

An assumption implicit in this formulation is that the contribution of the heat transfer from the tendons can be neglected in establishing the heat flow between the insulation and the vacuum chamber. This assumption has the effect of decoupling the reaction and vacuum chamber heat balance equations from the tendon heat balance equation. This assumption is discussed in Section 2.3.5.

Heat Balance on Prestress Tendons. Steady-state analysis dictates that (input – output + production = 0). The input and output terms for the tendon system are radiation terms from the insulation and to the vacuum chamber, respectively. (Heat transfer via conduction through the post to position 6b in Fig. 2-7 is small compared to the radiative heat transfer.) Note that the actual direction of the heat flow is unimportant in the mathematics of the formulation. We have

$$input = \frac{\sigma A_6 \left(T_5^4 - T_6^4\right)}{\frac{1}{F_{65}} + \left(\frac{1}{\epsilon_6} - 1\right) + \frac{A_6}{A_5}\left(\frac{1}{\epsilon_5} - 1\right)} \, . \tag{14}$$

and

$$output = \frac{\sigma A_6 \left(T_6^4 - T_7^4\right)}{\frac{1}{F_{67}} + \left(\frac{1}{\epsilon_6} - 1\right) + \frac{A_6}{A_7}\left(\frac{1}{\epsilon_7} - 1\right)} \, . \tag{15}$$

The generation or production term will be left as a dependent variable in our analysis. Therefore, we can solve for

$$\dot{q}''' = \frac{\sigma A_6}{V}\left[\frac{\left(T_6^4 - T_7^4\right)}{\frac{1}{F_{67}} + \left(\frac{1}{\epsilon_6} - 1\right) + \frac{A_6}{A_7}\left(\frac{1}{\epsilon_7} - 1\right)} - \frac{\left(T_5^4 - T_6^4\right)}{\frac{1}{F_{65}} + \left(\frac{1}{\epsilon_6} - 1\right) + \frac{A_6}{A_5}\left(\frac{1}{\epsilon_5} - 1\right)}\right] \, .$$

Because the area and volume are both related to the length and diameter of the tendons, this equation can be further reduced to

$$\dot{q}''' = \frac{4\sigma}{d_l}\left[\frac{\left(T_6^4 - T_7^4\right)}{\frac{1}{F_{67}} + \left(\frac{1}{\epsilon_6} - 1\right) + \frac{A_6}{A_7}\left(\frac{1}{\epsilon_7} - 1\right)} - \frac{\left(T_5^4 - T_6^4\right)}{\frac{1}{F_{65}} + \left(\frac{1}{\epsilon_6} - 1\right) + \frac{A_6}{A_5}\left(\frac{1}{\epsilon_5} - 1\right)}\right] \, . \tag{16}$$

2.3.3. Solution of Temperature Equations – Baseline Case

The solution of the temperature equations involves simultaneous solution of the heat flow equations, Eqs. (10), (11), (12), and (13). The heat flows through the various layers of the chamber must be equal at steady state. Thus, the heat flow equations are all equivalent. First, we equate Eqs. (10) and (13) to get

$$T_3 = T_2 - \frac{\sigma A_5}{U_{23}A_{23}}\left[\frac{\left(T_5^4 - T_7^4\right)}{\frac{1}{F_{57}} + \left(\frac{1}{\epsilon_5} - 1\right) + \frac{A_5}{A_7}\left(\frac{1}{\epsilon_7} - 1\right)}\right] \, . \tag{17}$$

This can be substituted into Eq. (11), which can then be equated with Eq. (13) to yield

$$T_4 = T_2 - (\sigma A_5) \left(\frac{1}{U_{23}A_{23}} + \frac{\Delta X_{34}}{k_{34}A_{34}} \right) \left[\frac{\left(T_5^4 - T_7^4\right)}{\frac{1}{F_{57}} + \left(\frac{1}{\epsilon_5} - 1\right) + \frac{A_5}{A_7}\left(\frac{1}{\epsilon_7} - 1\right)} \right] . \quad (18)$$

Finally, this equation can be substituted into Eq. (12), which can then be equated to Eq. (13) to give

$$T_5 = T_2 - (\sigma A_5) \left(\frac{1}{U_{23}A_{23}} + \frac{\Delta X_{34}}{k_{34}A_{34}} + \frac{\Delta X_{45}}{k_{45}A_{45}} \right)$$
$$\times \left[\frac{\left(T_5^4 - T_7^4\right)}{\frac{1}{F_{57}} + \left(\frac{1}{\epsilon_5} - 1\right) + \frac{A_5}{A_7}\left(\frac{1}{\epsilon_7} - 1\right)} \right] . \quad (19)$$

This is an implicit solution in T_5 which will require iteration to solve.

The Eqs. (17) to (19) constitute the solution of the temperature equations in their general form. The baseline case is a calculation of temperature and tendon heat balance results based on approximations of the parameters which describe the system as listed in Table 2-4.

Parameter Summary. We are interested in calculating numerical values from Eqs. (16) to (19). A number of assumptions about the system are required in order to determine some of the parameters which are needed in the solution equations. Some of the parameters are set for the system based on engineering judgment. Others can be calculated based on system geometry. This section is a detailed compilation of the parameters listed in Table 2-4.

We have already computed the value for T_2:

$$T_2 \cong 1020 \text{ K}.$$

Next, we obtain an estimate for the heat transfer coefficient, U, between the granule bed and the reaction chamber wall. In Ref. 2-15, Schlunder presents a graphical correlation for the average wall-to-packed bed heat transfer coefficient. Since our conditions very nearly match his (1 mm spherical particles, water vapor present), we can use Fig. 2 in Ref. 2-15. Our conditions are 1.3 Pa tritium pressure (see Chapter 4) at 1020 K, which correspond to 0.25 MPa at 200 K using the perfect gas law, resulting in

$$U_{23} \cong 2 \text{ W/m}^2 \text{-K}$$

The available heat transfer area at this interface is

$$A_{23} = 260 \text{ m}^2$$

The mean heat transfer area through the reaction chamber wall is estimated to be approximately the same, or

$$A_{34} = 260 \text{ m}^2$$

Mechanical design has set the reaction chamber wall at a thickness of

$$\Delta X_{34} = 0.02 \text{ m}$$

The thermal conductivity of SiC is

$$k_{34} = 50 \text{ W/m - K}$$

The mean heat transfer area through the insulation layer is estimated to be

$$A_{45} = 265 \text{ m}^2 .$$

The maximum insulation thickness is set by the maximum post height allowed by mechanical design. Thus,

$$\Delta X_{45} = 0.15 \text{ m}$$

For the baseline calculation, it will be assumed that the insulation is Fiberfrax. Its thermal conductivity is (Ref. 2-7)

$$k_{45} = 0.1 \text{ W/m} - \text{K}$$

It is noted that Min-K (Ref. 2-8), also a fibrous type insulation, has an effective thermal conductivity ~1/3 that of Fiberfrax in vacuum. Foil-type insulators have effective thermal conductivity 1/30 that of Fiberfrax (Ref. 2-9). The emissivity of the insulation is estimated to be

$$\epsilon_5 = 0.4 .$$

We will assume that the vacuum chamber wall has an area given by the design in Section 5.4, Fig. 5-14

$$A_7 = 3500 \text{ m}^2 .$$

The emissivity of the vacuum chamber wall will be assumed to be that of steel so that

$$\epsilon_7 = 0.6 .$$

2-31

The vacuum chamber wall was assumed to be at room temperature:

$$T_7 = 300 \text{ K} .$$

The tendon diameter is set by mechanical considerations at

$$d_t = 0.03 \text{ m} .$$

The emissivity of the tendons will be assumed to be the same as that for oxidized aluminum plate. Thus,

$$\epsilon_6 = 0.2 .$$

The total length of the tendons in the design is

$$L = 1000 \text{ m}^2 .$$

$$A_6 = 100 \text{ m}^2$$

The following values were estimated for view factors:

$$\overline{F}_{57} = 0.8$$
$$\overline{F}_{65} = 0.6$$
$$\overline{F}_{67} = 0.85$$

Finally, Stephan-Boltzman's constant is given as

$$\sigma = 5.67 \times 10^{-8} \text{ W/m}^2 - \text{K}^4$$

We have now completed the compilation of the various parameters and can proceed with a numerical solution to Eqs. (16) through (19).

Results. Solution of Eqs. (17) through (19) using the parameters determined above yields the following equations:

$$T_3 = 1020 - \left(1.051 \times 10^{-8}\right)\left(T_5^4 - 300^4\right) . \tag{20}$$

$$T_4 = 1020 - \left(1.052 \times 10^{-8}\right)\left(T_5^4 - 300^4\right) . \tag{21}$$

$$T_5 = 1020 - \left(4.145 \times 10^{-8}\right)\left(T_5^4 - 300^4\right) . \tag{22}$$

By iteration, Eq. (22) yields a value of approximately

$$T_5 = 391 \text{ K} .$$

It follows that

$$T_3 = 860 \text{ K} ,$$

and

$$T_4 = 859 \text{ K} .$$

Equation (16) is solved with the above parameters to give

$$\dot{q}''' = \left(2.67 \times 10^{-6}\right) T_6^4 - 4.02 \times 10^4 \text{ W/m}^3 . \tag{23}$$

For the baseline tendon heat generation rate,

$$T_6 = 713 \text{ K} .$$

Avco SiC/Al composite has strength-at-temperature capability up to ~800 K. The 713 K temperature calculated here thus indicates that the tendons can be maintained within the material's usable temperature range without active cooling or additional nuclear shielding.

The temperature distribution throughout the system is summarized in Table 2-5.

TABLE 2-5
SUMMARY OF HEAT TRANSFER RESULTS

T_1 (midpoint of last granule zone)	= 1170 K
T_2 (outside granule surface)	= 1020 K
T_3 (inside reaction chamber surface)	= 860 K
T_4 (outside reaction chamber surface)	= 859 K
T_5 (outside insulation surface)	= 391 K
T_6 (tendon)	= 713 K
T_7 (vacuum chamber)	= 300 K

2.3.4. Discussion of Parametric Variations

First, we can examine the tendon heat balance equation in its general form, Eq. (16). We can immediately see that the allowable heat generation in the tendon is inversely proportional to the diameter of the tendon. Thus, we can best influence the allowable heat generation rate by varying the tendon diameter. We have set

$$\epsilon_6 = 0.2 ,$$

based on the emissivity of oxidized aluminum plate. With this value, the term

$$\left(\frac{1}{\epsilon_6} - 1\right) = 4.0,$$

dominates the denominator of both of the radiant heat transfer derived terms in Eq. (16). For this reason, we can see that variation in the other terms in the denominators, such as view factors and surface areas, will create only minor changes in the allowable heat generation rate. Because the value chosen for the vacuum chamber wall temperature, T_7, is so low (300 K), this term will have relatively little influence on the calculation of the allowable heat generation rate. However, if higher vacuum chamber wall temperatures are expected, this term might become more significant. The insulation surface temperature, T_5, is comparable to the vacuum chamber temperature, T_7, and therefore is expected to have a similar influence on the results obtained from Eq. (16). It is important to note that changes in these temperatures produce a magnified change in the results of the equation because they are fourth order terms.

Now, we can examine the reaction chamber temperature equations, Eqs. (17) through (19). These equations all have a common term, the term derived for radiant heat transfer

$$\frac{\left(T_5^4 - T_7^4\right)}{\frac{1}{F_{57}} + \left(\frac{1}{\epsilon_5} - 1\right) + \frac{A_5}{A_7}\left(\frac{1}{\epsilon_7} - 1\right)}.$$

With the parameter values chosen, we can see that the terms in the denominator have the following values

$$\frac{1}{F_{57}} = 1.25,$$

$$\left(\frac{1}{\epsilon_5} - 1\right) = 1.5,$$

$$\frac{A_5}{A_7}\left(\frac{1}{\epsilon_7} - 1\right) = 0.051,$$

We can deduce from this that the vacuum chamber wall provides a very effective sink (note the third term), primarily due to its large area. Changes in the parameters

in this term will have little influence on the final temperature results, unless those changes are very significant. Changes in the other two terms listed will have a greater influence on the final temperature resuls. The vacuum chamber wall temperature, T_7, has been chosen as such a small value that it has relatively little effect on the final temperature, compared to the insulation surface temperature, T_5. However, as in the tendon heat balance, changes in this value have a magnified effect on the final result due to the fourth order nature of this term.

In each temperature equation, the radiant heat transfer derived term is multiplied by a resistance term and by

$$\sigma A_5 .$$

The insulation surface area, A_5, can be determined with good accuracy, knowing the geometry of the design. Therefore, this term is not considered to be a controllable parameter in this analysis. The resistance terms are as follows

$$\frac{1}{U_{23}A_{23}} = 1.9 \times 10^{-3} ,$$

$$\frac{\Delta X_{34}}{k_{34}A_{34}} = 1.5 \times 10^{-6} ,$$

$$\frac{\Delta X_{45}}{k_{45}A_{45}} = 5.7 \times 10^{-3} .$$

We can see that the greatest resistance is offered by the granule blanket-to-wall interface and the insulation layer (the first and third terms). The SiC reaction chamber offers negligible resistance and therefore has little influence on the final results. Thus, the controllable parameters of importance are the heat transfer characteristics at the blanket-to-wall interface and the resistance of the insulation layer. The values chosen for these terms will be of greatest importance in selecting the final design.

2.3.5. Conclusions

The baseline temperature distribution was calculated and the results show that cooling of the reaction chamber and tendon system can be accomplished by radiative heat transfer to the vacuum chanber. A significant range exists in the selection of system parameters including the diameter and emissivity of the tendon, the conductivity of the insulation, and the heat transfer coefficient at the blanket-to-wall interface. Proper selection of tendon design is very important in order to handle the expected heat generation within the tendons. The most critical parameter is the tendon diameter. The overall heat balance for the reaction chamber layers is controlled by the selection of the insulation layer design. Its design will have an appreciable effect on the heat balance on the tendons. Therefore, it is important to identify limits on the insulation layer design so that they can be considered in the design of the prestress tendons.

It is recommended that the following areas be studied in more detail:

1. Coordination of mechanical design and thermal design to optimize tendon diameter.
2. Verification of the emissivity of tendon material.
3. Identification of limitations on insulation layer design.
4. Identification of alternative insulation layer designs.

In addition to these specific areas, it is recommended that future work include integration of materials selection, mechanical, and thermal design.

The present heat transfer model assumes that the heat generation in the tendons does not substantially add to or affect the main heat flow from the insulation to the vacuum chamber, in effect decoupling the equations. In fact, the temperature difference between the insulation surface and the vacuum chamber is sufficiently low that heat flow from the tendons is significant and could affect the overall temperature distribution. This is not expected to alter the conclusions of this analysis due to the considerable flexibility in the design and selection of system parameters. It is recommended that future efforts fully couple the system equations.

The current heat transfer model should also be expanded to include spatially varying heat generation terms in all layers and be expanded to give a temperature profile within the tendons.

2.4. THERMODYNAMICS OF SOLID GRANULE CIRCULATION

The majority of the fusion power produced in Cascade is deposited in the bed of Li_2O granules and is transported out of the reaction chamber with the flowing Li_2O. The thermodynamics of this solid energy transport system are developed in this section.

2.4.1. Introduction

The overall thermodynamic efficiency of the Cascade reactor system as well as the practical design of the lithium oxide granule flow system are very much dependent upon the flow distribution and degree of granule mixing within the blanket. Several flow distributions were considered to determine the optimum blanket flow configuration. Although the actual particle behavior in the reaction chamber is difficult to predict, as discussed in Section 2.2, two extremes in flow and thermal behavior can be explored. The first case assumes that there is perfect radial mixing of the granules so that the average heat deposition rate is the same for all the granules. In this case, the granule's axial flow profile (from the front to the back of the blanket) is unimportant and all particles will exit with the same temperature. This can be called *mixed flow*. The second case assumes that there is no radial mixing or conduction between adjacent "layers" of granules. Since the heat deposition profile is not uniform in the radial direction, the granules will not have a uniform exit temperature unless their axial flow profile matches the heat deposition profile. This second type of behavior can be called *layered flow*.

The degree of flow *mixing* or *layering* is hard to predict quantitatively by particle dynamic theory alone. An empirical approach incorporating small scale experimental flow models would help in understanding this problem. Section 2.2 presents reaction

chamber design concepts that may be utilized to mechanically influence the degree of mixing. The question then arises as to which is the more desirable flow distribution. From thermodynamic efficiency considerations, a thoroughly mixed blanket is preferred, since it would provide a higher mixed mean outlet temperature than a layered flow blanket with finite zone widths. However, a thoroughly mixed blanket may experience other problems with the granules, such as exposint *all* granules to the surface heat flux, possibly increasing the rate at which granules must be replaced. This might be alleviated with a special *surface layer*, as discussed in Chapter 3. The mechanical design details for achieving either completely mixed or layered flow have not been fully developed, and so relative mechanical design complexities cannot be quantitatively compared with the associated gains in efficiency at the time. Therefore both types of flow were further analyzed. Combinations of the two are possible, and the solid flow options are graphically summarized in Fig. 2-8.

2.4.2. Mixed Flow

In this case, the total Li_2O mass flow rate $\dot{m}$ is determined by the total thermal power, P_{th}, the heat capacity of the granules. c_p, and the desired inlet/outlet temperature difference, ΔT, that is:

$$\dot{m} = \frac{P_{th}}{c_p \Delta T} .$$

For a blanket with a thermal power of 3000 MW, an average heat capacity of 2800 J/kg-K, and a temperature rise of 400 K, (from 770 K inlet to 1170 K outlet), the required flow rate is 2700 kg/s. A separate *surface layer* may be required to minimize the granule replacement rate. Assuming that 5 cm is a minimum practical thickness based on mechanical considerations, such a surface layer would contain approximately 42% of the flow or 1100 kg/s. Since good radial mixing is assumed, the axial flow profile is otherwise unimportant and the radial temperature distribution is flat. Assuming a 5 m outer radius reaction chamber, a blanket thickness of 1 m, and a density of

a. TOTAL MIXING

b. SURFACE LAYER/
   INTERNAL MIXING

c. LAMINAR LAYERS

d. SURFACE LAYER/
   SLUG FLOW

e. SURFACE LAYER/SLUG
   FLOW W/RECYCLE

FROM HX   RECYCLE

TO HX

RECYCLE

FAST SURFACE LAYER

BLANKET

CHAMBER
CENTERLINE

REACTION CHAMBER WALL
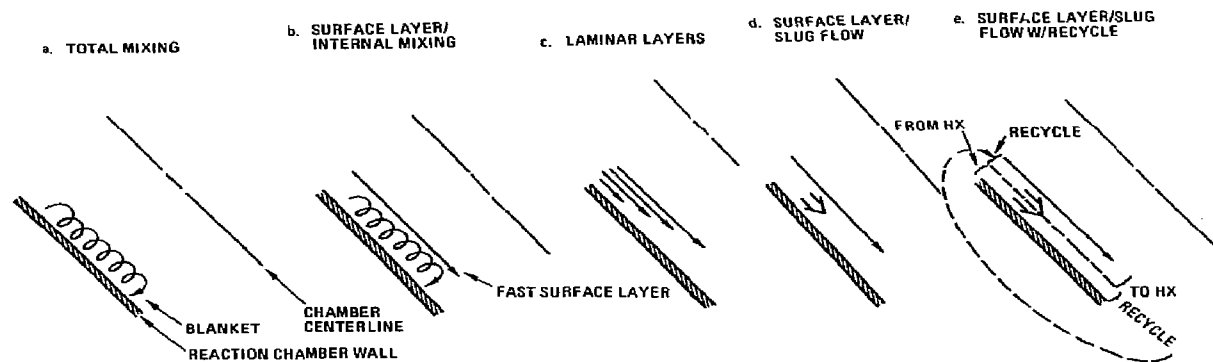
Fig. 2-6. Solid flow options.

1000 kg/m³ (including 50% packing factor), the average exit velocity in the direction parallel to the chamber walls is ~0.1 m/s and the average residence time is approximately 80 s.

2.4.3. Layered Flow

In this case, the heat deposition profile and the axial velocity profile are matched such that the exit temperature is radially uniform. This is accomplished by satisfying

$$P_{th} = \dot{m}c_p\Delta T = \int_{V_B} \dot{q}'''(r)dV \quad,$$

Noting that the differential volume of a hemisphere is $2\pi r^2 dr$, which equals rdA,

$$\rho v A c_p \Delta T = \dot{q}'''rdA$$

$$v = \dot{q}'''r/\rho c_p \Delta T$$

where $\dot{q}'''$ is the volumetric heating rate, ρ is the Li_2O effective density, v is the flow velocity, A is the cross-sectional area perpendicular to flow, V_B is the volume of the blanket, and r is the radial distance from the center of the chamber in meters. The volumetric heat generation rate can be expressed as

$$\dot{q}'''_r = \frac{7.2 \times 10^8 e^{-3.5r}}{r^2} \;,\; MW/m^3$$

by fitting the data generated in the neutronics calculations (Ref. 2-16). The quantity $\rho c_p \Delta T$ equals 1.1×10^9 J/m³, and thus the velocity profile is given by

$$v(r) = 6.4 \times 10^4 \; e^{-3.5r}/r, \;\; m/s.$$

We can then plot the velocity profile for all the granule layers except the first one. In the first layer we must include the surface heating effect. In order to include the surface

heating effect, a characteristic thermal penetration depth must be assumed. Figures 2-9 and 2-10 show the nuclear heating profile and the velocity profile, again assuming a 5 cm thick first layer. This would be the optimum velocity distribution for layered flow with respect to thermodynamic efficiency and minimum particle throughput.

Neither perfectly mixed nor perfectly layered flow is likely to occur in the reaction chamber. Furthermore, if indeed the velocity profile can be controlled, it would probably be in discrete zones rather than as the optimum continuous distribution. This issue was studied further to determine the number of zones required to achieve a given efficiency assuming no mixing. The velocity of each zone is assumed to be controllable; however, within a zone, the velocity is assumed constant. Thermodynamic inefficiency results from the fact that while the front granules of each zone can be heated to the maximum temperature, the granules further back in the zone are underheated. A blanket with fewer zones will also require more total granule throughput, since a greater fraction of the blanket is overcooled. The average exit temperature for each zone is somewhat less than the maximum, depending upon the radial thickness of the zone.

The temperature peaking factor within an individual zone can be calculated as follows. Since

$$v = \dot{q}'''r/\rho c_p \Delta T \text{ (from Sec. 2.4.2)}$$

then for constant v, ρ, and c_P, the quantity $\dot{q}'''r/\Delta T$ is constant. Therefore

$$\frac{\Delta T_{max}}{\Delta T_{avg}} = \frac{(\dot{q}'''r)_{max}}{(\dot{q}'''r)_{avg}}$$

where the subscripts *max* and *avg* refer to the maximum and average values within the zones, respectively, and $\dot{q}'''$ is as defined above. Thus, for a finite number of constant velocity zones, careful consideration must be given to their radial thickness

2-42
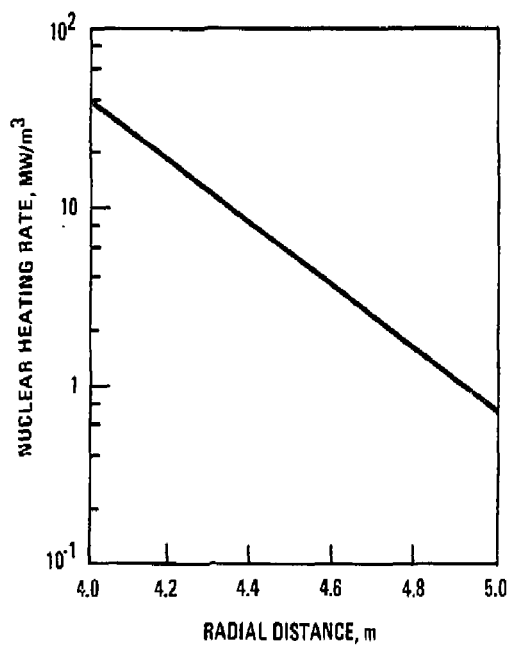
Fig. 2-9. Nuclear heating profile in Li_2O blanket.
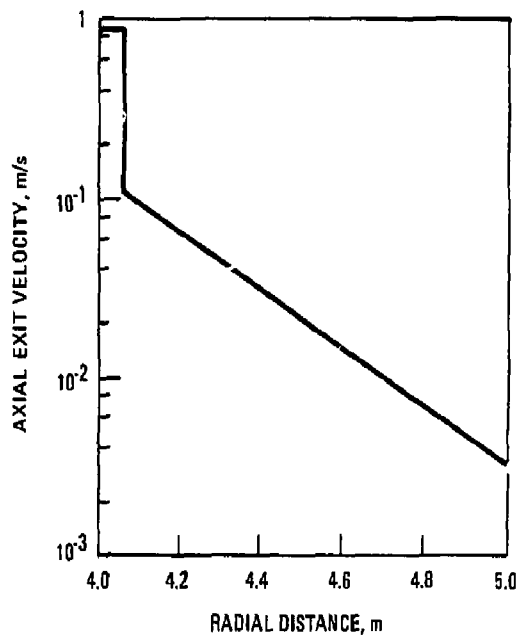
Fig. 2-10. Optimum velocity profile for perfectly "layered" flow.

and location of each zone. We can parametize this effect by using the $\dot{q}'''$ data as a function of r generated from the neutronics calculations to satisfy the above equation for several values of $\Delta T_{max}/\Delta T_{avg}$. The thermodynamic efficiency of the system is directly related to the value of ΔT_{max} and the assumed inlet temperature. ΔT_{avg} is limited by the maximum allowable Li_2O temperature. The number of zones is directly related to the allowable magnitude of $(\dot{q}'''r)_{max}/(\dot{q}'''r)_{avg}$ for each zone since the total change in the heat generation rate from the inner surface to the outer surface of the blanket is fixed. Therefore we can tabulate the mixed-mean outlet temperature and thermodynamic efficiency as a function of the number of radial zones as shown in Table 2-6. The surface layer is not included in this table. A higher temperature first layer would allow higher ideal efficiencies. The optimum peaking factor is obtained by selecting zone widths to yield the same mixed mean outlet temperature for all zones for a given maximum allowable Li_2O temperature. In this parameterization, it was assumed that the maximum allowable granule temperature is 1270 K based on LiOT transport considerations. (The maximum allowable granule temperature for Li_2O is discussed in more detail in the next section.)

Examination of Table 2-6 shows that above approximately seven zones the increase in efficiency due to adding more zones is small and probably would not justify the added complexity. The radial boundaries for a blanket consisting of a 5 cm thick first layer and seven additional layers are shown in Table 2-7. The nuclear heating deposition profile was used to determine the zone boundaries that would yield the proper value of $\Delta T_{max}/\Delta T_{avg}$, which for this example is 1.3.

In actuality, it may be more effective to allow a greater temperature distribution (and thus a lower outlet temperature) within the zones near the back of the blanket, since the total heat deposited there, and consequently their effect on the overall mixed-mean outlet temperature, is small. In fact, the granules exiting from these zones could be recycled back to the blanket inlet rather than routed to the power conversion system, as shown in Fig. 2-8. These options should be studied further. However, for

TABLE 2-6
THERMODYNAMIC EFFICIENCY DEPENDENCE ON
THE NUMBER OF RADIAL ZONES

Optimum of Zones[a]	Intrazone Peaking Factor	Mixed-Mean Outlet Temperature[b] (K)	Maximum Thermodynamic Efficiency[c] (%)
1	3.7	910	67.0
2	2.2	1000	70.0
3	1.8	1050	71.4
4	1.6	1090	72.4
5	1.4	1130	73.4
7	1.3	1160	74.1
10	1.2	1190	74.9
20	1.1	1230	75.6

[a]Not including first layer.

[b]Assuming an inlet temperature of 770 K and a maximum temperature of 1270 K.

[c]Assuming ideal Carnot efficiency with a 300 K sink.

the present analysis, we assume the same mixed-mean outlet temperatures for each zone.

2.5. MAXIMUM Li$_2$O TEMPERATURE CONSIDERATIONS

The thermodynamic efficiency of the Cascade reactor is limited by the maximum allowable Li$_2$ temperature as was shown in the last section. The maximum allowable temperature is in turn set by the acceptable LiOT loss rate from two perspectives — physical loss of Li$_2$O from the granules, and concerns of compatibility of LiOT with materials commonly used throughout the vacuum system. This section addresses the former issue of mass transport.

The LiOT loss rate from Li$_2$O can be computed given the LiOT partial pressure and the chamber pumping flow rate using the perfect gas law. For LiOT in thermodynamic equilibrium with Li$_2$O and T$_2$O, the LiOT partial pressure, P_{LiOT} in atm,

TABLE 2-7

RADIAL ZONE BOUNDARIES

FOR AN EIGHT ZONE BLANKET[a]

Zone	Inner Radius (m)	Maximum Nuclear Heating (MW/m^3)
1 (First layer)	4.00	37.4
2	4.05	30.6
3	4.19	17.9
4	4.32	10.4
5	4.46	6.1
6	4.59	3.6
7	4.73	2.1
8	4.87	1.2

[a]Peaking factor is 1.3.

can be computed given the temperature, T in K, and the T_2O partial pressure, P_{T_2O} in atm, using (Ref. 2-17)

$$\log P_{LiOT(g)} = -\frac{8635}{T} + \frac{1}{2}\log P_{T_2O(g)} + 4.57 \quad .$$

The T_2O partial pressure is calculated from the tritium generation rate and the chamber pumping flow rate, again using the perfect gas law. The process is iterative in that the LiOT loss rate will impact the necessary chamber pumping rate.

Using the Cascade gas flow rates of Ref. 2-18,

7.5×10^{-6} kg/s T_2 (as T_2O) from Li_2O neutron capture,

9.9×10^{-6} kg/s He from Li_2O neutron capture,

7.1×10^{-6} kg/s He from $D - T$ reaction,

1.9×10^{-5} kg/s unburned $D - T$ gas,

the LiOT mass transport as a function of temperature at 13 Pa chamber pressure was calculated as described above. The results are shown in Table 2-8. The table shows that the LiOT loss rate increases dramatically and becomes a significant fraction of the total volume pumped above 1300 K. Above 1400 K, LiOT becomes the dominant pumped specie corresponding to over 50% of the total volume pumped. On this basis, 1270 K is suggested as the maximum allowable Li_2O temperature for the present vacuum system design. It is recommended that follow on studies examine the compatibility of Li_2O with the materials with which it is expected to come into contact, as this limitation may be more stringent than that of pumping system capacity.

TABLE 2-8
LiOT MASS TRANSPORT
AT 13 Pa CHAMBER PRESSURE

Temperature (K)	LiOT Loss Rate (g/s)	Total Chamber Pumping Rate (ℓ/s)	Fraction LiOT Total Pumped
1000	6.8×10^{-4}	5,800	0.0028
1100	4.1×10^{-3}	6,400	0.017
1200	0.019	7,500	0.074
1300	0.072	9,700	0.23
1400	0.27	17,000	0.53
1500	1.17	51,000	0.83

References for Chapter 2

2-1. J.H. Pitts, "Cascade: A Centrifugal-Action Solid-Breeder Reaction Chamber," *Nuclear Technology/Fusion*, Vol. 4, No. 2, part 3, September 1983, p. 967.

2-2. J.H. Pitts, "Mechanical and Thermal Design of the Cascade Reactor," Lawrence Livermore National Laboratory Report, UCRL-89273; also, *Proceedings of the Tenth Symposium on Fusion Engineering*, Philadelphia, PA, December 1983.

2-3. G.R. Hopkins and R.J. Price, "Fusion Reactor Design with Ceramics," *Nuclear Engineering Design/Fusion,* to be published, 1984.

2-4. Avco Specialty Materials Co., Product literature letter to P. Trester, GA Technologies, November 1983.

2-5. "New Product Information," Dow Corning Corporation, 1983.

2-6. G.R. Hopkins and E.T. Cheng, "Low Activation Fusion Rationale," *Nuclear Technology/Fusion,* Vol. 4, November 1983, p. 528.

2-7. "Fiberfrax-Ceramic Fiber," The Carborundum Company, Niagara Falls, NY, 1979.

2-8. "Min-K Thermal Insulation-Aerospace Insulation," Johns-Manville, Denver, CO.

2-9. "Memorandum Number 11 — Thermophysical Properties of RTG Insulation Components," Jet Propulsion Laboratory, June 1971.

2-10. J.H. Pitts, "Stress Analysis of the Cascade Chamber," *1982 Laser Program Annual Report,* Lawrence Livermore National Laboratory Report UCRL-50021-82, 1983, p. 8-24.

2-11. R.J. Roark, *Formulas for Stress and Strain,* Fourth Edition, McGraw-Hill Book Company, New York, NY, 1965.

2-12. American Institute of Steel Construction, *Manual of Steel Construction,* Seventh Edition, 1970.

2-13. J.H. Pitts, O.R. Walton, and R.L. Creedon, "A High-Temperature, Low-Activation Design for the Cascade Reactor," *Transactions of the American Nuclear Society,* Vol. 46, June 1984; also, Lawrence Livermore National Laboratory Report UCRL-90199SUM, January 1984.

2-14. O.R. Walton, "Granular Flow Considerations in the Design of a Cascade Solid Breeder Reaction Chamber," Lawrence Livermore National Laboratory Report UCID-19903, October 1983.

2-15. E.U. Schlunder, "Particle Heat Transfer," in *Seventh International Heat Transfer Conference,* 1982, Vol. 1, pp. 195-211.

2-16. W. Meier of LLNL, personal communication to H.E. Levine of GA Technologies, June 1983.

2-17. M. Tetenbaum, C.E. Johnson, Chemical Technology Division, Argonne National Lab., paper submitted to the *J. of Nuclear Materials*, May 1983.

2-18. J.H. Pitts, "Vacuum Pumping of the Cascade Reaction Chamber," *1982 Laser Program Annual Report*, Lawrence Livermore National Laboratory Report UCRL-50021-82, 1983, p. 8-26.

3. GRANULE DESIGN AND FABRICATION

3.1. INTRODUCTION

The flowing solid breeder (Li_2O) granule blanket of the 3000 MW(t) Cascade (Ref. 3-1) reactor absorbs the energy produced during laser-induced fusion reactions and transports it to the power conversion system. The first few layers of granules, located closest to the fusion energy source, will experience a surface heat flux which might consist of alpha particles, reflected laser light, X-rays, and pellet debris. In the limiting case, for a product of compressed fuel density and radius of 3 g/cm^2, the latter two sources alone could deposit $\sim32\%$ (Ref. 3-2) of the 600 MJ released during each 2 μs pulse (Ref. 3-3). These first few layers will therefore experience melting, vaporization, and possible cracking, the degree of which could impact the reaction chamber blanket flow dynamics and vacuum pumping requirements. The system power balance could also be affected if vaporization results in significant energy trasport. Because the granule diameter is small, granules that are not directly exposed to the fusion pellet energy yield will experience very little spatial variance in their nuclear heating and correspondingly small thermal stresses. This study therefore examined the thermal and structural effects expected on first layer granules. Cost-effective methods of manufacturing the Li_2O granules were also evaluated.

3.2. GRANULE THERMAL STRESS ANALYSIS

3.2.1. First Layer Granule Dynamics

The pulsed energy released by each D-T pellet microexplosion will subject the surfaces of first layer granules that face the reaction chamber to large successive loads from reflected laser light, X-rays, alphas, and pellet debris. The fraction of

3-1

the total pellet energy yield that is deposited on the granule surface increases with increasing pellet compression. For the reference case in which the pellet compression is 3.0 g/cm², approximately 32% of the pellet energy yield is deposited on the granule surface (Ref. 3-2).

The objectives of our thermal stress analysis were threefold:

1. To determine the feasibility of avoiding melting and vaporization of the first layer granules by increasing the Cascade reaction chamber size.

2. If melting and vaporization cannot be avoided, to determine the amount of melting and vaporization that will occur.

3. To determine the severity of thermal stress-induced cracking and the sensitivity of thermal stress to granule size.

An estimate of the size of the reaction chamber that is required to avoid melting and vaporization can be obtained by using a one-dimensional unsteady-state conduction equation and approximating the first layer granules as a semi-infinite slab. Assuming that the heat flux, $\dot{q}''$, is constant over the duration of the pulse and that the granule is initially at constant temperature, T_O, the granule surface temperature, T_S, can be approximated by

$$T_S = T_O + 1.13 \frac{\dot{q}''}{k} (\alpha t_p)^{1/2}$$

where k is the granule thermal conductivity, α is the thermal diffusivity, and t_p is the pulse duration time (Ref. 4). The heat flux can be approximated by

$$\dot{q}'' \approx \frac{fQ}{t_p A_S}$$

where f is the fraction of the total pellet energy yield that is deposited on the granule surface, Q is the total pellet energy yield, and A_S is the granule surface area of the first layer. For a spherical reaction chamber

$$A_S = 4\pi r_C^2$$

and

$$t_p = \frac{r_C}{V}$$

where r_C is the distance from the microexplosion to the first layer granule surface and V is the velocity of the slowest fusion reaction product (the pellet debris). Combining the above equations and solving for r_C gives

$$r_C = \left[0.09 \frac{fQV^{1/2}\alpha^{1/2}}{k\,(T_S - T_O)} \right]^{2/5}$$

Using the reference Cascade design parameters listed in Table 3-1 and the material properties of Li_2O listed in Table 3-2, the distances r_C that are required between the microexplosion and the first layer granules to avoid melting and vaporization are 42 m and 28 m, espectively. These results indicate that very large reaction chambers are required to avoid melting or vaporization, which implies that this approach is not economically or mechanically feasible. Therefore, some melting and vaporization of first layer granules will occur.

The upper bounds of melting and vaporization were then estimated by assuming that the total energy intercepted by the frontal area of the granules is used strictly to either only melt or to melt and then vaporize material, and that the non-neutron energy is all absorbed at the surface of the granule. It was further assumed that before conducting through the granule, all the surface energy must first raise the solid breeder material to the melting temperature, then melt the material at constant temperature, then raise the material to the vaporization temperature, and finally vaporize the material at constant temperature. The maximum amounts of material, m_m and m_v, which will melt or vaporize are

TABLE 3-1

		Reference
Pellet energy yield, Q	600 MJ	3-1
Frequency	5 Hz	3-1
Non-neutron energy fraction, f	0.32	3-2
Pulse length, t_p	2 μs	3-3
Velocity of slowest fusion reaction products, V	2×10^6 m/s	3-3
Blanket inner radius, r_C	4 m	3-1
Maximum Li$_2$O outlet temperature, T_O	1200 K	3-1
Granule porosity, p	0.05	
Li$_2$O grain diameter, g	5 μm	

$$m_m = \frac{fQ}{H_f + c_p (T_m - T_O)}$$

$$m_v = \frac{fQ}{H_f + H_v + c_p (T_v - T_O)}$$

where H_f is the latent heat of fusion, and H_v is the latent heat of vaporization. Using the values listed in Tables 3-1 and 3-2, the maximum quantity of material that would melt assuming no vaporization is 55 kg. Alternatively, if the incoming energy was instead used completely for vaporization, the maximum quantity of vaporized Li$_2$O is 5.6 kg. In these limiting cases, the maximum melt layer thickness is 74 μm (10% of first layer granules), or that of the maximum vaporization layer is 7 μm (1% of first layer granules). These results are not operationally restrictive and if vaporized material redeposits locally, 2-D thermal analysis presented in the next section shows that the granule would resolidify between pulses.

In reality, the physics pertaining to both the change of state of the solid breeder as the energy of the microexplosion conducts through the granule and the dynamics

TABLE 3-2
Li₂O MATERIAL PROPERTIES

		Reference
Melting temperature, T_m	1706 K	3-5
Vaporization temperature, T_v	2873 K	3-6
Heat of fusion, H_f	1.96×10^6 J/kg	3-6
Heat of vaporization, H_v	2.7×10^7 J/kg	3-7
Density, ρ	2000 kg/m³	3-6
Specific heat capacity, c_p	$2.5179 \times 10^3 + 0.3328\,T$ $-8.382 \times 10^7\,T^{-2}$ J/kg-K	3-8
Thermal conductivity, k	$(1-p)^{1.94} \times$ $(0.022 + 1.784 \times 10^{-4} T)^{-1}$ W/m-K	3-8
Thermal diffusivity at 1706 K, α	4.5×10^{-7} m²/s	3-8
Thermal diffusivity at 2873 K, α	2.5×10^{-7} m²/s	3-8
Young's modulus, E	$140\,\exp(-4p)[1$ $-(T/T_m)\exp(1 - T_m/T)]$	3-8
Tensile strength, σ_t	$108\,g^{-0.4}\exp(-10p) \times$ $[1 - 44\exp(-7000/T)]$ MPa (g in microns)	3-8
Linear thermal expansivity, α_l	$2.0569 \times 10^{-6}\,T^{0.4}$ K^{-1}	3-8
Poisson's ratio, ν	0.25	3-8

of the ablated material blow-off and potential granule shock formation are extremely complex. However, by estimating some fundamental time constants, a rough estimate of the magnitude of granule dynamics can be obtained.

The first layer granules could fracture from either mechanical or thermal stresses. The mechanical stresses are caused by the compressive shock wave from the pulsed energy deposition. The shock wave travels through the granule, then reflects back

in tension. Because ceramics such as Li_2O are much stronger in compression than tension and the granule is assumed to be unconstrained at the surface, fracture from mechanical stresses would probably occur in the back of the granule. The thermal stresses are caused by the sudden surface heating of the granule, which causes a thin layer on the front face to expand. This expansion will cause pulling on the rest of the granule, putting it in tension. Fracture from thermal stresses would probably occur along the front face of the granule, where the thermal gradient is highest. In this work, only the thermal stresses were analyzed.

The coupling of the mechanical and thermal stresses can be neglected if the parameter H is much less than one where

$$H = \left(\frac{t_M}{t_T} \cdot \frac{t_M}{t_P} \right)^{1/2}$$

and t_M and t_T are the characteristic mechanical and thermal relaxation times (Ref. 3-9). The parameter H compares the mechanical relaxation time to the thermal relaxation time and pulse length. The characteristic relaxation times are defined by

$$t_M = \frac{L}{c_S}$$

and

$$t_T = \frac{L^2}{\alpha}$$

where L is the characteristic length, i.e., the granule radius, c_S is the wave propagation speed in the solid, and α is the thermal diffusivity. The wave propagation speed can be defined as (Ref. 3-9)

$$c_S = \left(\frac{E}{\rho} \right)^{1/2}$$

where E is Young's modulus. Assuming a 2 mm diameter Li_2O granule with a pulse duration time of 2.0×10^{-6} s, $c_S = 5.6 \times 10^3$ m/s and $\alpha = 6.7 \times 10^{-7}$ m^2/s. Substituting into the expressions for the characteristic relaxation times and the parameter H yields, $t_M = 1.8 \times 10^{-7}$ s, $t_T = 1.5$, and $H = 1.0 \times 10^{-4}$ s, which is much less than one. This implies that the transient thermal stresses and mechanical stresses can be handled independently.

The comparison of characteristic times can also be used to determine if first row granules will experience significant shock waves as the surface material vaporizes. If the characteristic mechanical relaxation time is longer than the gas expansion time, then it can be expected that the ablation would occur with shock formation. The gas expansion time is estimated by

$$t_g \simeq \frac{L}{c_g}$$

where c_g is the gas propagation speed.

The speed of sound in a gas can be used as an upper bound. Using the ideal gas law, the speed of sound becomes

$$c_g = \left(\frac{\gamma R T_v}{M} \right)^{1/2}$$

where γ is the ratio of the specific heat at constant pressure to the specific heat at constant volume, R is the gas constant, T_v is the vaporization temperature, and M is the molecular weight of the solid breeder. For a polyatomic ideal gas, $\gamma = 4/3$, and $c_g = 1000$ m/s. Letting the characteristic length equal the vaporization depth and using the maximum ablation depth and mass calculated earlier, $t_g = 7.0 \times 10^{-9}$ s. This is approximately twenty-five times faster than the mechanical relaxation time. In actuality, the vaporization depth will be less than the maximum vaporization depth, decreasing the gas time. Because the gas expansion time is much shorter than the mechanical time, the vaporized material should ablate with shock formation. However,

3-7

it is expected that the shock wave would generate stresses within the granule which would be relieved and dissipated into the porous blanket. It is also noted that the gas expansion time is much shorter than the pulse duration time, sufficiently reducing the density of the ablated material so that vapor shielding of the gammas and pellet debris from the granule will be small.

3.2.2. Two Dimensional Thermal and Structural Computer Analysis

The transient temperature distribution of a Cascade reactor first layer granule was calculted using TACO2D (Ref. 3-10), a two dimensional, finite element heat transfer code. The temperature distribution at the end of the pulse was coupled into NIKE2D (Ref. 3-11), a two-dimensional, implicit, finite deformation, finite element stress code, to determine the stress in the granule. The transient analysis was also used to determine if melted or vaporized material would recondense between pulses.

Figure 3-1 displays the two-dimensional mesh that was used in our analysis. The analysis assumed that the surface of the granules facing the microexplosion will undergo the dynamics described in Sec. 3.2.1.

The thermal stresses at the end of the pulse duration time were calculated by coupling the thermal output from TACO2D into NIKE2D. The end of the pulse duration time was examined because it is expected that this is when the largest thermal gradient and thus the largest thermal stresses will occur. The granule's center of mass was constrained from moving in any direction, but surface motion was unconstrained.

Figures 3-2 and 3-3 present the thermal stress contours of a 2 mm and 1 mm diameter first layer Li_2O granule. Table 3-3 summarizes the information contained in these figures. The maximum tensile stress for both sizes of granules is almost 50 times greater than its fracture strength. However, this stress occurs only within a small region on the side of the ball, and will probably result only in local chipping A more important stress figure of merit is found by estimating the maximum tensile
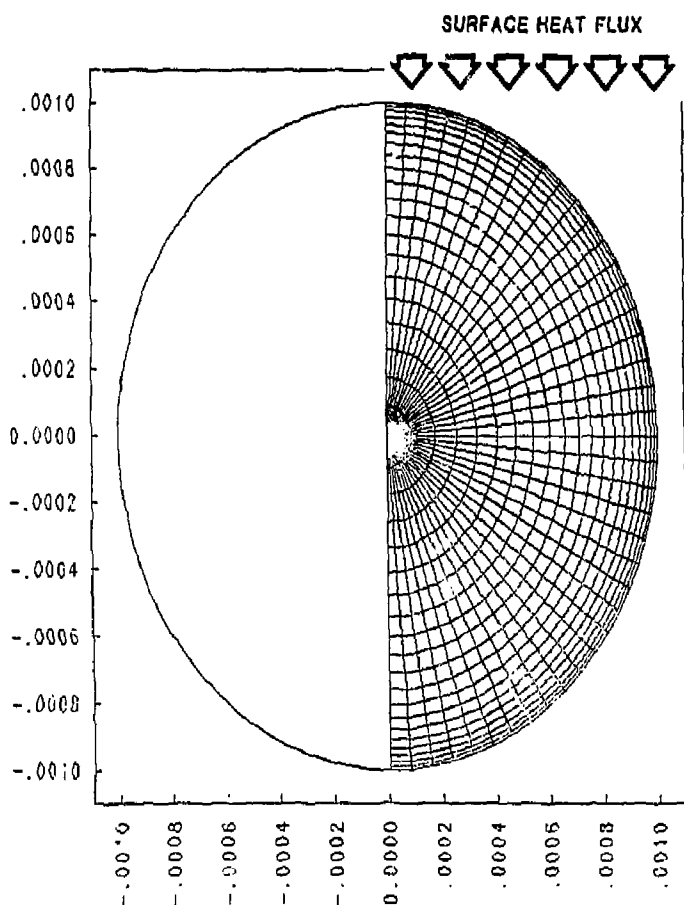
Fig. 3-1. Mesh used for the computer analysis of first layer granules

ICF MICROSPHERE THERMAL STRESS
CONTOURS OF MAXIMUM PRINCIPAL STRESS

MIN(N)=-1.17E+09
MAX(X)= 1.30E+09
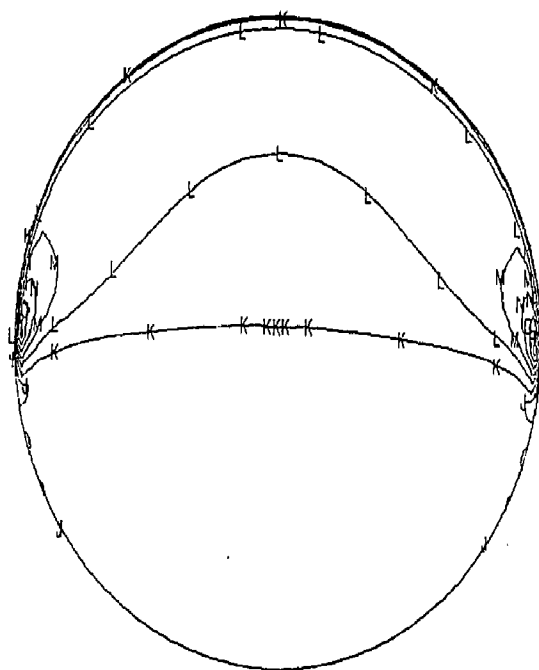
CONTOUR LEVELS

A =-1.05E+09
B =-9.34E+08
C =-8.16E+08
D =-6.99E+08
E =-5.81E+08
F =-4.63E+08
G =-3.45E+08
H =-2.27E+08
I =-1.09E+08
J = 0.
K = 1.26E+03
L = 2.44E+08
M = 3.62E+08
N = 4.80E+08
O = 5.98E+08
P = 7.15E+08
Q = 8.33E+08
R = 9.51E+08
S = 1.07E+09
T = 1.19E+09

Fig. 3-2. Thermal stress contours of a 2 mm first layer Li_2O granule.

3-10

ICF MICROSPHERE THERMAL STRESS
CONTOURS OF MAXIMUM PRINCIPAL STRESS

MIN(N)=-1.19E+09
MAX(X)= 1.34E+09
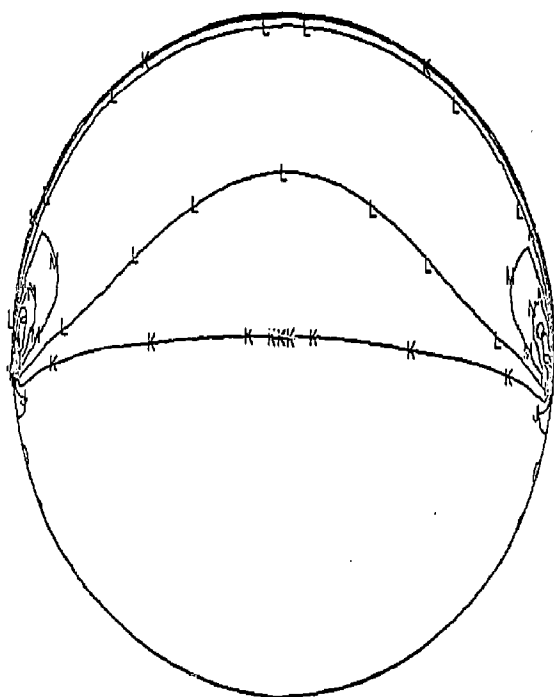
CONTOUR LEVELS

A =-1.07E+09
B =-9.53E+08
C =-8.32E+08
D =-7.12E+08
E =-5.91E+08
F =-4.71E+08
G =-3.50E+08
H =-2.30E+08
I =-1.09E+08
J = 0.
K = 1.32E+08
L = 2.53E+08
M = 3.73E+08
N = 4.94E+06
O = 6.14E+08
P = 7.35E+08
Q = 8.55E+08
R = 9.76E+08
S = 1.10E+09
T = 1.22E+09

Fig.3-3. Thermal stress contours of a 1 mm first layer Li_2O granule.

stress contour that dissects the granule. When this contour exceeds the fracture strength, he granule will fragment. Both the 2 and 1 mm diameter ball maximum tensile stress contour exceed the Li_2O fracture strength, by about a factor of ten. Therefore, it is anticipated that first layer granules will crack into large fragments with some chipping along the sides.

TABLE 3-3
THERMAL STRESS FOR
2 AND 1 mm DIAMETER GRANULES

Granule diameter (mm)	2	1
Maximum tensile stress (MPa)	1300	1340
Maximum compressive stress (MPa)	1170	1190
Maximum tensile stress contour that dissects the granule (MPa)	303	313

Li_2O fracture strength at 1200 K = 30 MPa

The thermal stresses decreased with increasing granule diameter because larger granules have more material on which to react the expansion force of the surface facing the microexplosion. However, stress dependence on granule diameter was not strong, as the tensile stresses decreased by only 3% from 1 mm to 2 mm diameter.

Figure 3-4 presents the temperature profile within the granule immediately before the next pulse. The figure shows the granule temperature is below the 1700 K Li_2O melt temperature everywhere except for a very thin region facing the original energy flux direction. Since the initial temperature chosen for this granule was a uniform 1200 K, (i.e., just before exit from the reaction chamber but ignoring temperature gradients from previous pulses), it is concluded that first layer granule material will solidify between pulses. In addition, the orientation of a granule would most likely be altered between pulses, enhancing heat transfer to granules within the blanket.

ICF MICROSPHERE TEMPERATURE CONTOURS (C)
ISOPLOT AT TIME 2.0000E-01

MINIMUM AT • =
9.318E+02

MAXIMUM AT + =
1.701E+03

AVERAGE =
1.036E+03

CONTOUR LEVELS
A = 9.500E+02
B = 9.750E+02
C = 1.000E+03
D = 1.025E+03
E = 1.050E+03
F = 1.075E+03
G = 1.100E+03
H = 1.125E+03
I = 1.150E+03
J = 1.175E+03
K = 1.200E+03
L = 1.225E+03
M = 1.250E+03
N = 1.275E+03
O = 1.300E+03
P = 1.325E+03
Q = 1.350E+03
R = 1.375E+03
S = 1.400E+03
T = 1.425E+03
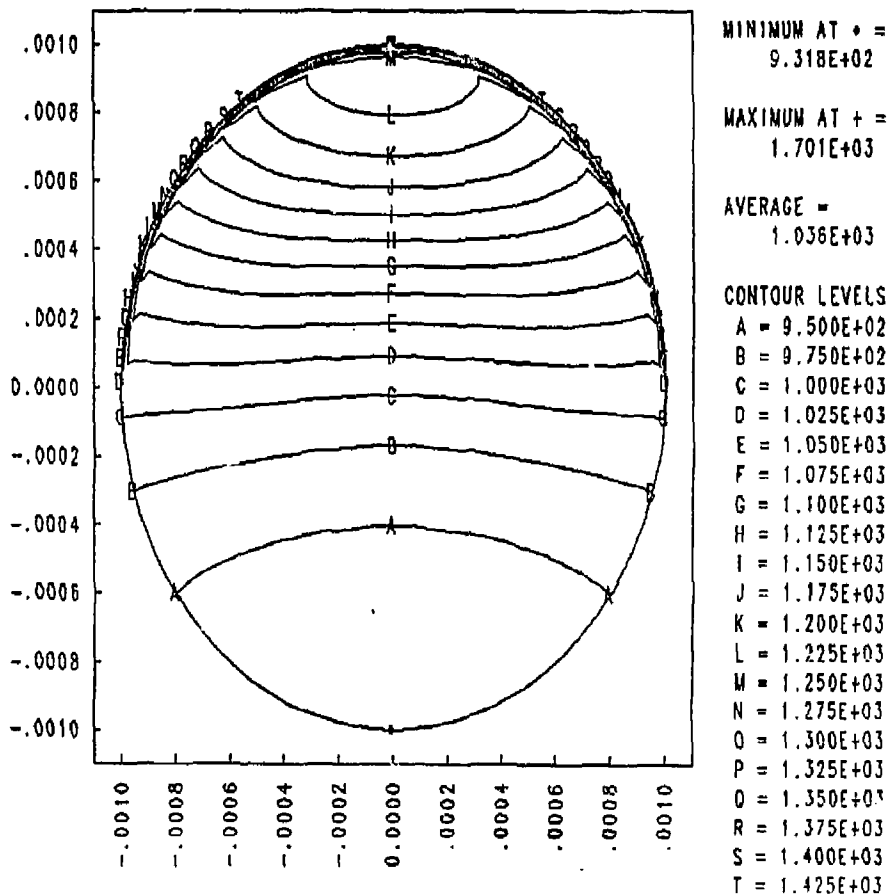
Fig. 3-4. Temperature profile of a 2 mm first layer Li_2O granule just before the next pulse. Note that temperature contours are in °C.

3.2.3. Thermal Stress Analysis Conclusions

Based on the thermal and structural analysis of the first layer Li_2O granules presented above, we conclude:

1. It is not feasible to avoid melting and vaporization by increasing the size of the reaction chamber. Therefore, reactor designs should account for some melting and vaporization of first layer granules.

2. A maximum of 10% of each first layer granule will melt from the absorption of the energy from a single microexplosion. However, the bulk temperature rise of the granule is not significant, and the granule material will resolidify between pulses.

3. The maximum vaporization layer that will blow off into the reaction chamber is 7 microns thick, containing a total of 5.6 kg of Li_2O. This analysis assumed that this material is deposited locally as an upper limit to the thermal stress. This assumption needs to be verified as the otherwise-implied mass and energy transport could impact the reaction chamber vacuum pumping requirements and system power balance.

4. The thermal stress contours that dissect the granule are approximately ten times greater than the fracture strength. Therefore, it is anticipated that first layer granules of the present design will crack into large fragments with chipping expected along the sides of the granule where local stresses are much higher.

5. Based on cost data presented in Section 3.3 below, the cost of continuously refabricating the broken particles would be high. Two alternatives are available which avoid refabrication. One alternative is to not refabricate cracked granules and thus operate with a powdered blanket. However, analysis of the flow dynamics of a powdered blanket would require a significant, parallel experimental program. The second alternative is to incorporate a special surface layer of granules which would exhibit improved response to the thermal and stress effects. Silicon carbide (CVD), with a factor of seven lower thermal expansion coefficient, a factor of ten to twenty greater

irradiated fracture strength, and a factor of ten greater thermal conductivity, would be an excellent candidate material for this special layer.

We expect that SiC would experience at least a factor of eight lower thermal stress than Li_2O and thus would not fracture. Lar or h low SiC granules would *float* on top of the Li_2O granules, providing a protective layer.

6. The granule tensile thermal stresses decreased with increasing diameter. However, the stress dependence on granule diameter was not strong. Therefore. granule size should be determined by ease of manufacturing, heat transfer, tritium retention, and cost.

3.3. LITHIUM OXIDE GRANULE FABRICATION PROCESSES

3.3.1. Introduction

Three processes for the fabrication of lithium oxide granules have been identified which should be cost effective in the manufacture of the granules. One process, the VSM process (Ref. 3-12), is based on melting and spheroidizing irregularly-shaped lithium oxide feed granules. The second process, the lithium hydroxide process, is one patented by Research Dynamics Inc. (Ref. 3-13), which spheroidizes liquified lithium hydroxide, but would use GA's sphere forming technology. The third process is a lithium carbonate sol-gel process proposed herein based on sol-gel technology developed for making spherical fuel particles for the High Temperature Gas-Cooled Reactor (HTGR).

The processes are described in the following sections. Block flow diagrams of the processes are shown in Figs. 3-5, 3-6, and 3-7, and a cost estimate summary for fabrication of the granules is shown in Table 3-4.

IRREGULAR Li_2O
FEED GRANULES

VACUUM FURNACE
570 K, 0.3 Pa — IMPURITY REMOVAL — H_2O, CO_2

VSM FURNACE
1900 K TO 2000 K — SPHEROIDIZE AND COOL

SCREEN — FINES — PELLETIZER

OVERSIZE — CRUSHER
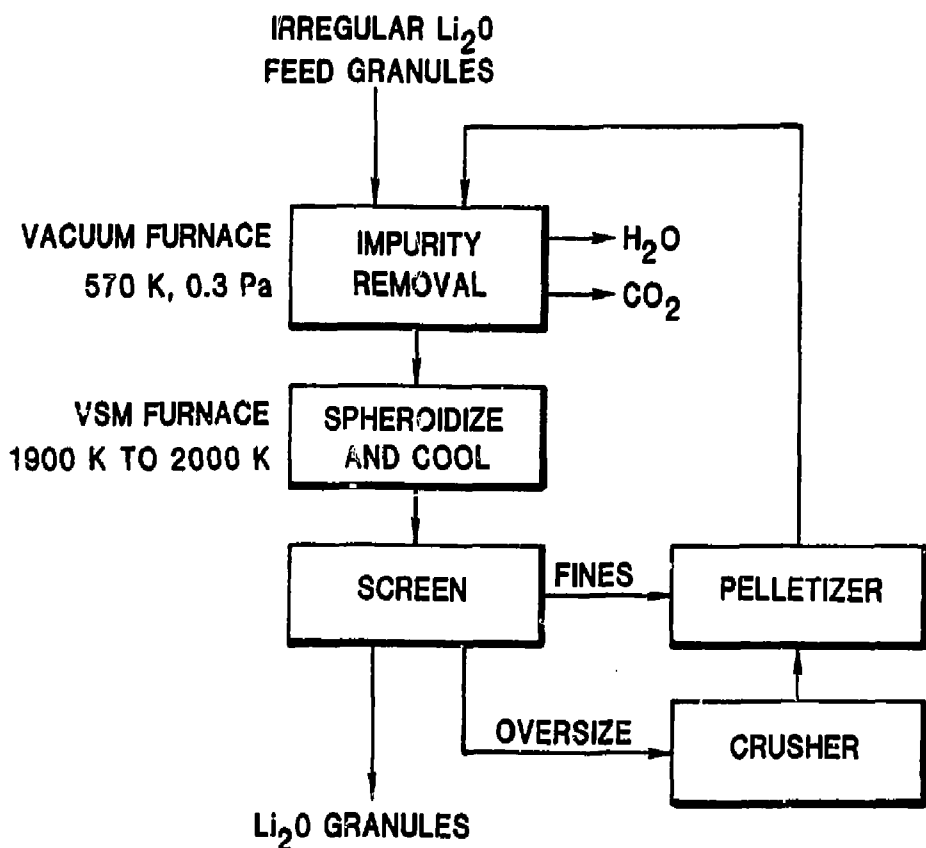
Li_2O GRANULES

Fig. 3-5. Li_2O granule fabrication — VSM process flow diagram.

LIOH · H_2O

MELTER, 870 K | LIOH MELTING | → H_2O → CO_2

PULSED SPHEROIDIZING NOZZLES
COUNTER-CURRENT SOLIDIFICATION COLUMN 870 K | SPHEROIDIZE AND COOL

VACUUM FURNACE
470 K, 0.3 Pa | LIOH TO Li_2O CONVERSION | → H_2O

VERTICAL TUBE SINTERING FURNACE
1200 K TO 1400 K | SINTER Li_2O GRANULES
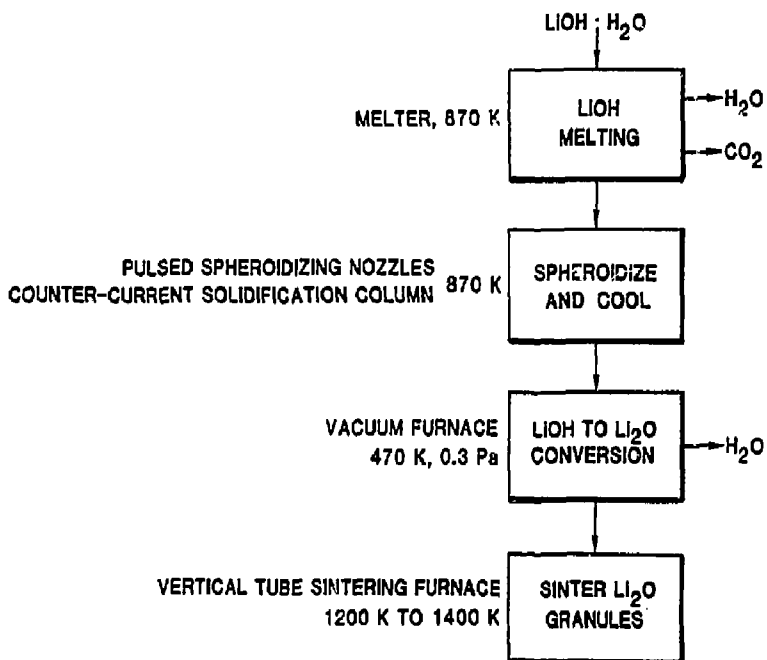
Fig. 3-6. Li_2O granule fabricatiaon — LiOH method process flow diagram.
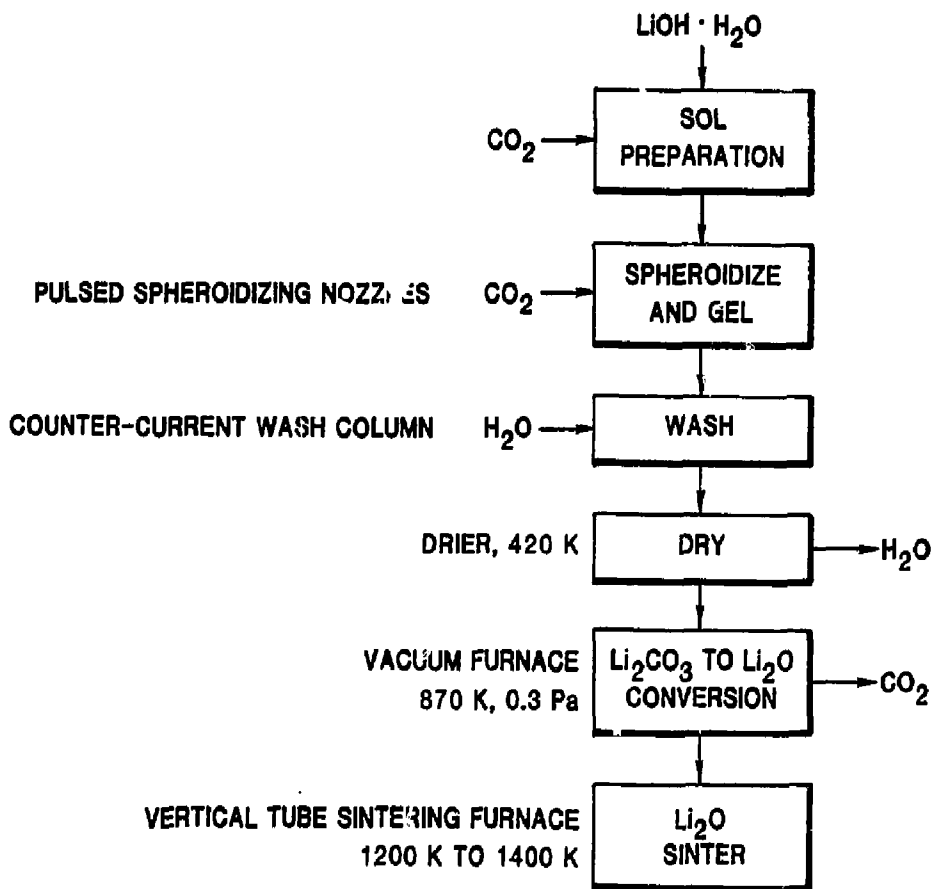
Fig. 3-7. Li_2O granule fabrication — Li_2CO_3 sol-gen process flow diagram.

TABLE 3-4
Li$_2$O GRANULE FABRICATION COST SUMMARY

	Costs in \$/kg Li$_2$O		
	VSM Process	LiOH Process	Li$_2$CO$_3$ Process
Labor	13	15	17
Raw materials	150	33	17
Energy at \$0.07/kW-hr	0.32	0.69	0.93
Depreciation	1.6	1.6	2.3
Total	170	50	37
Refabrication (Total minus raw materials)	15	17	20

3.3.2. VSM Drop-Melt Furnace Process

This process requires high purity lithium oxide granules as feed material to the melt-spheroidizing furnace. Since lithium oxide readily absorbs water and carbon dioxide. it would probably be contaminated with these impurities during transportation and handling of the material. Thus, a process step to remove these impurities before spheroidizing in the VSM furnace will be required.

Cost of the high purity lithium oxide granules, in the size range of 1.4 mm to 2.3 mm (8 to 12 mesh), is the major cost item of this process. This makes it noncompetitive with the other two processes for fabrication of the initial charge of granules for the reaction chamber. However, for the refabrication mode of operation where broken granules are recycled to the granule fabrication line, it could be the lowest cost process, as shown in Table 3-4.

The major process steps of the VSM process (Fig. 3-5) are described below.

1. Water and carbon dioxide are removed from the lithium oxide granules by heating in a vacuum furnace to 570 K (300°C) at a vacuum of 0.3 Pa (2 microns of mercury).

2. The irregularly shaped feed granules are converted to spherical granules by melting as they drop through the hot zone of a VSM furnace operating at a temperature of 1900 K to 2000 K. The spheres solidify by cooling below the Li_2O melting point (1700 K) in the cold zone at the bottom of the furnace.

3. The spherical lithium oxide granules are segregated into specific sizes by screening in a sonic sifter.

4. Oversize granules are recycled by crushing and conversion back to smaller granules in a pelletizer.

5. Undersize graules are recycled directly to the pelletizer.

6. After crushing, the recycle material is added to the feed stream to the vacuum furances.

7. Broken granules from the reaction chamber would be processed the same way as recycle material.

3.3.3. Lithium Hydroxide Process

This process requires high purity lithium hydroxide as the feed material to the granule forming equipment. Water and carbon dioxide impurities are removed by the process, but nonvolatile and metallic impurities would remain in the product granules. Thus, the cost of the lithium hydroxide for this process is also the major cost item for initial or make-up granules, but very much less than for the lithium oxide for the VSM process.

Following are the major process steps for this process (Fig. 3-6):

1. The lithium hydroxide is melted by heating to about 870 K (melting point ~730 K).

2. The liquid lithium hydroxide is transferred to the spheroidizing feed tank, also at a temperature of 870 K.

3. The liquid lithium hydroxide is pumped at a constant rate to spheroidizing nozzles at the top of a cooling tower.

4. The spherically-shaped lithium hydroxide granules are solidified by a counter-current flow of argon gas in the cooling tower.

5. The solidified granules are collected at the bottom of the cooling tower and transferred to batch acuum furnaces.

6. The spherical lithium hydroxide granules are converted to lithium oxide in the vacuum furnace operating at a temperature of 370 K and a pressure of 0.3 Pa (2 microns of mercury).

7. The lithium oxide granules are sintered to high density by heating in a sintering furnace to approximately 1200 K to 1400 K in an argon atmosphere.

3.3.4. Lithium Carbonate Process

The lithium carbonate process has the potential of using commercial grade lithium hydroxide as the raw material for the process since water soluble impurities in the lithium hydroxide feed, such as alkali and alkaline earth elements (K, Na, Mg, Ca, etc.) would be removed during the gelled sphere washing step of the process. Volatile impurities would also be removed during the conversion step to lithium oxide as in the lithium hydroxide process. Thus, raw material costs for this process should be the lowest of the three processes.

The lithium carbonate process consists of the following major steps (Fig. 3-7):

1. Lithium hydroxide dissolved in water is reacted with carbon dioxide to form a lithium carbonate sol.

2. The sol is pumped at constant rate to spheroidizing nozzles at the top of a gelling column.

3. The lithium carbonate granules from the sphering nozzles are gelled in a column of carbon dioxide gas and collected in a carbonic acid solution.

4. The granules are washed in a counter current wash column with water or aqueous carbonate solution.

5. Washed granules are dried in a continuous drying oven at temperatures up to 420 K.

6. Dried lithium carbonate granules are converted to lithium oxide in a batch vacuum furnace at a pressure of about 0.3 Pa (2 microns of mercury) and a temperatur of 870 K

7. The lithium oxide granules are then sintered to about 90% to 95% of theor ___ l density in a vertical tube furnace at a temperature of 1270 K in an argon atmosphere.

3.3.5. Cost Basis

The costs presented in Table 3-4 are based on actual GA operating experience with the VSM furnace in the manufacturing of HTGR granules, and sol-gel processes used in the manufacturing of HTGR alumina, and lithium aluminate granules. Raw material cost of the Li_2O is based on estimates of commercial scale purification and vacuum-dewatering of LiOH obtained from Ref. 3-14, and other materials costs from Ref. 3-15. Chemical plant equipment costs were obtained by following standard industry practice (Ref. 3-16), and assuming a 1 MT a day plant. The fabrication costs shown in Table 3-4 should be used only on a comparison basis and would cha__ge the cost of high purity lithium compounds were reduced by large production demands. Labor costs for all three processes would be expected to drop based on normal learning curves for new production facilities and cost-sharing of personnel with other fusion-related tasks at the power plant. The processes are nearly automated to current

U.S. practice and no additional major cost reductions are foreseen through further automation.

References for Chapter 3

3-1. J.H. Pitts, "Cascade: A Centrifugal-Action Solid-Breeder Reaction Chamber," *Nuclear Technology/Fusion*, Vol. 4, No. 2, part 3, p. 967, September 1983.

3-2. M.J. Monsler, J. Hovingh, D.L. Cook, T.G. Frank, and G.A. Moses, "An Overview of Inertial Fusion Reactor Design," *Nuclear Technology/Fusion*, Vol. 1, July 1981, p. 316.

3-3. J. Hovingh, "Heat Transfer in Inertial Confinement Fusion Reactor Systems," *Nuclear Engineering and Design* 68, 1981, p. 286.

3-4. J.R. Welty, C.E. Wicks, and R.E. Wilson, *Fundamentals of Momentum, Heat, and Mass Transfer*, New York: John Wylie and Sons, p. 318.

3-5. M. Abdou *et al.*, "Blanket Comparison and Selection Study," Argonne National Laboratory Report, ANL/FPP-83-1, October 1983, p. VIII-4.

3-6. K. Tanaka *et al.*, "Tritium Recovery of the Fusion Reactor of Lithium Oxide Blanket," Int. Conf. Rad. Effects and Tritium Tech. for Fusion Reactors, CONF 750989, 1975, p. III-256.

3-7. O.H. Krikorian, Private Communication to J. Pitts, LLNL Internal Memo, October 27, 1982.

3-8. R.W. Werner, F.L. Ribe, *et al.*, "Synfuels from Fusion — Using the Tandem Mirror Reactor and a Thermochemical Cycle to Produce Hydrogen," Lawrence Livermore National Laboratory Report UCID-19609, November 1, 1982, p. 146-149.

3-9. J.A. Dalessandro, "First Wall Thermal Stress Analysis for Suddenly Applied Heat Fluxes," Proceedings of the Third Topical Meeting on the Technology of Controlled Nuclear Fusion, Santa Fe, New Mexico, May 9-11, 1978, CONF-780508, p. 358.

3-10. W.E. Mason, Jr., "TACO — A Finite Element Heat Transfer Code," Lawrence Livermore National Laboratory Report UCID-17980, Rev. 1, 1980.

3-11. J.O. Hallquist, "NIKE2D — A Vectorized Implicit, Finite Deformation, Finite Element Code for Analyzing the Static and Dynamic Response of 2-D Solids," Lawrence Livermore National Laboratory Report UCID-19677, 1983.

3-12. R.C. Noren, "Fabrication of Li_2O Microspheres," GA Technologies Internal Memo to H.E. Levine, August 8, 1983.

3-13. J.H. Anno, "Method of Producing Porous Lithium Oxide," U.S. Patent No. 4,221,774 to Research Dynamics Inc., September 9, 1980.

3-14. L. Yang, GA Technologies personal communication, August 5, 1983.

3-15. Chemical Marketing Reporter, Schnell Publishing Co., Inc., New York, NY, published weekly.

3-16. Perry, Chilton, and Kirkpatrick, "Perry's Chemical Engineers' Handbook," 4th Edition. McGraw-Hill, 1963.

4. TRITIUM INVENTORY AND RECOVERY

4.1. INTRODUCTION

In the Cascade (Ref. 4-1) approach to fusion power, a bed of high-temperature (~1200 K) solid Li_2O or other lithium-ceramic granules is centrifugally held against the walls of a rotating, double-cone shaped chamber. Within the chamber, the granules absorb the neutrons released from laser-induced fusion reactions, producing thermal energy and tritium. The granules are circulated to transport the energy to the power conversion system. Tritium is recovered by the vacuum system which sustains the chamber vacuum. This section describes how tritium inventory and recovery issues affect key design features of the Cascade concept.

Tritium, bred by neutron capture in the Li_2O, undergoes a three-step process before its recovery by the vacuum system. The first is bulk diffusion within the granule. There is considerable controversy at the present time on the chemistry of tritium migration mechanisms in the Li_2O solid breeder. The uncertainty centers around the chemical form in which the tritium will be released from the Li_2O. Some studies of tritium release from neutron-irradiated Li_2O (*e.g.*, Refs. 4-2 and 4-3 and references therein) indicate that the tritium is released in the oxide form (T_2O), whereas other preliminary studies in which the tritium recovery is performed *in-situ* (Refs. 4-4 and 4-5) indicate released tritium is in the elemental form. Experiments of tritium recovery from Li_2O under the conditions expected in Cascade have not been performed. Based on the lesser uncertainty at this time of Refs. 4-2 and 4-3, this analysis assumes that the release occurs in the T_2O form. The second step in the recovery process is desorption of the T_2O at the granule surface. This is assumed to be an instantaneous process. The final step is percolation of the T_2O through the interstices in the packed granule blanket.

The reference design characteristics of the Cascade concept are presented in Table 4-1. The objectives of this initial study were to investigate tritium inventory sensitivity and dependence on the following design characteristics:

- Granule radius in the range of 0.01 mm to 10 mm.
- Blanket porosity from 0.4 to 0.6.
- Breeder temperature distribution from 800 K to 1700 K.
- Vacuum chamber tritium partial pressure from 0.13 Pa to 13 Pa.

The results of the parametric analyses then formed the basis for establishing the tritium recovery requirements and the recommended recovery method.

TABLE 4-1
CASCADE REFERENCE DESIGN
CHARACTERISTICS

Thermal power	3000 MW
Granule radius	0.5 mm
Average breeder temperature	1000 K
Blanket porosity	50%
Vacuum-chamber total pressure	13 Pa
Vacuum-chamber T_2O pressure	1.3 Pa
Tritium breeding ratio	1.3
Total Li_2O mass, including Li_2O circulating outside the reaction chamber	10^6 kg

4.2. TRITIUM ANALYSIS CODE – TRIT4

The approach taken to accomplish the objectives listed above was to use the GA TRIT4 code, a one-dimensional extension of the steady-state TRIT3 code (Ref. 4-6) to determine the tritium inventory in the Li_2O breeder blanket. The TRIT4 code models tritium inventory in the following principal modes:

- Bulk diffusion inventory within the granule.
- Soluble inventory within the solid Li_2O.
- Porous diffusion inventory in the interstices among the granules.

The bulk diffusion inventory is calculated from the tritium generation rate and temperature profiles in the blanket, the granule size, and Fick's law, using the diffusion coefficient data of Nasu *et al.*, (Ref. 4-7). An expression for the average tritium concentration in a granule is obtained by integrating the steady-state tritium concentration profile for a sphere over the radius and is expressed as (Ref. 4-8)

$$\text{Bulk diffusion inventory} = \frac{S r_M^2}{15 D} \times V_B$$

where S is the tritium generation rate (Ref. 4-9), kg/m^3, r_M is the granule radius, m, D is the bulk diffusion coefficient, m^2/s, and V_B is the solid Li_2O volume, m^3. A plot of the diffusion coefficient data of Nasu *et al.*, (Ref. 4-7) versus temperature is shown in Fig. 4-1.

The gaseous T_2O pressure profile within the blanket is calculated using a percolation model of porous diffusion (Ref. 4-11). Tritium released at the surface of a granule must travel through the interstices among the blanket granules before reaching the chamber vacuum system. This hold-up will create a concentration profile within the blanket. This profile, plus the T_2O partial pressure within the vacuum chamber, constitutes the porous diffusion. More importantly, the porous diffusion inventory directly influences the solubility concentration within the granule by affecting the tritium concentration at the granule surface.

The solubility inventory of tritium in the form of LiOT in the solid Li_2O is determined by the thermodynamic equilibrium of the reaction

$$Li_2O_{(s)} + T_2O_{sol} \rightleftarrows 2LiOT_{sol}$$
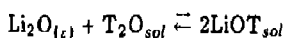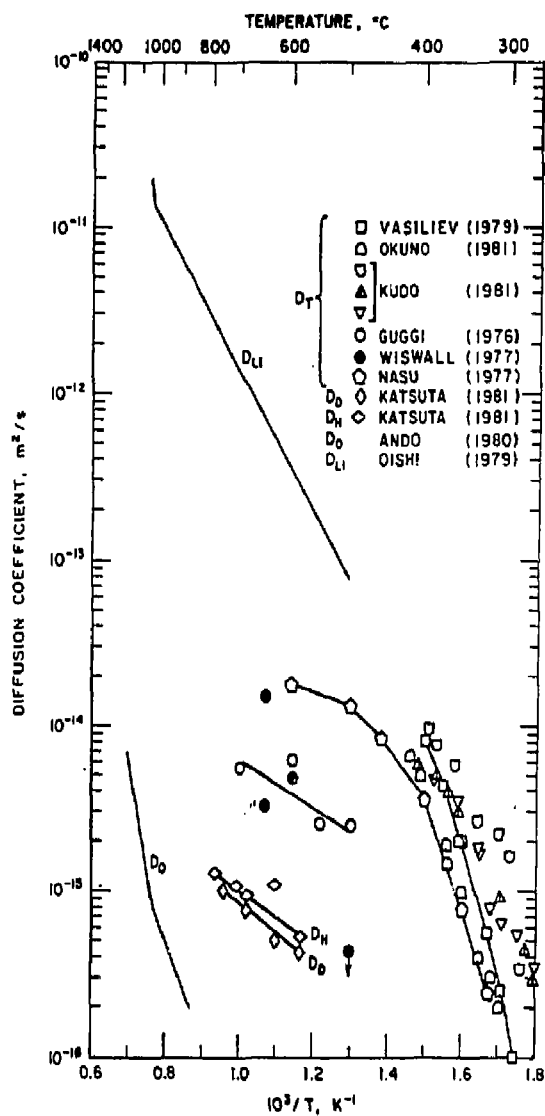
Fig. 4-1. Temperature dependence of bulk diffusion coefficients of tritium, oxygen, lithium, hydrogen, and deuterium in Li₂O. (Reproduced from Ref. 3-10.) The data of Nasu (Ref. 3-7) was used in the present analysis.

TEMPERATURE, °C

1400 1000 800 600 400 300

DIFFUSION COEFFICIENT, m²/s

10⁻¹⁰ 10⁻¹¹ 10⁻¹² 10⁻¹³ 10⁻¹⁴ 10⁻¹⁵ 10⁻¹⁶

D_{LI}

D_O

D_H

D_D

D_T {
□ VASILIEV (1979)
△ OKUNO   (1981)
△
△ } KUDO   (1981)
▽

○ GUGGI   (1976)
● WISWALL (1977)
○ NASU   (1977)
D_O ◇ KATSUTA (1981)
D_H ◇ KATSUTA (1981)
D_O ANDO   (1980)
D_{LI} OISHI   (1979)

0.6 0.8 1.0 1.2 1.4 1.6 1.8

10³/T, K⁻¹

The equilibrium solubility constant, K_p, for this reaction is given in Ref. 4-12 as a function of temperature by the expression

$$\log K_p = -\frac{7073}{T} + 2.102\log(T) - 0.00254T + 2.767$$

where T is the temperature in K and K_p is expressed in atmospheres. The chemical activity of LiOT can then be obtained using

$$a_{\text{LiOT}} = \left(\frac{P_{T_2O}}{K_p}\right)^{1/2}$$

for the given T_2O partial pressure given in Table 4-1. The mole fraction of LiOT, χ_{LiOT} is then given by

$$\chi_{\text{LiOT}} = \frac{a_{\text{LiOT}}}{\gamma_{\text{LiOT}}}$$

where γ_{LiOT} is the activity coefficient. The activity coefficient was recently evaluated by Norman and Hightower (Ref. 4-13), and is shown in Fig. 4-2. The ratio of tritium to lithium atoms is determined from the mole fraction using

$$\frac{\text{atoms of T}}{\text{atoms of Li}} = \frac{\chi_{\text{LiOT}}}{2 - \chi_{\text{LiOT}}}$$

The tritium inventory in kilograms then follows directly from the above and the Li_2O inventory listed in Table 4-1.

4.3. TRITIUM ANALYSIS RESULTS

The total steady-state tritium inventory of the Cascade reactor, granule transport, and power conversion system is 6 kg assuming an average Li_2O temperature of 1000 K. The steady-state radial profile of the tritium inventory with the in-chamber
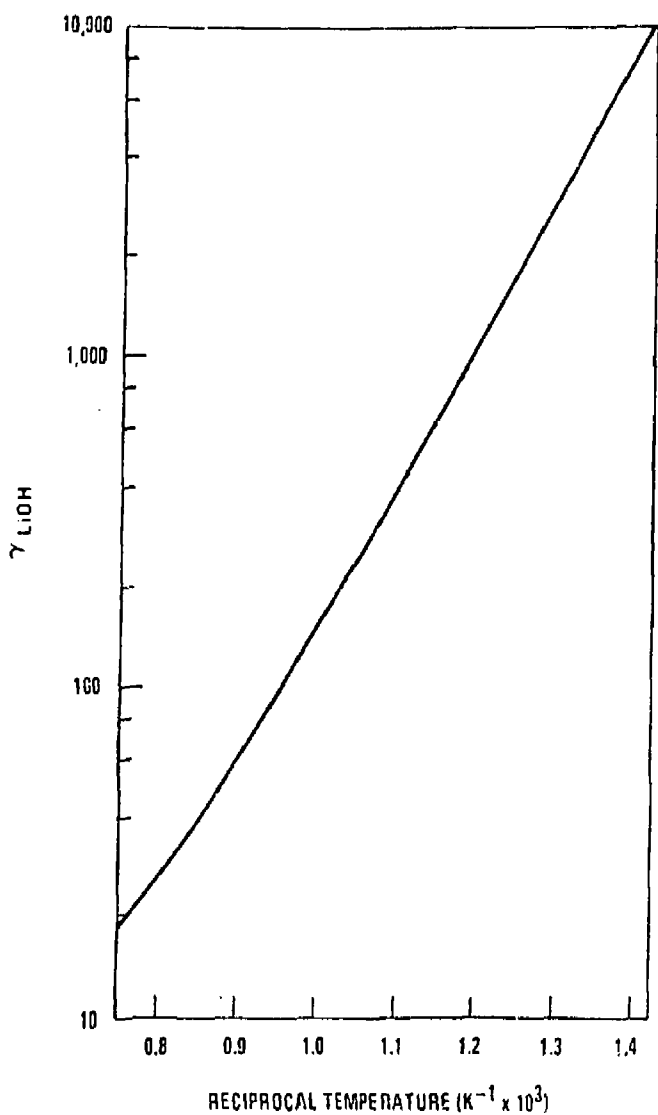
Fig. 4-2. Activity coefficient of LiOH versus temperature, experimentally determined by Norman and Hightower in Ref. 3-13.

4-6

Cascade Li_2O blanket is shown in Fig. 4-3. The inventory is expressed in kilograms of tritium per centimeter of radial blanket thickness. The figure shows that the major contributors are the bulk diffusion and solubility inventories. Bulk diffusive tritium inventory is highest nearest the inner surface of the blanket, following the radial dependence of the tritium generation rate. The porous diffusion inventory is highest near the outer radius because the tritium must flow toward the center of the chamber. The porous diffusion contribution to the total inventory is negligible, but its magnitude is nonetheless important through the square-root dependence of the soluble inventory on the T_2O overpressure profile. The soluble inventory is highest toward the outer radius of the blanket because it follows the porous diffusion inventory.

The values of the diffusion coefficient shown in Fig. 4-1 indicate that the time scale for bulk diffusion will be long relative to the approximately one minute residence time of a granule within the chamber. In addition, upon exit from the reaction chamber, the solid breeder granules will experience agitation during transport to the power conversion system. These effects will probably eliminate the percolation pathway and reduce the porous concentration profile to that due to the vacuum chamber T_2O partial pressure, thus reducing the soluble and porous diffusion inventories. Assuming that all the tritium generated in the blanket is in the oxide form, the T_2O partial pressure was calculated to be 1.3 Pa based on a total vacuum chamber pressure of 13 Pa. This effect is quantitatively significant with granule radii less than 0.1 mm or at blanket porosities less than 30%, as discussed below.

The design characteristic of greatest impact on the tritium inventory is the granule size. A plot of tritium inventory versus granule radius is shown in Fig. 4-4. The figure shows that a minimum of 5 kg is obtained for 0.1 mm radius granules. For granules below 0.7 mm radius, the soluble contribution dominates the total tritium inventory, whereas the bulk diffusion contribution dominates for larger granules. The porous diffusion inventory decreases with increasing granule size due to the larger pores and

4-7
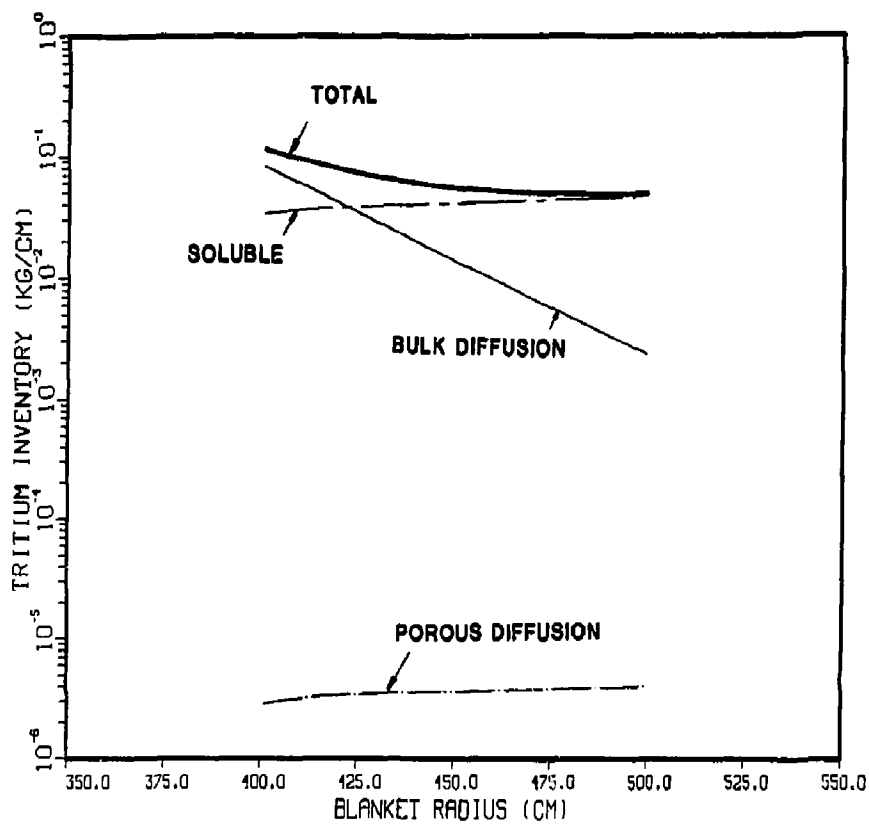
Fig. 4-3. Tritium inventory per centimeter of radial blanket thickness versus blanket radius.
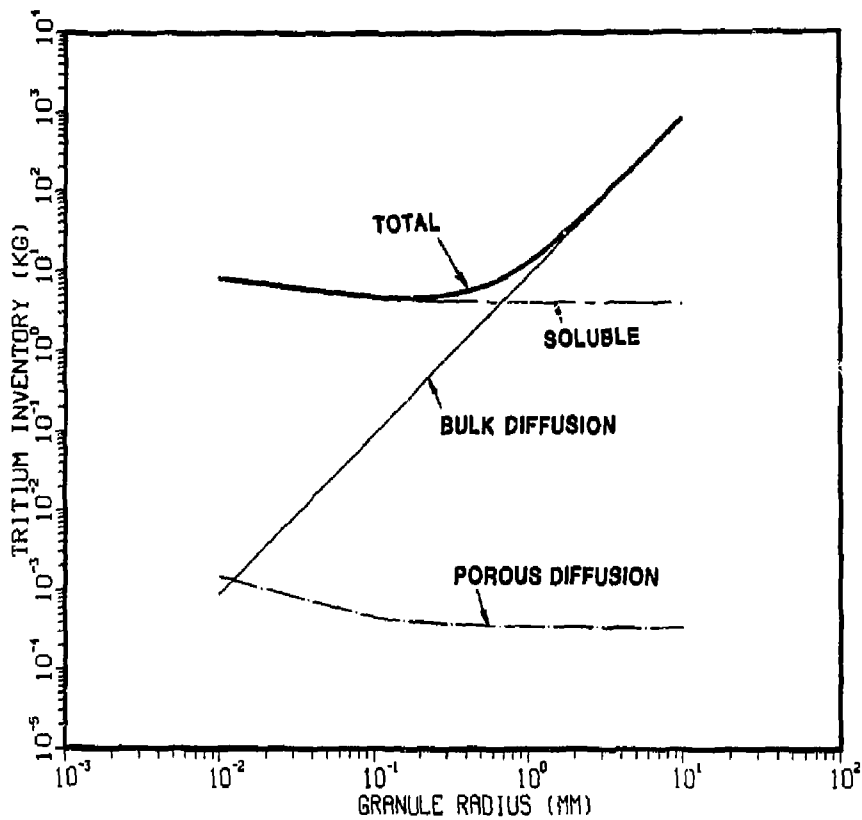
Fig. 4-4. Tritium inventory versus granule radius for a blanket with fully developed porous diffusion profile.

decreased path length for escaping from the blanket. Agitation of the bed during transport external to the chamber is expected to reduce inventories to those shown in Fig. 4-5. The major difference is in the soluble inventory for microspheres with radii less than 0.1 mm, reducing the minimum tritium inventory to 4 kg.

As mentioned above, the effect of the porous inventory on the soluble inventory is significant at blanket porosities less than 30%, as shown in Figs. 4-6 and 4-7. It is noted that such low porosities can only be achieved by combining granules of different sizes. affecting the flow characteristics of the Cascade blanket. For uniform granule sizes, variation in the blanket porosity from 0.4 to 0.6 results in less than a 10% change in the total inventory from the 50% porosity base case.

In the temperature range of 800 K to 1700 K, the total tritium inventory is fairly constant. as shown in Fig. 4-8. This is attributed to the opposing effects of temperature on the individual solubility and bulk diffusion contributions. As the temperature increases, the diffusion coefficient for tritium in Li_2O increased. decreasing the bulk inventory. However, the activity coefficient for LiOT in Li_2O decreases. increasing the soluble inventory. The opposing dependencies effectively cancel.

Finally, Fig. 4-9 shows that a ten-fold increase in the chamber T_2O partial pessure to 13 Pa would increase the tritium inventory to 16 kg. This effect is due to the change in the solubility inventory brought upon by the change in the porous inventory and indicates a relative insensitivity to the vacuum chamber T_2O partial pessure.

4.4. CONCLUSIONS

The reference Cascade reactor design would have a total tritium inventory of 6 kg. Although the selection of the optimum granule size requires considerations of fabrication cost and thermal stress analysis, granules of up to 1.5 mm radius would satisfy the current 10 g/MW(t) safety guidance on maximum tritium inventory (Ref. 4-10). The major portion of the tritium inventory in the total circulating Cascade
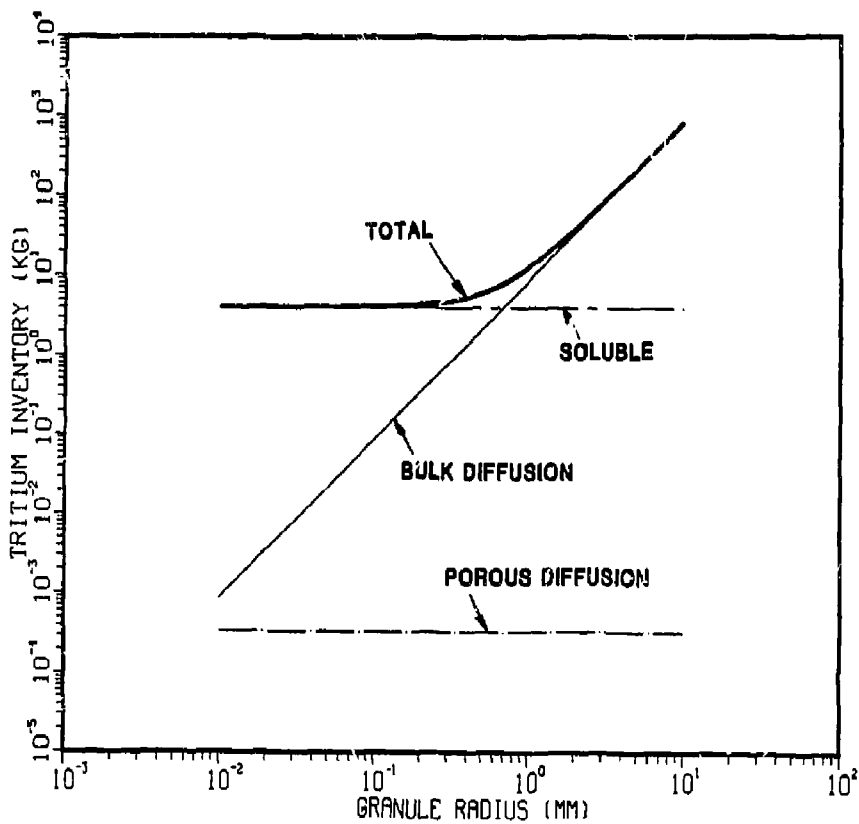
Fig. 4-5. *Tritium inventory versus granule radius for a blanket without a porous diffusion profile. Porous inventory due entirely to T_2O partial pressure within a vacuum chamber.*
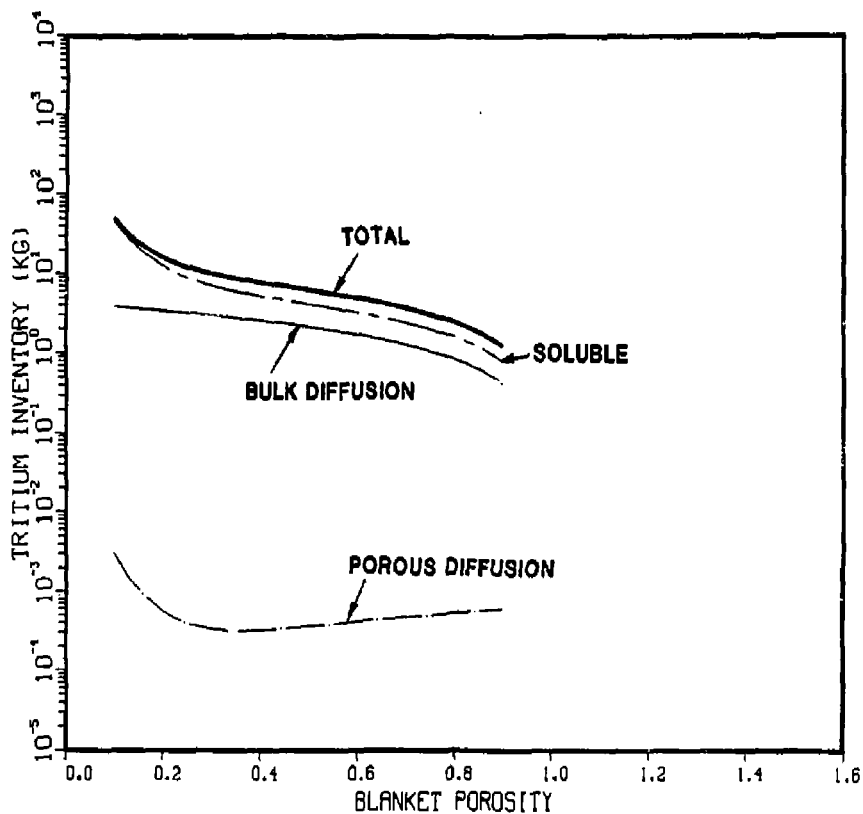
Fig. 4-6. Tritium inventory versus blanket porosity assuming fully developed porous diffusion profile.
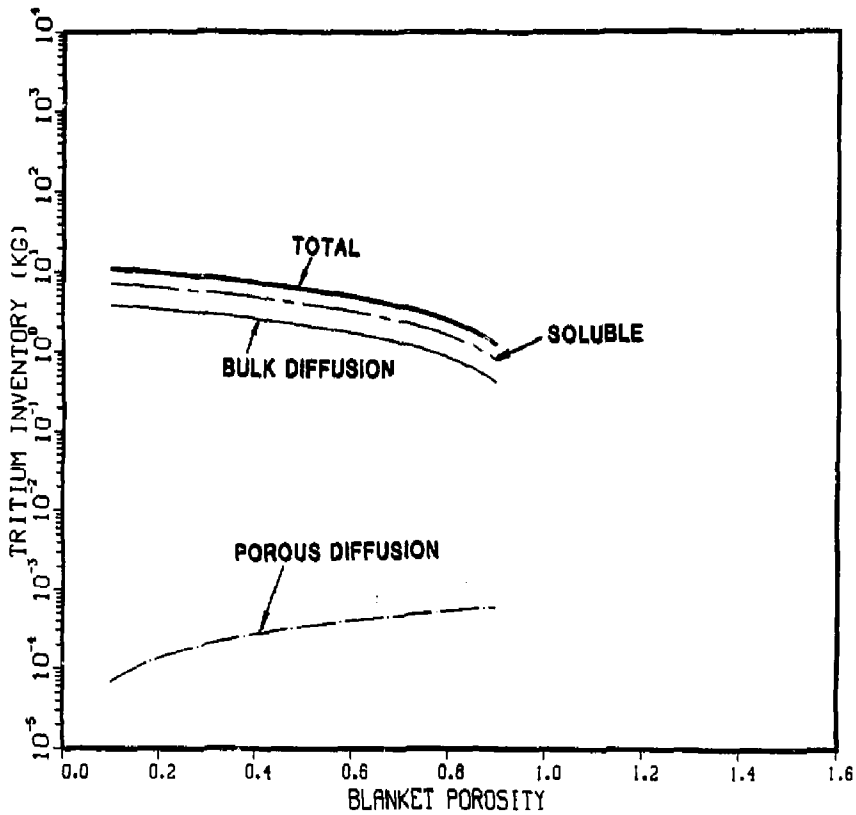
Fig. 4-7. *Tritium inventory versus blanket porosity assuming no porous diffusion profile. Porous inventory due entirely to T_2O partial pressure within the vacuum chamber.*
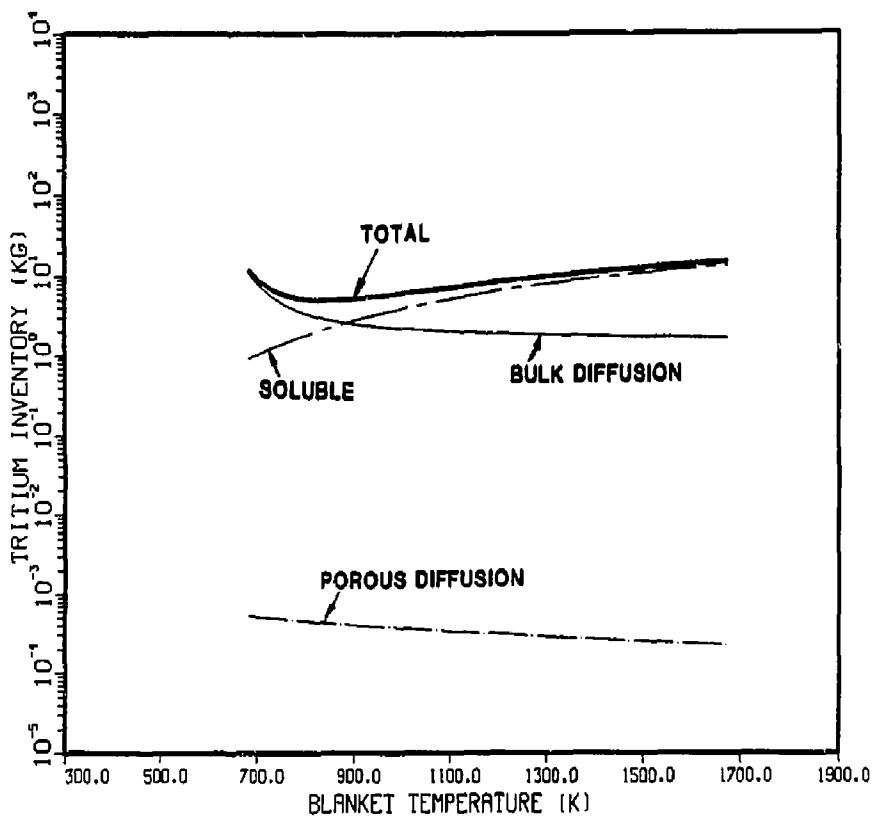
Fig. 4-8. Tritium inventory versus blanket temperature.
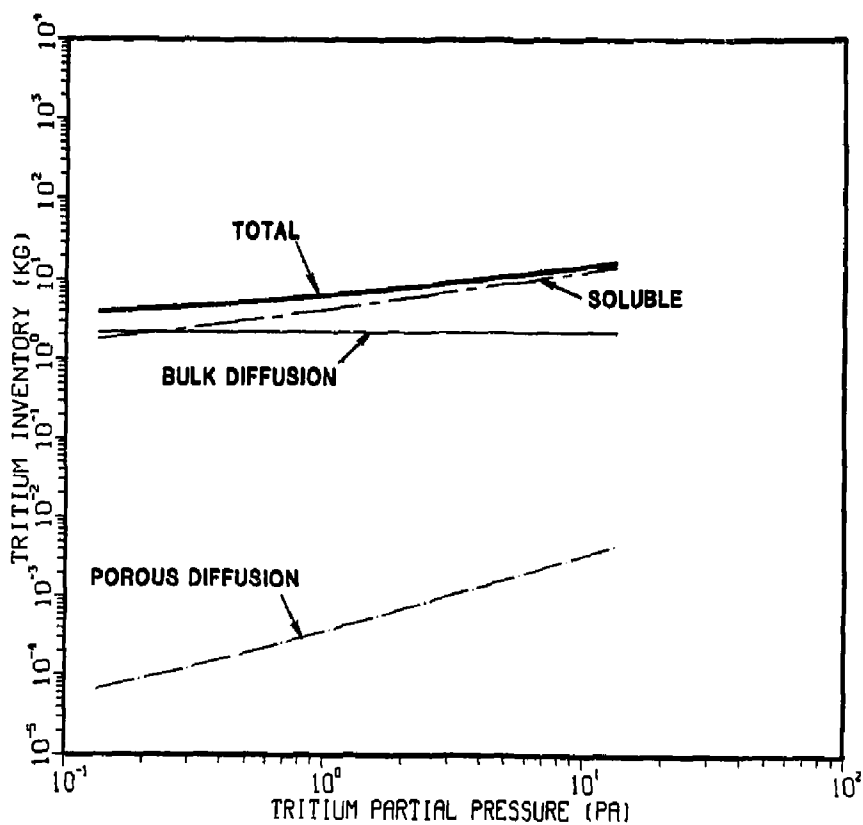
Fig. 4-9. Tritium inventory versus vacuum chamber T_2O partial pressure.

blanket, *i.e.*, all except for the porous diffusion contribution, is considered quite secure, having e-fold release times on the order of days or longer in the parameter range of present interest. Thus, instantaneous release is not mechanistically possible. These features of acceptable tritium inventory, low leakage, and simplicity of tritium recovery continue to preserve the safe, environmentally attractive and economical appeal of the Cascade approach to fusion power.

References for Chapter 4

4-1. J.J. Pitts, "Cascade: A Centrifugal-Action Breeder Reaction Chamber," *Nuclear Technology/Fusion.* Vol. 4, No. 2, Part 3, p. 967, September 1983.

4-2. K. Okuno and H. Kudo, "Thermal Release of Tritium Produced in Sintered Li_2O Pellets," *J. Nucl. Mater.* **116**, 1983, p. 82.

4-3. T. Tanifiyi *et al.*, "Tritium Release from Neutron-Irradiated Li_2O; Constant Rate Heating Measurements," *J. Nucl. Mater.* **95**, 1980, p. 108.

4-4. R.G. Clemmer *et al.*, "The TR10-01 Experiment: In-Situ Tritium Recovery Results," *Third Topical Meeting on Fusion Reactor Materials*, September 1983.

4-5. S. Nasu *et al.*, "A Preliminary In-Pile Test of Tritium Release from Li_2O Pellets," *J. Nucl. Mater.* **101**, 1981, p. 220.

4-6. C.E. Kessel, Jr., "TRIT3 Program Manual — A Fortran Code for the Prediction of Tritium Inventories and Permeation Rates at Steady-State in Solid Breeder Blankets for Fusion Reactors," GA Technologies Report to be published, 1984.

4-7. S. Nasu *et al.*, "Tritium Release from Neutron-Irradiated Li_2O Pellets," *J. Nucl. Mater.* **68**, 1977, p. 261.

4-8. J.R. Powell *et al.*, "Tritium Recovery from Fusion Blankets using Solid Breeder Compounds," Brookhaven National Laboratory Report BNL-20563, October 1975.

4-9. W. Meier of LLNL, Personal Communication to H.E. Levine of GA Technologies, June 1983.

4-10. M.A. Abdou *et al.*, "Blanket Comparison and Selection Study," Argonne National Laboratory Report ANL/FPP-83-1, Volume II, October 1983, pp. XI-8 through XI-13.

4-11. J.R. Hofmann, "Trasient Pressurization and Transport of a Two-Component Gas Within Interconnected Porosity of Solid Mixed-Oxide Fuel," *Nuclear Science and Engineering* 68, 1978, p.P73.

4-12. N.W. Gregory and R.H. Mohr, "The Equilibrium $2LiOH(s) = Li_2O + H_2O(g)$," *J. Am. Chem. Soc.*, Vol. 77, 1955, p. 2142.

4-13. J.H. Norman and G.R. Hightower, "Measurements of the Activity Coefficient of LiOH Dissolved in $Li_2O(s)$ for Evaluation of Li_2O as a Tritium Breeding Material," *Proceedings of the Third Topical Meeting on Fusion Reactor Materials*, Albuquerque, NM, October 1983.

1-5. D.P. Carosella, Jr., "Steam Generator Thermal Performance Model Verification by Use of Fort St. Vrain Nuclear Generating Station Test Data," ASME 79-WA/NE-1, December 1979.

5. PRIMARY HEAT EXCHANGER AND
TRANSPORT SYSTEM DESIGN

5.1. INTRODUCTION

The *primary coolant loop* of the Cascade reactor possesses some interesting characteristics. First, the circulating bed of Li_2O granules serves multiple functions as a heat generating, transport, and exchange medium. Second, it is not strictly a coolant loop since the circulating bed does not perform a cooling function, i.e., it does not remove appreciable quantities of heat from other components within the reaction chamber. Thus a loss of coolant accident has little meaning. Third, the Li_2O granules do not produce any radioactivity with significant decay afterheat. Thus, a loss of coolant accident would have insignificant consequences were one to occur. Finally, since the Li_2O granules are solid, they present unique challenges in both heat exchange to a working fluid or gas, and in their transport around the primary loop. These challenges are addressed in this chapter.

The heat exchangers used to recover the energy from the stream of solid Li_2O granules initially flowing in a vacuum are a key feature of the Cascade power conversion system. Several options appear possible and are presented in Section 5.2. Options presented include heat transfer in a helium medium as well as vacuu heat transfer. Since the Cascade reaction chamber must operate at vacuum conditions (~ 10 Pa), those heat exchangers that operate with a helium pressure on the Li_2O must be provided with vacuum locks. A possible lock system is described in Section 5.3. Section 5.4 presents the granule transport system options and the conceptual mechanical design integration of the components in the reactor primary coolant loop.

5.2. HEAT EXCHANGER DESIGN

5.2.1. Introduction

The transfer of heat from recirculating beds of solid particles has been employed industrially for many years in chemical process industries, in heat recovery systems and quite importantly, in catalytic reactors requiring continuous regeneration of the solid particle catalysts. The use of recirculating particulate solids as the primary heat energy transport medium in large-scale power conversion systems is relatively more unique. Conventional combustion systems typically depend on radiation and furnace gas sensible heat transport to the power conversion system and, in fission reactors, heat energy is transferred via the reactor core coolant fluid. A notable exception is contemporary work in fluid bed combustion power plant development in which certain versions opt for heat exchange surfaces immersed within the fluid bed combustion chamber.

Heat transfer models and correlations are available in the literature (Ref. 5-1) that can be applied with reasonable confidence for the case of a moving bed of lithium oxide flowing over heat exchanger surfaces under vacuum or with interstitial helium gas. Fluid bed heat transfer correlations are also available in the literature (Ref. 5-2) for immersed tube heat exchange surfaces. Various heat exchanger concepts for the Cascade power conversion system were evaluated using appropriate heat transfer models.

5.2.2. Li$_2$O Particle Bed Heat Transport Properties

Calculation of heat exchanger performance requires evaluation of the basic heat transport characteristics of the Li$_2$O particle bed. A review of the literature led to the recently published, multi-volume *Heat Exchanger Design Handbook* (Ref. 5-1) for stagnant and agitated bed heat transfer models of correlations. Li$_2$O bed

characteristics were evaluated over the range of 1173 K to 773 K, the ICF Cascade reactor discharge and return temperatures respectively.

5.2.2.1. Stagnant Li$_2$O Bed Thermal Conductivity

In packed beds, an exact mathematical model for heat transport is quite complex, even though accurate conductivity values for the solid and interstitial fluid are known. Building from earlier models by Hengst and Zehner, Bauer offers [Ref. 5-1(a). Section 2.8.1 the Zehner, Bauer model for calculation of stagnant bed conductivity λ_{so} [Ref. 5-1(a). eq. 7a]:

$$\frac{\lambda_{so}}{\lambda} = \left(1 - \sqrt{1 - \psi}\right) \left[\frac{\psi}{(\psi - 1) - \frac{\lambda}{\lambda_D}} - \psi\frac{\lambda_R}{\lambda} \right]$$

$$- \sqrt{1 - \psi} \left[\varphi \frac{\lambda_s^*}{\lambda} + (1 - \varphi) \frac{\lambda_{so}^*}{\lambda} \right] ,$$

where:

λ_{so} = effective stagnant bed thermal conductivity.

λ = interstitial gas thermal conductivity (Ref. 5-3).

ψ = bed porosity = 0.4 for mono-size granules.

λ_R = equivalent radiation thermal conductivity [Ref. 5-1(a). Eq. 11].

λ_s^* = mean thermal conductivity of solid phase [Ref. 5-1(a). Eq. 7b].

λ_D = equivalent thermal conductivity between the surfaces of the solid phase [Ref. 1(a). Eq. 13]

φ = describes the additional heat transfer through the solid path between adjacent particles [Ref. 5-1(a). Eq. 19].

Detailed expressions for each of the later four terms are provided in Ref. 5-1(a) as referenced above. Published experimental results are correlated with this model and are presented in Ref. 5-1(a) for various solid particle materials. gases, and particle sizes over a pressure range from 10^{-1} to 10^6 Pa.

Figure 5-1 plots the effective bed thermal conductivity calculated using the above model for the Li_2O particles in helium over a range of pressure from 10^{-5} to 1 MPa. Both 200 μm and 500 μm diameter particle sizes were evaluated. These curves are consistent with curves presented by Bauer [Ref. 5-1(a)] correlating the calculational model results with experimental data. The smaller particles typically cause the bed conductivity to be lower. because of the larger number of radiation and conduction interfaces through a unit thickness of bed.

5.2.2.2. Bed-To-Wall Heat Transfer Coefficient.

When heat is transferred from a packed bed of particles to a wall. a resistance appears that depends strongly on the transport properties of the gas phase. In addition. heat will be exchanged by radiation and contact area conduction.

According to Muchowski [Ref. 5-1(b). Section 2.8.3 . all of the transport phenomena mentioned above may be considered independent of one another. Therefore. the total heat transfer coefficient α_w at the wall is given by [Ref. 5-1(b). Eq. 1 :

$$\alpha_w = \alpha_g + \alpha_c + \alpha_r .$$

where subscript

$\quad\quad\quad\quad g$ = molecular gas conduction.

$\quad\quad\quad\quad c$ = contact area conduction.

$\quad\quad\quad\quad r$ = radiation.

For spherical particles. α_g can be calculated by Schlünder's formula Ref. 5-1(b). Eq. 3 :

$$\alpha_g = \frac{2\lambda_g}{R} \left[(K_n - 1)\ell n \left(1 - \frac{1}{K_n} \right) - 1 \right] .$$

where
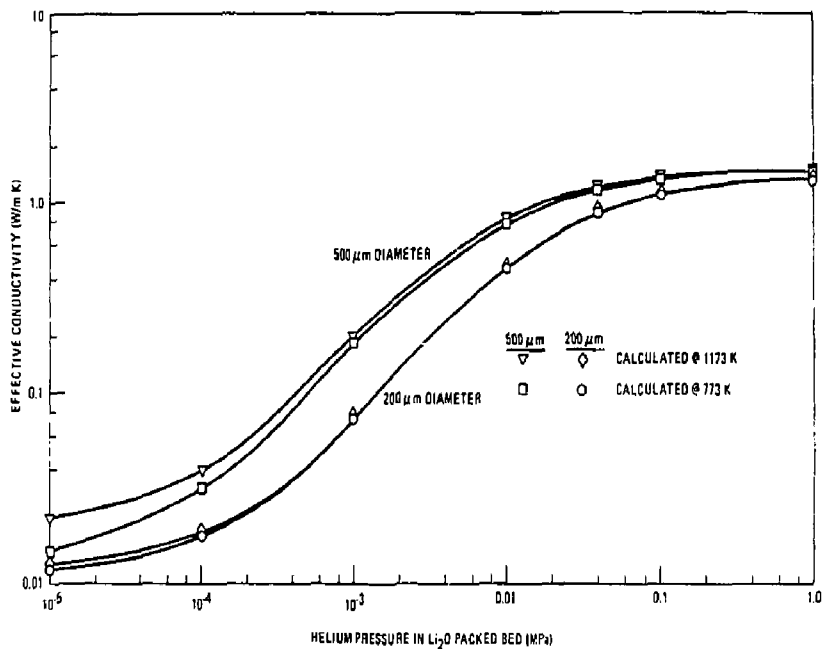
Fig. 5-1. Effective bed thermal conductivity of Li_2O granules in helium.

$$K_n = \frac{2\Lambda}{R} \left(\frac{2-\gamma}{\gamma}\right) = \text{Modified Knudsen number [Ref. 5-1(b), Eq. 4]}.$$

Λ = mean free path of the gas molecules [Ref. 5-1(b), Eq. 5],

R = particle radius

γ - accommodation coefficient [Ref. 5-4, Table 12 23]

λ_g = gas thermal conductivity (Ref. 5-3)

The mean free path Λ for a given gas is dependent upon both temperature and pressure; gas thermal conductivity λ is temperature dependent and the accommodation coefficient γ is a function of molecular weight and temperature.

The contribution of radiation from the bed to the wall can be expressed by a radiation heat transfer coefficient [Ref. 5-1(b), Eq. 6].

$$\alpha_R = 0.04 \, C_s \epsilon \left(\frac{T_m}{100}\right)^3.$$

where

C_s = 5.76 W/m² modified Stephan-Boltzman constant.

ϵ = absorption ratio (0.9 assumed).

T_m = mean temperature at the bed surface.

The contribution α_c of the contact area conduction to the wall heat transfer coefficient is strongly dependent on the material, geometry of the particles, and the structure of the particle surface. For poorly conducting (i.e., ceramic) granules, α_c is negligible according to Muchowski. This term was not included in the Li_2O bed-to-wall coefficient α_w for the ICF heat exchanger evaluation.

Figure 5-2 curves show the calculated bed-to-wall heat transfer coefficient for 200 and 500 μm diameter Li_2O granules in helium from 10^{-5} to 1 MPa. Below about
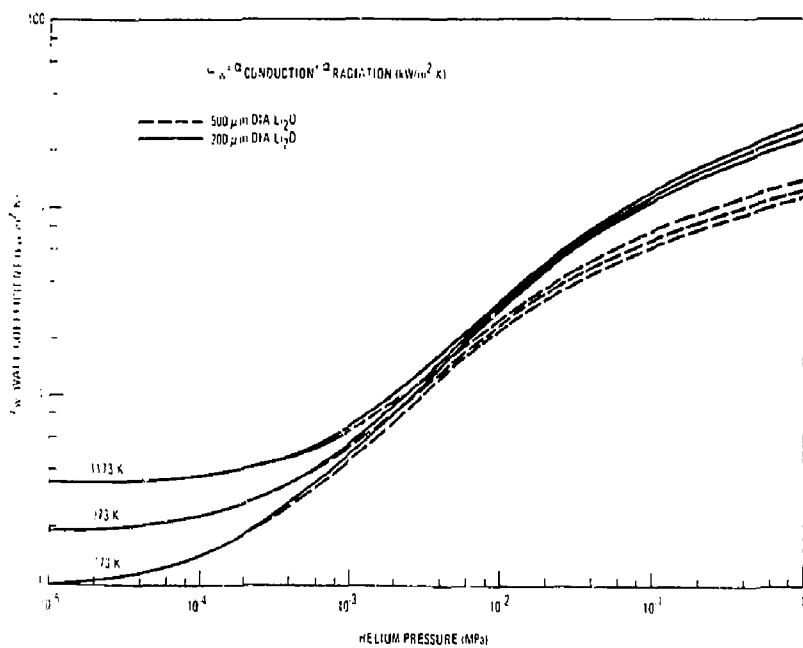
Fig. 5-2. *Packed bed-to-wall heat transfer coefficients for Li_2O granules in helium.*

5-7

10^{-3} MPa, particle size is unimportant as gas conduction heat transfer becomes negligible. Temperature level controls in this particle range with radiation being the primary heat transfer mechanism. At high pressure the smaller particles offer a smaller average gas gap thickness, thus permitting greater heat flow for a given temperature difference. The wall coefficient given by Ref. 5-1(b). Eq. 1 is an instantaneous value and defines the limiting overall heat transfer coefficient as time approaches zero for heat transfer from a stagnant packed bed.

5.2.2.3. Agitated Li$_2$O Bed-to-Wall Heat Transfer Coefficient

As pointed out above, the bed-to-wall heat transfer coefficient is an instantaneous value as time approaches zero for a stagnant packed bed. As particle contact time at the wall increases, the temperature gradient at the wall decreases due to the temperature gradient developing within the bulk bed behind the bed-wall interface. Periodic displacement and exchange of particles at the wall with particles from the bulk of the bed by agitation (or flowing movement) will maintain a steeper temperature gradient at the wall and thus improve heat transfer. A model for the effective bed-to-wall heat transfer coefficient $\bar{\alpha}$ as a function of average particle contact time at the wall and bed thermal properties is given by Muchowski [Ref. 5-1(b). Section 2.8.3, Eq. 16 :

$$\frac{\bar{\alpha}}{\alpha_w} = \frac{2}{\sqrt{\pi}Bi\sqrt{\overline{Fo_s}}}\left[1 - \frac{1}{\sqrt{\pi}Bi\sqrt{\overline{Fo_s}}}\,\ell n\left(1 - Bi\sqrt{\overline{Fo_s}}\right)\right] \ .$$

where

$$Bi = \frac{\alpha_w s}{\gamma_{so}} = \text{Biot number. [Ref. 5 - 1(b) Eq. 17]}$$

$$Fo_s = \frac{K_{app}t_s}{s^2} = \text{Fourier number. [Ref. 5 - 1(b). Eq. 18]}$$

$$K_{app} = \frac{\gamma_{so}}{\rho_B C p_s} = \text{Apparent thermal diffusivity of the packed bed.}$$
$$\text{(Ref. 5 - 5. Eq. 3 - 2)}$$

$s = $ bed depth, cm

$\lambda_{so} = $ stagnant bed effective thermal conductivity (Fig. 5–1)

$\alpha_w = $ packed bed–to–wall heat transfer coefficient (Fig. 5–2)

$t_s = $ particle–wall contact time, sec.

$\rho_B = $ bulk particle bed density @ 0.6 solids fraction and
   90% $Li_2O = 1.09\,g/cm^3$

$Cp_s = Li_2O$ solid specific heat = $2.78\,J/g$ (Ref. 5–6).

According to Muchowski, the above expression is valid for $Fo < 0.1$. As t_s decreases to where α/α_w becomes >1.0, then $\alpha = \alpha_w$ for any lesser value of t_s, α_w being the upper limit of heat transfer from the bed to the wall.

The above expression for $\bar{\alpha}$ was evaluated over a range of contact times from 0.3 to 10 seconds using bed thermal properties for 200 μm particles with helium pressure of 10^{-1} MPa. α_w is higher for 200 μm diameter Li_2O particles at higher helium coupling gas pressure. For vacuum conditions, the wall coefficient α_w is the same for either 200 or 500 μm diameter particles, but the bed conductivity γ_{so} is higher for 500 μm diameter Li_2O particles. Therefore, the effective wall heat transfer coefficient $\bar{\alpha}$ under vacuum conditions was evaluated for 500 μm diameter particles. The results are plotted on Fig. 5-3.

Comparisons shown by Muchowski [Ref. 5-1(b)] for calculated ideal stirred (agitated) bed heat transfer coefficients versus experimental data suggest that the calculated values may be optimistic. Considering the complexity of accurately modeling heat transfer from a flowing particle bed, it is clear that detailed experimental heat transfer measurements will be required for flowing Li_2O particles in helium before heat exchanger design can proceed much beyond a conceptual study phase.
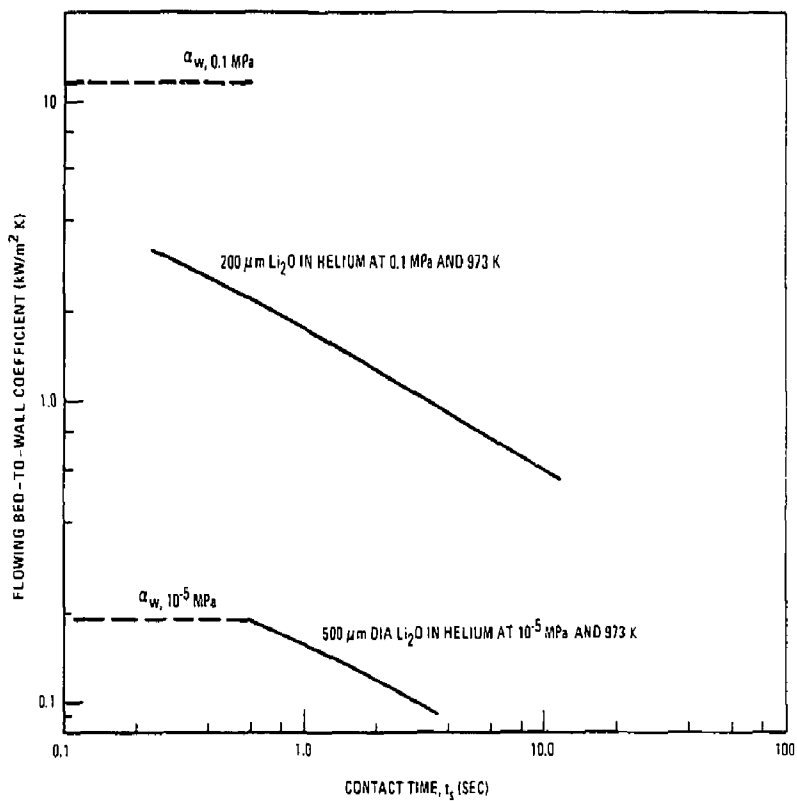
Fig. 5-3. Agitated Li_2O granule-to-wall heat transfer coefficient.

5.2.2.4. Fluid Bed Heat Transfer Coefficient

Gas-fluidized systems are characterized by the vigorous mixing generated within the bulk of the bed, caused by the rising gas bubbles. In this condition, the volume rate of bubbles approximately equals that of the gas flow in excess of that required to bring the bed to a barely fluidized condition (*i.e.*, minimum fluidization velocity u_{mf}) [Botherill. Ref. 5-1(c)].

Because of the very large area of particle surface exposed within a fluidized bed, fluid-to-particle heat transfer is rarely a limiting factor [Ref. 5-1(c)] even though at any instant, gas-solid contact is far from uniform throughout the bed. The very wide range of possible bed behavior causes some problems in the design of fluid bed systems in that fluidization behavior of small beds can be very different from that of large beds, so that small scale tests are often quite misleading. This comes about because bubbles are constrained in size by the size of the equipment involved. Large bubbles rise correspondingly faster through the bed than smaller ones. Immersion of heat transfer surfaces within the bed also affects the bubbling behavior and can have different effects according to operating circumstances. Although published correlations are considered adequate for concept scoping studies, it is clear that large scale fluid bed heat transfer tests would be required to establish detailed fluid bed heat exchanger parameters.

Review of the literature for immersed surface fluid bed heat transfer coefficient correlations led to selection of the correlation for horizontal immersed tubes developed by Vreedenberg and presented as Eq. 9-13 by Kunii and Levenspiel (Ref. 5-8, Eq. 9-13).

$$\frac{h_w d_{ti}}{k_g} = 0.66 \left(\frac{C_{pg}\mu}{k_g} \right)^{0.3} \cdot \left[\left(\frac{d_{ti}\rho_g u_0}{\mu} \right) \left(\frac{\rho_s}{\rho_g} \right) \left(\frac{1-\epsilon_f}{\epsilon_f} \right) \right]^{0.44} .$$

for

$$\frac{d_{ti}\rho_g\mu_0}{\mu} < 2000 \, ,$$

where:

C_{pg} = 20.7 J/K mole. specific heat of helium gas at constant pressure (Ref. 5-4, Table 3-173)

μ = 3.953 · 10^{-6} T$^{0.687}$ g/cm s helium gas viscosity (Ref. 5-7)

k_g = 2.774 · 10^5 T$^{0.701}$ W/cm K helium gas thermal conductivity (Ref. 5-7)

ρ_g = helium density, g/cm^3

d_{ti} = immersed tube diameter. cm

ρ_s = 1.81 g/cm^3 Li$_2$O particle density @ 90% dense (Ref. 5-8)

e_f = 0.70 void fraction in fluidized bed assuming bed expansion height of 2 times minimum fluidization

u_0 = helium fluidizaion flow velocity. cm/s

h_w = surface heat transfer coefficient to horizontal immersed tubes. W/cm^2 K

Vreedenberg's correlation shows improved heat transfer rate as u_0 increases and as immersed tube size d_{ti} decreases. Particle size enters in only that u_{mf} (minimum fluidization velocity) and u_t (terminal velocity) are higher for larger particles. This suggests that an advantage exists by using larger particles in the fluid bed. Arguments presented by Botterill [Ref. 5-1(c). Fig. 1] however indicate a decreasing surface heat transfer rate in a fluid bed as particle size increases over the range of 100 to 1000 μm. On the other hand. Botterill further states that as particle size increases. the maximum surface heat transfer coefficient occurs nearer to the minimum fluidization velocity. Fundamentally, particle-to-wall contact time must be minimized (mixing rate within the bulk bed maximized) to achieve higher heat transfer rates but. bubble blanketing of the surface increases as gas flow rate increases. thereby decreasing particle contact density at the wall. This optimization process clearly requires

experimental data for the specific geometry and bed materials of interest. Within the limited scope of this study, evaluation of the immersed-tube fluid bed heat exchanger was confined to 200 μm diameter particles with $u_0 = 40\,u_{mf}$. Results in this case are not greatly different than for 500 μm diameter particles with $u_0 = 10\,u_{mf}$.

As a first order check of the Vreedenberg correlation, the value for h_w was determined using a uniform surface renewal model by Mickley (Ref. 5-2, Eq. 46) for 200 μm diameter Li_2O particles. Also, experimental results plotted by Botterill (Ref. 5-2, Fig. 15) were used to estimate h_w assuming a 20 ms surface contact time. Both of these estimates for h_w were (perhaps fortuitously) within 10% of the value of 1330 W/m^2 K calculated using Vreedenberg's correlation with 200 μm diameter Li_2O at $u = 40\,u_{mf}$ and 4 cm diameter immersed tubes.

5.2.3. Heat Exchanger Concept Evaluation

5.2.3.1. Heat Exchanger Tubes and Steam-Side Correlations

The thermal and energy transport parameters used for the heat exchanger design evaluations are listed in Table 5-1. Steam conditions were selected to utilize a conventional, superheated steam turbine cycle comparable to modern fossil fired power plants.

Double walled heat exchanger tubes are employed for all heat exchanger concepts involving heat transfer from the flowing Li_2O particles through heat exchanger tubes to water/steam working fluid. The double wall tubes provide a barrier to tritium diffusion into the steam system and also reduce the likelihood of water leaks into the Li_2O granule blanket. Two sizes of double wall heat exchanger tubes were conceptually defined, 2.5 and 4.0 cm outside diameter. Characteristics of the tubes are summarized in Table 5-2.

Using the steam-side parameters from Table 5-1, available heat transfer temperature differences between the Li_2O and steam-side flows were determined on the basis

TABLE 5-1
CASCADE POWER CONVERSION SYSTEM
Heat Transfer System Parameters

Thermal Rating	3000 MW
Primary Side	
Li_2O Granule Flow Rate	2700 kg/s
Li_2O Granule Volume Rate	2.48 m^3/s
Li_2O Granule Diameter	200 μm OR 500 μm
Li_2O Temperature – to HX	1173 K
Return	773 K
Helium Fluidization/Thermal Coupling Gas	
Secondary Side	
Steam Pressure	15.1 MPa
Feedwater Flow Rate	1180 kg/s
Feedwater Temperature	473 K
Enthalpy	878 J/g
Superheated Steam Temperature	813 K
Enthalpy	3421 J/g
Evaporator Enthalpy Rise	1730 J/g
Superheater Enthalpy Rise	813 J/g

of once-through boiling and superheat in counterflow with the Li_2O. Although not completely accurate because of feedwater inlet subcooling. water/steam temperature was conservatively assumed constant through the evaporator section, then increased linearly through the superheater section. Also in staged fluid-bed heat exchanger concepts. the Li_2O temperature in each stage is uniform. thus step-wise temperature decreases are experienced rather than a linear decrease relative to the counterflowing steam-side flow. Within the scope of this concept study, the somewhat idealized temperature profiles shown by Fig. 5-4 were used for all of the once-through Li_2O to steam boiler concepts.

TABLE 5-2
CASCADE POWER CONVERSION SYSTEM
Double Wall Steam Boiler Tube Characteristics

Outside Diameter (cm)	2.5	4.0
Pitch (cm)	3.25	5.0
Outside Surface Area (m^2/m_ℓ)	0.0785	0.126
Inside Surface Area (m^2/n_i)	0.0427	0.0735
Inside Flow Area (cm^2)	1.45	4.3
Interspace Gap Width (μm)	200	300
Overall Conductance $(W/m^2$-K) (referred to Outside Surface Area)	700	484
Maximum Tensile Stress (MN/m^2) at 15.1 MPa Internal Pressure	38	44

The log mean temperature difference for the boiler section is given by:

$$\Delta T_{MB} = \frac{\Delta T_2 - \Delta T_1}{\ell n \frac{\Delta T_2}{\Delta T_1}} = \frac{432 - 160}{\ell n \frac{432}{160}} = 274 \text{ K} .$$

For the superheater section:

$$\Delta T_{ms} = \frac{360 - 432}{\ell n \frac{360}{432}} = 395 \text{ K} .$$

In the evaporator section, a water-side surface heat transfer coefficient of 57×10^3 $W/m^2 K$ was used. This value was taken to be the same as used for the Fort St. Vrain (FSV) Nuclear Generating Station steam generator design based on similar once-through boiling conditions of temperature, pressure, and mass velocities (Ref. 5-9).

For the superheater section, the Bishop correlation as used for the FSV steam generators (Ref. 5-9, Eq. 11) is used.
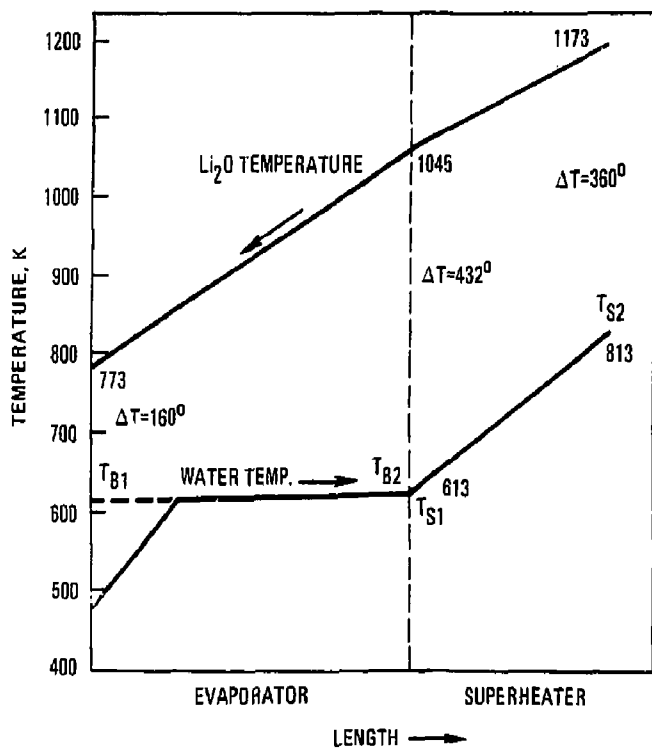
Fig. 5-4. Li_2O and steam boiler temperature profiles.

$$h_{sw} = 0.0073 \left(\frac{k}{d_i}\right) (N_{Re})^{0.886} (Pr)^{0.61} ,$$

where:

h_{sw} = superheater steam-side heat transfer coefficient, $W/cm^2 K$,

k_v = 5.3×10^{-4} W/cm K, steam vapor thermal conductivity
(Ref. 5-4, Table 3-264)

d_i = tube inside diameter, cm

N_{Re} = Reynolds number = $(u_v d_i \rho_v)/(\mu_v)$

where

u_v = steam velocity, cm/s

ρ_v = steam density, g/cm^3 (Ref. 5-50, steam tables)

μ_v = 0.6×10^{-3} g/s cm @ 700 K, 14 MPa
(Ref. 5-4, Table 3-264) steam viscosity

Pr = Prandtl number = $(c_p \mu_v)/k_v$,

c_p = 3.1 J/g K, @ 700 K steam vapor heat capacity
(Ref. 5-4, Table 3-261).

The calculated value of h_{sw} is typically about 5000 W/m^2 K for the heat ex-
changers evaluated in this study.

5.2.3.2. Fluid-Bed Immersed-Tube Exchanger

Fluid-bed heat exchangers with immersed tubes offer relatively high bed-to-
surface heat transfer coefficients, very good bed mixing and fluid-like solids transport
capabilities. On the negative side, tube abrasion, vibration, and solids dusting can
be troublesome for long term power plant operations.

To minimize the Li_2O transport height differences for the ICF power conver-
sion system, a horizontally staged counterflow, once-through, immersed tube fluid-
bed heat exchanger concept is evaluated. The concept is shown by Fig. 5-5. In this
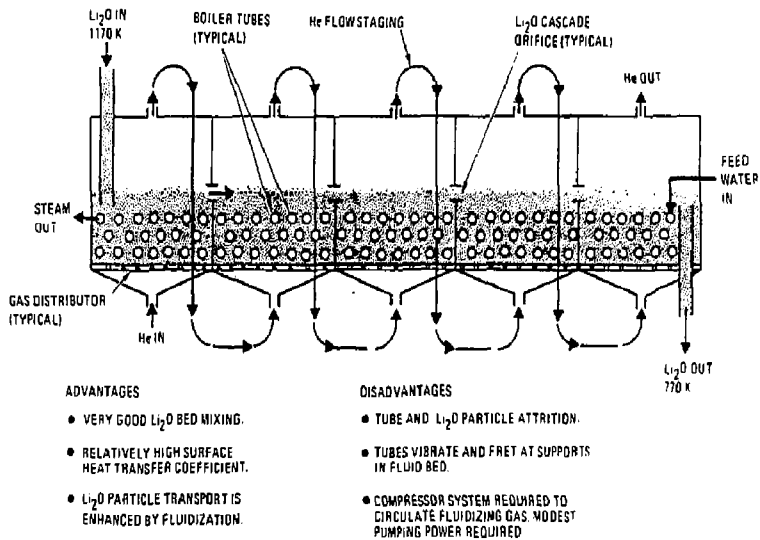
Fig. 5-5. Immersed-tube, fluid-bed, staged counterflow heat exchanger.

design, the high temperature Li_2O enters the first stage where it mixes with the stage Li_2O inventory that is fluidized around the immersed tubes stacked in a triangular array. Triangular pitch spacing of the tubes is 3.25 and 5.0 cm for the 2.5 and 4.0 cm diameter tubes, respectively. With the close triangular spacing used to minimize bubble growth in the bed while minimizing Li_2O inventory volume within each stage, adequate space is not available for return bends on the multi-pass tubes. The most direct way to provide this space is by installing dummy tubes in alternate layers. This is, however, an added cost and complexity. Further, more detailed work on this concept should include mechanical layout studies of the tube array to determine whether a close packed array can be achieved without dummy tubes.

For once-through boiling and superheat, the required tube length is determined by the feedwater flow rate per tube, the enthalpy rise required, and the overall thermal conductance from the Li_2O bed to the water/steam:

$$L = \frac{\dot{m}\,\Delta h}{u_0\,\Delta T_m} \quad \text{(m)}\,.$$

where:

Δh = enthalpy rise, J/g,

$\dot{m}$ = feed water flow rate per tube, g/s,

u_0 = overall conductance, W/m_ℓ K (based on outside surface area of tube per meter of length).

ΔT_m = log mean temperature difference, K (Fig. 5-4).

Since u_0 is different for the evaporator and superheat sections because of the steam-side film coefficient, it is necessary to calculate each length separately and add them for total once-through tube length.

$$\Sigma L_t = L_e + L_s \quad \text{(m)}\,.$$

5-19

The enthalpy rise for each section is specified in Table 5-1. Assuming six stages of approximately equal Δh per stage results in four evaporator stages and two superheat stages. Tube length per stage is then

$$L_{ts} = \frac{\Sigma L_t}{6} \qquad \text{(m)} ,$$

and assuming two passes per stage for each tube. the stage width w_s (perpendicular to the plane of the paper) becomes

$$w_s = \frac{L_{ts}}{2} \qquad \text{(m)} ,$$

for a bed array of twenty active tubes depth. the total array frontal length per stage is

$$\mathcal{L}_A = \frac{N_t \left(P_t\right) \times 10^{-2}}{10^\cdot} \qquad \text{(m)} ,$$

where

  $\mathcal{L}_A$ = horizontal length normal to the tubes of the stage, m

  N_T = number of once-through tubes, calculated from 1800 kg/s (total feedwater flow rate from Table 5-1) divided by the feedwater flow rate per tube $(\dot{m})$

  P_T = horizontal tube pitch spacing, cm

    *Note that for 20 active tubes depth and 2 passes per tube there are 10 active tubes per unit horizontal pitch.

Frontal area per stage is then

$$A_{FS} = \mathcal{L}_A w_s \qquad \text{(m}^2\text{)} .$$

Since the stages are cascaded in series, the frontal area. A_{He} for helium fluidization flow is

5-20

$$A_{He} = \frac{w_s N_T (P_l - d_{lo}) \times 10^{-2}}{10} \qquad (\text{m}^2) \, ,$$

where d_{lo} = outside tube diameter, cm.

Fluid bed depth, H_B for 20 active tubes array depth with alternate dummy tubes and allowing two tube diameters between the bottom of the array and the gas distributor and three tube diameters of bed depth above the tube array is

$$H_B = 20 + (20 - 1) \, (\rho_t \cos 30^\circ - 5 \, d_{t0}) \times 10^{-2} \qquad (\text{m})$$

Fluidization pressure drops per stage can be estimated as equal to the static head of Li_2O

$$\Delta P_B = H_B \rho_B g \, .$$

where

$$
\begin{aligned}
\rho_B &= \rho_s (1 - e_f), \\
e_f &= 0.7 \text{ for the expanded bed,} \\
\rho_s &= 1.81 \text{ g/cm}^3 \ (90\% \text{ dense } Li_2O) \\
g &= 980 \text{ cm/s}^3 \text{ gravity constant.}
\end{aligned}
$$

For fluidization pumping power estimates, the bed fluidization pressure drop was doubled to account for ducting and gas distributor losses. Compressor work, W_c for isotropic compression at 0.85 compressor efficiency and six fluid bed stages is given by (Ref. 5-4, Eq. 6-22)

$$0.85 \, W_c = \frac{k}{k - 1} \, (RT_1) \left[\left(\frac{P_2}{P_1} \right)^{(k-1)/k} - 1 \right] \, .$$

where

W_c = compressor work per kg helium flow, N−m/kg,

k = 1.66 for helium (Ref. 5-4, Table 3-180),

R = 2.08 × 10^3 N−m/kg K,

T_1 = initial temperature, K,

P_1 = initial pressure, N/m²,

$P_2 = [P_1 + 6(2)\Delta P_B]$ final pressure, N/m².

Fluidization helium flow rate for 40 u_{mf} from Section 5.2.2.4 is given by

$$\dot{M} = 40\, u_{mf} A_{He} \rho_{He} \, ,$$

where for spherical particles (Ref. 5-2, Eq. 3-17)

$$u_{mf} = \frac{d_p^2 (\rho_s - \rho_g) g}{150\,\mu} \left(\frac{e_{mf}^3}{1 - e_{mf}} \right) \, ,$$

d_p = particle diameter, cm

g = 980 cm/s² gravitational constant,

e_{mf} = 0.4 bed void fraction at minimum fluidization.

For 200 μm diameter Li₂O,

$$u_{mf} = \frac{(0.2)^2 (1.81 - 5 \times 10^{-5})(980)}{150(4.46 \times 10^{-4}} \left(\frac{0.4^3}{1 - 0.4} \right) = 1.13\,\text{cm/s} \, .$$

Table 5-3 lists the major characteristics of immersed-tube fluid-bed heat exchangers evaluated using ICF power conversion system parameters. Both 2.5 and 4.0 cm diameter tubes were evaluated. As noted earlier, 200 μm diameter Li₂O particles were used as a basis for the fluid bed calculations. Designs employing either tube size

TABLE 5-3

CASCADE POWER CONVERSION SYSTEM

Immersed-Tube, Fluid-Bed, Staged-Counterflow,
Once-Through Boiler Concept

- Li_2O Granules Fluidized in Helium Gas
- Double Wall Boiler Tubes
- Steam Rate 4.2×10^6 kg/hr @ 15.1 MPa, 810 K

Tube Diameter (cm)	2.5	4.0
Li_2O-to-Tube Heat Transfer Coefficient (W/m^2 K)	1730	1330
Number of Tubes	6200	2100
Tube Length (m)	46	110
Surface Area (m^2)	22,000	29,000
Frontal Area (per stage) (m^2)	85	96
Helium Fluid-Bed Flow Area (per stage) (m^2)	24	19
Number of Stages	6	6
Tube Array Height (m)	1.3	1.9
Fluidization Helium Pressure Drop (MPa)	0.17	0.24
Fluidizing Helium Pumping Power (MW)	1.6	1.3

appear practical, the most significant difference being the number of tubes a factor of three less but more than twice as long for the 4 cm diameter tubes.

5.2.3.3. Fluid-Bed Direct Contact Heat Exchanger

The high effective surface area of a fluid-bed direct contactor is ideal for the transfer of heat from particulate solid to a fluid. However, in the case of solid-to-gas exchange, the large disadvantage in heat capacity of the gas requires high pressure and large frontal area to keep gas velocity sufficiently below terminal velocity of the particles to maintain a stable fluidized bed. In this case, larger particles are preferred.

A staged counterflow contact heat exchanger is shown conceptually in Fig. 5-6. In this vertical configuration, the Li_2O particles flow by gravity head from stage to stage against the fluidization pressure gradient. A horizontal configuration may also be possible, but to achieve a countercurrent flow, some means to move the Li_2O

1170 K
Li₂O
IN

~1130 K
HOT H₈
OUT

CYCLONE SEPARATOR

Li₂O
COME–DOWN
TUBES

Li₂O
RECOVERY

ADVANTAGES

- HIGH EFFECTIVE SURFACE AREA
  PROVIDES GAS–SOLIDS NEAR THERMAL
  EQUILIBRIUM AT SOLIDS INLET TEMPERATURE

- BOILER OR SECONDARY HEAT EXCHANGER
  CAN BE CONVENTIONAL SINGLE WALL TUBES

- CAN COUPLE DIRECTLY TO CCGT

GRID PLATES

DISADVANTAGES

- HIGH PRESSURE REQUIRED TO PROVIDE
  ADEQUATE HEAT CAPACITY. GAS FLOW
  RATE LIMITED BY FLUIDIZATION VELOCITY.

730 K COOL
He IN

- Li₂O PARTICLE ATTRITION.

- POTENTIAL Li₂O DUST AND LiOT CARRYOVER.

- HIGH PUMPING POWER FOR GAS RECIRCULATION.

Li₂O
OUT
770 K

Fig. 5-6. Direct contact, fluid-bed counterflow heat exchanger.

5-24

particles horizontally against the pressure gradient between stages must be devised. The scope of this study did not permit exploration of means to accomplish this.

In the case of the immersed-tube concept discussed above (Section 5.2.3.2), the fluidizing gas is directed in parallel with the Li_2O, thereby allowing use of the stage-to-stage pressure difference to convey the particles horizontally. The small heat capacity and flow rate of the low pressure helium fluidization flow does not significantly degrade thermal performance. In the direct contact heat exchanger, the high pressure, high flowrate helium must flow countercurrent to the Li_2O to effectively utilize the high Li_2O outlet temperature. Hot helium leaving a fluid-bed contactor can be used for either a helium heated steam boiler or a closed-cycle gas turbine. At 1100 K and above a helium gas turbine cycle is practical and is discussed in Section 5.5 below.

Parameters of the fluid bed contactor and helium-to-steam boiler are tabulated on Table 5-4. In this case, 500 μm particles were selected to maximize the allowable helium flow velocity, thus reducing frontal bed area required. Helium flowrate required to transfer the required heat energy is

$$\dot{m}_{He} = \frac{Q}{C_p \Delta T N_s} ,$$

where

Q = 3×10^9 J/s, ICF heat generation rate,

C_p = 5.23 J/g K, specific heat of helium (Ref. 5-4, Table 3-173)

ΔT = helium temperature rise, °C,

N_s = 10, number of stages.

Assuming the 10 contact stages have equal energy transfer, then ΔT_{Li_2O} per stage is 40 K. Since fluid bed mixing is very rapid, each stage will be equilibrated at stage exit helium and Li_2O temperature. Therefore with 10 stages, contactor exit helium temperature will be 1130 K. Helium flowrate required is:

TABLE 5-4
CASCADE POWER CONVERSION SYSTEM
Intermediate Fluid-Bed, Direct Contact Heat Exchanger
To Helium Once-Through Steam Generator

- Li_2O Rate 2700 kg/sec @ 1170 K, 500 μm Diameter Granules
- Li_2O to Helium Fluid-Bed contacter with Staged Counterflow
- Steam Rate 4.2×10^6 kg/hr @ 15.1 MPa and 810 K
- Helium to Steam Helical Bundle Once Through Steam Generator

Fluid-Bed Contactor Helium Pressure	5.1 MPa
Superficial Fluidization Velocity	280 cm/sec (40 U_{mf})
Number of Countercurrent Stages	10
Total Frontal Area per Stage	20 m^2
Number of Contacter Modules	10
Module Diameter	5 m
Module Height	13 m
Helium Flow Rate	1430 kg/sec
Helium-to-Steam Generator Surface Area	8300 m^2
Number of Steam Generator Modules	6
Heat Transfer Loop Helium Pumping Power	44 MW

$$\dot{m}_{He} = \frac{3 \times 10^9 \text{ J/s}}{10(5.23 \text{ J/g K}) 400 \text{ K}} \doteq 1430 \text{ kg/s} .$$

Minimum fluidization velocity for 500 μm diameter Li_2O is $u_{mf} = 7.06$ cm/s (Ref. 5-2, Eq. 3-17). At 40 $u_{mf} = 2.82$ m/s, and 5.1 MPa pressure, with average helium density of 5.2 kg/m^3, bed frontal area is

$$\Sigma A_{FB} = \frac{1430 \text{ kg/s}}{2.5 \text{ kg/m}^3 (2.82 \text{ m/s})} \doteq 203 \text{ m}^2 .$$

Therefore with 10 contactor modules of 10 stages each, the frontal bed area per module is about 20 m^2. Average stage residence time for the Li_2O particles is 25 seconds.

Assuming an average unexpanded stage bed depth of 30 cm, the module fluidization ΔP is

$$\Delta P_{FB} = 10\,\text{stages}\,(0.3\,\text{m})\,1.8\times10^3\,\text{kg}/\text{m}^3\,(0.6\,\text{solid fraction})\,(9.80\,\text{m}/\text{s}^3)$$
$$= 3.2\times10^4\,\text{Pa}\,,$$

multiplying by 2 for gas, distributor, and miscellaneous losses, the module pressure loss becomes

$$\Delta P_m = 6.4\times10^4\,\text{Pa}\,,$$

The helium-to-steam boiler is sized based on FSV nuclear generating station conditions (Ref. 5-11). The FSV employs 12 helical-tube steam generator modules heated by helium gas at 4.8 MPa entering the superheater in counterflow at 1010 K. Total surface area is 3712 m^2 for 730 MW thermal rating (excludes reheat section). Feed water flow rate is 290 kg/s. Using the FSV helium and steam temperature and flow conditions, an overall helium-to-steam conductance of 1253 W/m^2 K is calculated for the steam generator modules.

Using the FSV overall conductance value and ICF power conversion system parameters:

Helium inlet to steam generator = 1130 K

Helium outlet from steam generator = 730 K

Helium flow rate = 1430 kg/s

Feed water flow rate = 1.8 × 10^3 kg/s

Feed water enthalpy = 878 J/g @ 470 K

Superheated vapor enthalpy = 3421 J/g @ 810 K

$$\text{Overall } \Delta T_m = \frac{(1130 - 810) - (730 - 470)}{\ell n\,\frac{320}{260}} = 289\,\text{K}$$

$$Q = 3 \times 10^9 \, \text{J/s}$$

$$A_{HX} = \frac{3 \times 10^9 \, \text{W}}{1253 \, \text{W/m}^2 \, \text{K}} = 8300 \, \text{m}^2 \, \text{heat exchanger surface area.}$$

From Ref. 5-11, the helium-side module ΔP is 2.5×10^4 Pa. Assuming a compressor efficiency of 0.85 with a total helium side $\Delta P = (6.4 + 2.5) \times 10^4$ Pa, required compression power is calculated to be 44 MW (Ref. 5-4 Eq. 6-22).

These results confirm the feasibility of the direct contact fluid bed heat exchanger with a helium-to-steam boiler. For a closed-cycle gas turbine, the contact fluid bed is likely the best option since a close approach temperature is required to the chamber outlet Li_2O temperature. For tube-type exchangers, surface area requirement becomes very large as the approach temperature difference becomes small.

5.2.3.4. Gravity Cascade Heat Exchanger

Gravity induced flow of particulate solids over the heat exchanger surfaces provides mixing similar to fluidization. The degree of enhancement of the surface-to-wall heat transfer coefficient is dependent for a given particle-gas combination on the average contact time as discussed in Section 5.2.2.3, and shown by Fig. 5-3.

A conceptual Cascade heat exchanger arrangement characterized by Fig. 5-7 was evaluated for ICF power conversion system operating conditions. To enhance mixing, a staggered tube, horizontal array was selected, similar to that employed for the immersed tube fluid-bed concept. In this case, however, horizontal staging is not appropriate and the once-through boiler tubes pass back-and-forth, ascending countercurrent to the Li_2O flow as indicated in Fig. 5-7. This heat exchanger arrangement has the advantage that it can operate in either gas or vacuum conditions. Its characteristics will be calculated for both cases.

INPUT Li$_2$O DISTRIBUTOR 1170 K

STEAM OUT

BOILER TUBE ARRAY

FEED WATER IN

770 K Li$_2$O DISCHARGE
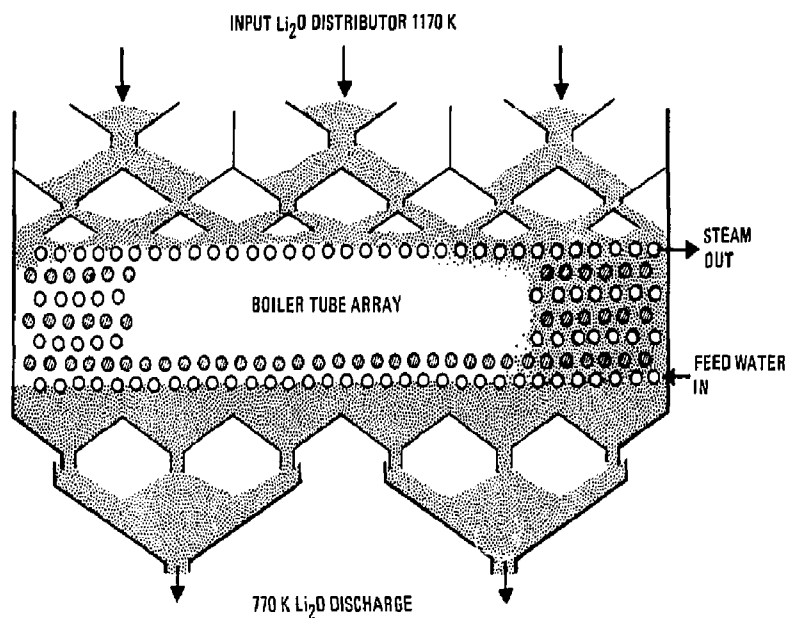
ADVANTAGES

● GOOD BED MIXING.

● RELATIVELY HIGH SURFACE HEAT TRANSFER COEFFICIENT.

● CAN OPERATE UNDER VACUUM CONDITIONS.

DISADVANTAGES

● UNIFORM PARTICLE DISTRIBUTION OVER LARGE FRONTAL AREA IS DIFFICULT.

● CLEANING Li$_2$O PLUGS IS DIFFICULT.

Fig. 5-7. Horizontal tube, Cascade gravity-flow counterflow heat exchanger.

The configuration shown by Fig. 5-7 indicates cascade flow-splitter type distributors, intended to provide uniform flow conditions over all of the surfaces while maintaining relatively short residence times for the hot Li_2O granules in transit from the ICF chamber.

Referring back to Section 5.2.2.3, it is necessary to define the bed depth s, and contact time t_s for a specific heat exchanger in order to evaluate the surface heat transfer coefficient $\bar{\alpha}$ [Ref. 5-1(b), Eq. 16]. The remaining parameters are defined by the Li_2O particle bed characteristics and properties as evaluated in Sections 5.2.2.1 and 5.2.2.2.

For the horizontal, staggered tube array, the effective agitated bed depth is defined as half of the bed thickness flowing between tubes. The apparent thickness thus is with respect to the tube surface on either side, *i.e.*,

$$ s = \frac{P_t - d_t}{2} , $$

where

$$ P_t = \text{tube pitch spacing, cm (Table 5-2)} $$
$$ d_t = \text{tube diameter, cm.} $$

Further, the contact time in the case of cross flow over the tube surfaces is estimated by

$$ t_s = \frac{d_t}{u_B} . $$

where u_B = bed flow velocity, cm/s.

The open flow area for Li_2O flow over the tube array, A_B is give by:

$$ A_B = (P_t - d_t)(N_t - 1)\ell_t \qquad cm^2 , $$

5-30

where

N_t = number of tubes in the frontal array,

ℓ_t = horizontal tube pass length normal to flow, cm

To avoid an iterative solution, the number of tubes was fixed by selecting the feedwater flow per tube. The frontal tube length per pass ℓ_t was fixed at 4.5 and 2.5 meters for the 4 and 2.5 cm tubes, respectively. This leaves only the total tube length to evaluate using the contact time t_s to determine $\bar{\alpha}$.

$$u_B = \frac{Li_2O \text{ Volume Flow}}{A_B} = \frac{2.48 \times 10^6 \, \text{cm}^3/\text{s}}{A_B \, \text{cm}^2}, \qquad \text{cm/s}$$

The value of t_s estimated using u_B and the tube diameter is used to determine $\bar{\alpha}$ from Fig. 5-3 for both one atmosphere helium gas pressure and for Li_2O flow under vacuum conditions.

Overall tube length was calculated summing the boiler and superheater length determined for the selected feedwater flow, number of tubes and overall Li_2O-to-steam conductance U for the boiler and superheater sections, respectively. Table 5-5 lists the resulting heat exchanger characteristics for the two selected tube diameters and feedwater flow rates. The parenthetical values shown in Table 5-5 were calculated for vacuum conditions of Li_2O transport. Vacuum conditions penalize heat exchanger area requirements are about a factor of three greater as compared to using helium interstitial gas due to the latter's improved thermal coupling of heat exchange surfaces with the Li_2O granules.

These conceptual results are optimistic both in contact time t_s for cascade type flow over tubes and in the agitated bed calculational model as noted by Muchowski Ref. 5-1(b). For example, stagnation buildup of Li_2O on the leading edge of tubes is not explicitly accounted for in these results. Also, the time of flight of an average particle past one projected tube diameter at the throat area for t_s needs experimental adjustment. However, despite these assumptions, the results are indicative of achievable performance and geometry of practical heat exchangers for a power conversion

5-31

TABLE 5-5

CASCADE POWER CONVERSION SYSTEM

Horizontal Tube, Li$_2$O Gravity Flow, Once-Through Boiler Concepts

- Li$_2$O Granule Gravity Flow Across Staggered Tubes in Counterflow 0.1 MPa (10^{-5} MPa)
- Steam Rate 4.2×10^6 kg/hr @ 15.1 MPa Through Double Wall Boiler Tubes

Tube Diameter, (cm)	4	4	2.5	2.5
Number of Tubes	2100	1700	6200	5000
Tube Length, (m)	112 (372)	132	46 (174)	56
Surface Area, (m^2)	29,000 (97,000)	28,000	22,000 (84,000)	21,000
Frontal Area, (m^2)	470	370	500	400
Li$_2$O Flow Area (m^2)	93	80	115	92
Number of Passes per Tube	25 (83)	30	20 (70)	23
Tube Array Height (m)	2.2 (7.2)	2.6	1.1 (4.0)	1.3
Overall Heat Transfer Coefficient, Li$_2$O-to-Water, Evaporator Section, (W/m^2-K)	395 (103)	368	476 (120)	489
Feed Water Flowrate (g/s, Tube)	570	700	190	240

system of the required rating. More detailed design studies and cost estimates are necessary to determine whether a significant advantage exists for the 2.5 or 4.0 cm diameter boiler tubes.

To confirm that the tube pitch spacing and therefore frontal flow area is adequate to allow flow of the rated Li$_2$O granule volume, the limiting Li$_2$O flow rate was estimated, treating the tube-to-tube space as an orifice. From Ref. 5-12, Fig. 4.1, using D_o (minimum orifice width) of 0.75 cm (from Table 5-2) and particle diameter $D_p = 0.02$ cm.

$$\frac{D_o}{D_p} = 38 = n_r \; .$$

From Ref. 5-12, Fig. 4.1,

$$\frac{W_A \sqrt{\tan \beta_A}}{C_w C_o \sqrt{g} \rho_B D_p^{2.5}} = 3500 \; ,$$

where (Ref. 5-12, Eq. 4.9)

$W_A =$ solids flow rate, g/s ,

$\beta_A =$ angle of repose ,

$\rho_B =$ bulk density of the bed, g/cm^3 ,

$C_w = \left(\dfrac{n_r - 1}{n_r}\right) + 0.5 \left[1 - \left(\dfrac{n_r - 2}{n_r}\right)^2\right]$.

$C_w = 0.974$,

$g =$ gravitational constant, 980.6 cm/s .

From Ref. 5-12, Fig. 4.3, assuming an equivalent hopper angle of $\theta = 60°$ for flow between cylindrical tubes @ $D_o/D_p = 38$, $C_o = 1.1$.

For uniform spheres $\beta \simeq 24°$ and $\tan \beta = 0.466$.

Calculating weight flow W_A with average bed bulk density $\rho_B = 1.09$ g/cm^3, $W_A = 10.61$ g/s for a circular orifice 0.74 cm dia.

Per unit area, $W_A = 24$ g/s cm^2 = 240 kg/s m^2.

For 2700 kg/s Li$_2$O flow, the required area is

$$A_B = \frac{2700 \, \text{kg/s}}{240 \, \text{kg/s} \, \text{m}^2} = 11.3 \; \text{m}^2 \; .$$

All cases provide 7 to 10 times this required minimum area. Li$_2$O flow rate can be controlled by discharge orifices beneath the heat exchanger tube array.

5.2.3.5. Vertical Li$_2$O Tube-Flow, Shell Steam Side Heat Exchanger

A heat exchanger concept was considered in which the Li$_2$O granules flowed through vertical tubes exchanging heat to coolant or steam generation on the shell-side. Figure 5-8 conceptually describes this approach.

Li$_2$O flow was estimated using the above model from Ref. 5-12 (Fig. 4.1). A rod-like heat transfer model was used to determine the length L (Ref. 5-13, Eq. 20.41):

$$\frac{T_w - T_0}{T_w - T_1} = 0.692 \, e^{-5.78[(\pi k L)/(W \, C_p)]} \, ,$$

where

T_w = Constant wall temperature, K

T_0 = Li$_2$O exit temperature, K

T_1 = Li$_2$O inlet temperature, K

k = γ_{so} bed conductivity (Fig. 5-1)

W = mass flow Li$_2$O, g/s

C_p = Li$_2$O particle heat capacity, 2.78 J/g K (Ref. 5-6)

By calculating W based on flow through a vertical tube (Ref. 5-12, Fig. 4.1), a required tube length L can be calculated. For this case, a constant wall temperature of boiler saturation temperature was used.

Since λ_{so} is greater with 500 μm diameter microspheres, only 500 μm dia Li$_2$O was considered for this concept. Calculated flow for 4 cm diameter tubes was 223 g/s per tube. At 0.1 MPa the calculated length is 39 m and

$$N_t = \frac{2.7 \times 10^6 \, \text{g/s}}{223 \, \text{g/s}} = 12,000 \text{ tubes} \, .$$

Total area $A_{HX} = 20000(39).126 \, \text{m}^2/\text{m}_t = 59,000 \, \text{m}^2$.

1170 K
Li$_2$O IN

STEAM OR
HEATED
HELIUM OUT

ADVANTAGES

- Li$_2$O PARTICLE FLOW GEOMETRY IS SIMPLE
  WITH FEW REGIONS FOR POTENTIAL HOLDUP

- UNIFORMITY OF Li$_2$O FLOW CAN BE
  REASONABLY ASSURED

- ACCEPTABLE TUBE–SIDE HEAT TRANSFER
  RATE

- CLEANUP OF Li$_2$O PLUGS STRAIGHT FORWARD

DISADVANTAGES

- SHELL–SIDE STEAM GENERATION
  PRESSURE IS LIMITED

- TUBE–TO–SHELL THERMAL EXPANSION
  DIFFERENCES DIFFICULT TO ACCOMMODATE

FEEDWATER
OR COOL HELIUM
INLET

Li$_2$O OUT
770 K

Fig. 5-8. Li$_2$O tube-side gravity-flow counterflow heat exchanger.

Under vacuum conditions of 10 Pa, calculated tube length is 2950 meters for 4 cm diameter tubes and 735 meters for 2.5 cm tubes. Neither of these can be considered feasible. This concept is not attractive at 0.1 MPa helium pressure and is infeasible under vacuum conditions.

5.2.3.6. Conclusions

A summary comparison of the heat exchanger concepts is presented by Table 5-6. Table 5-7 is a chart of summary statements. The most significant conclusion is that all three of the principle concepts are feasible and can result in practical designs. No clear recommendation has evolved from purely heat transfer considerations.

TABLE 5-6
CASCADE POWER CONVERSION SYSTEM
Summary

	Immersed Tube Fluid-Bed	Direct Contact Fluid Bed	Cascade Flow	
			W/He	Vacuum
Helium Pressure, MPa	>0.1	5.1	0.1	10^{-5}
Total Heat Transfer Surface Area, m^2	22,000	Not Applicable	22,000	84,000
Total Frontal Surface Area, m^2	510	200	500	500
Active Height, m	1.3	13	1.1	4.0
Helium Transfer Locks	Yes	Yes	Yes	No
Intermediate Heat Exchanger	No	Yes – with Steam Cycle Maybe - with Gas Turbine	No	No
Steam Cycle	Yes	Yes	Yes	Yes
Gas Turbine	Yes	Yes	Yes	Yes

TABLE 5-7
HEAT EXCHANGER CONCLUSIONS

- Fluid-bed concepts are self-distributing across frontal area.

  Cascade-flow concepts require mechanical distribution to minimize Li_2O volume.

- Fluid-bed transfer area not significantly different than Cascade-flow due to good agitation and short particle contact time.

- Vacuum heat exchanger heat transfer area is approximately three times the helium case.

- Direct contact requires high helium pressure and high pumping power.

- None of the heat exchanger concepts are infeasible except the vertical tubeside Li_2O concept under vacuum conditions.

- No clear recommendations from purely heat transfer considerations.

5.3. VACUUM TRANSFER LOCK ASSESSMENT

5.3.1. Introduction

Heat exchanger concepts which involve interstitial helium gas or helium fluidization gas require a transfer lock system through which to pass the Li_2O granules from the high vacuum reaction chamber to the heat exchanger system, and to return the cooled Li_2O to the reaction chamber. Conceptually, a transfer lock for this general function is not particularly unique. However, the very large volume transfer rate required at high proposed operating temperatures presents an interesting challenge.

5.3.2. System Description

Functionally, the transfer lock system must handle 2700 kg/s of Li_2O granules leaving the reaction chamber at 1170 K and 10 Pa. This corresponds to 2.5 m^3/s

volume rate. Figure 5-9 is a schematic showing major functional components of a transfer lock system. Not shown in the diagram are the surge tanks before and after each transfer lock,

The chamber discharge lock is evacuated in the empty state, then opened to the chamber to receive a charge of hot Li_2O granules. The lock is isolated and helium gas is introduced to the desired pressure. The lock is then opened, passing the granules to the heat exchanger system via surge tanks.

For return to the chamber, cooled granules are transferred into the lock under helium atmosphere. The lock then isolates and is pumped down to chamber vacuum. After reaching chamber pressure, the lock is opened to the chamber and the Li_2O flows into the chamber, again via a surge tank.

In order to use commercially available vacuum pumps, precoolers are required to cool the initially hot helium to acceptable pump inlet temperature. A receiver tank is provided to maintain vacuum pump discharge pressure at 0.1 MPa. If higher pressure is needed for the power conversion heat transfer system, a helium return compressor will be required as shown optionally. For the direct contact fluid bed, 5.1 MPa system pressure is required.

Conceptual sizing of system vessels was performed based on engineering judgment of reasonable lock cycle times. Assumed lock cycle step times (based on hot side sequence)

Pump down empty lock	120 sec.
Hot Li_2O transfer (fill)	30 sec.
Helium pressurization	10 sec.
Li_2O transfer out of lock	30 sec.
Total cycle	190 sec.

Allowing 30% clearance volume over Li_2O bed volume in each lock charge,

$$\text{Lock volume} = 2.5 \text{ m}^3/\text{s } (1.30)(190 \text{ s}) = 620 \text{ m}^3$$
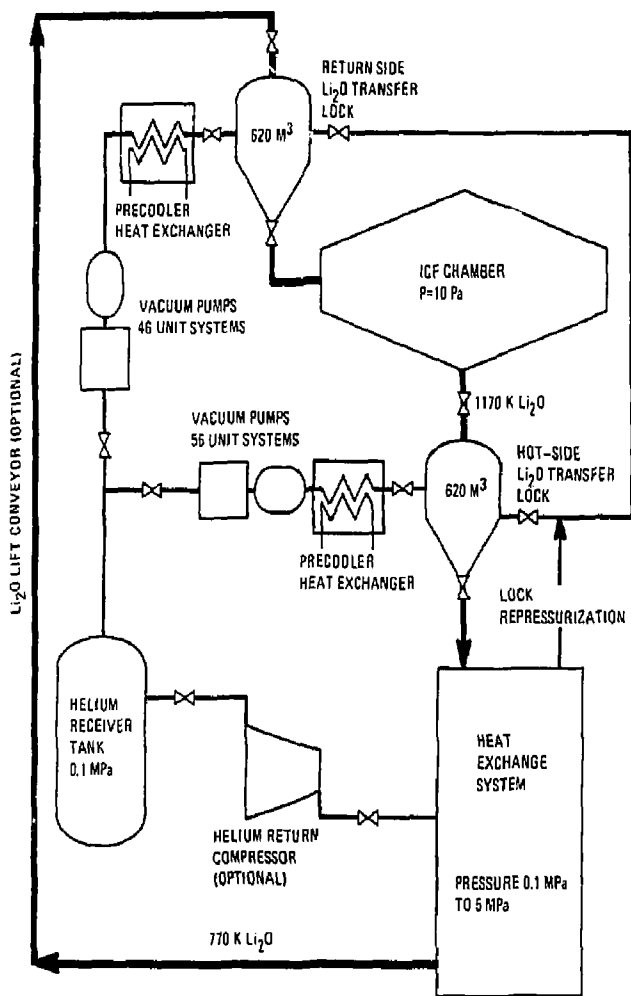
Fig. 5-9. Vacuum lock Li_2O transfer system schematic.

For a 120 sec pumpdown to 10 Pa of 620 m³, the required pump speed S is given by (Ref. 5-14, Fig. 1, Eq. 2):

$$S = \frac{F \times \text{Volume}}{\text{Time}} ,$$

where F = pumpdown factor.

For pumpdown to 10 Pa, $F = 10.3$

$$S = \frac{10.3(620 \times 10^3 \, \ell)}{120} = 5.3 \times 10^4 \, \ell/s \cong 3.2 \times 10^6 \, \ell/\text{min} .$$

Since the hot helium (1170 K) remaining in the transfer lock is precooled to 320 K before entering the vacuum pumping system, the required volumetric pump speed is reduced:

$$S_c = 3.2 \times 10^6 \, \ell/\text{min} \left(\frac{T_2}{T_1}\right) = 3.2 \times 10^6 \left(\frac{320}{1170}\right) = 8.7 \times 10^5 \, \ell \, \text{min} .$$

Recommended (Ref. 15) vacuum pumping units consist of two backing pumps and one booster as follows

     2   ES7500 Backing Pumps @ 7,800 ℓ/min each

     1   EH4200 Rotary Lobe Booster @ 81,000 ℓ/min

Number of hot side lock pump units required, based on backing pump capacity is

$$N_p = \frac{8.7 \times 10^5}{2(7800)} = 56 .$$

For the cold side, pump down volume is less due to the presence of the Li_2O granule charge during pumpdown (at 0.6 solid fraction in 2.5 m³ 's Li_2O volume)

$$\text{Volume} = 620 \text{ m}^3 - 190 \text{ s}(0.6) \ 2.5 \text{ m}^3/\text{s} = 335 \text{ m}^3 \ ,$$

Chamber temperature (Li_2O + helium) is 770 K, Li_2O return temperature.

$$S_c = \frac{10.3(335 \times 10^3)}{120} \left(\frac{320}{770}\right) 60 \text{ s/m} = 7.1 \times 10^5 \ \ell/\text{m} \ ,$$

$$N_p = \frac{7.1 \times 10^5}{2(7800)} = 46 \text{ units.}$$

5.3.3. Pumping Power Requirements

Installed motors on the vacuum pump units are:

2	ES7500 with 15 HP ea. =	30 HP
1	EH4200 with 10 HP =	<u>10</u> HP
	Total	40 HP per unit

Total installed HP = $(56 + 46)40 = 4080$.

The vacuum pumps are open to the lock and actively pumping 120 seconds of each 190 second cycle. The remainder of the time they are running against shutoff. Assume power drawn is 70% continuous of installed power.

$$\text{Vacuum pumping power} = 0.7 \ (4080 \text{ HP}) \ 0.746 \text{ kWhr/HPhr}$$
$$= 2.1 \times 10^3 \text{ kW}$$

For comparison, the isentropic pumping power was calculated for evacuation of the transfer locks. In this case, the calculation was performed stepwise over a number of pressure steps to account for the changing pressure ratio and helium mass flow rate. Total isentropic pumping power was calculated as 660 kW. This corresponds to an overall vacuum pumping efficiency of about 30% at 70% of installed horsepower.

For the direct contact fluid bed heat exchanger case, compression from the 0.1 MPa contactor pressure requires significant compression power. For this case, it is assumed that compression suction maintains the receiver at 0.1 MPa so the initial depressurization of the locks from 5.1 to 0.1 MPa is accomplished by venting the

locks to the receiver, bypassing the vacuum pumps. However, all of the gas must be recompressed to heat exchanger operating pressure.

Total compression mass flow rate is

$$\dot{m} = \frac{2.5\,\mathrm{m}^3/\mathrm{s}\,(1.3)\,5.1 \times 10^6\,\mathrm{N/m}^2}{2.08 \times 10^3 \mathrm{N-m/kg\ K}} \left[\frac{1}{1173} + \frac{0.4}{773} \right]\ .$$
$$= 10.9\,\mathrm{kg/s}\ .$$

At 85% efficiency, compression power is [Ref. 5-15. Eq. 9:53]

$$W_c = \frac{k\,N_s}{0.85(k-1)}\,\dot{m}RT_1 \left[\left(\frac{P_2}{P_1} \right)^{(k-1)/kN_s} - 1 \right]\ .$$

where

$$T_1 = 350\ \mathrm{K}$$
$$R = 2.08 \times 10^3\ \mathrm{N\text{-}m/kg\ K}$$
$$P_2 = 5.1 \times 10^6\ \mathrm{N/m}^2$$
$$P_1 = 0.1 \times 10^6\ \mathrm{N/m}^2$$
$$k = 1.66$$
$$N_s = \text{Number of compression stages}\quad 20.$$
$$W_c = 3.36 \times 10^7\ \mathrm{N\text{-}m/s} \equiv 36\ \mathrm{MW}$$

5.3.4. Conclusions

Table 5-8 summarizes the vacuum-to-helium transfer lock system evaluation. Although the large scale of the system is unique, the energy consumption is not unacceptable nor does it appear mechanically infeasible. It does present a technological challenge given the system cycle rate and the number and size of the equipment. Probably the aspect of greatest concern is whether the evacuation of helium from the bulk volume of 475 cubic meters of 200 to 500 μm Li_2O particles in 120 seconds from the cold-side transfer lock is feasible. Even assuming that it is distributed into

a number of smaller transfer changers, the small interstitial spaces between particles will limit the rate of evacuation. This could be self-defeating because as the time of evacuation increases, the volume of material to be evacuated continues to increase to maintain Li_2O throughput of 2.5 m^3/s. Experimental work is required to evaluate pumpdown rate from the particle bed of Li_2O granules.

<div align="center">

TABLE 5-8
ICF POWER CONVERSION SYSTEM

Mechanical Evaluation
Vacuum-to-Helium Li_2O Transfer Chambers
Li_2O Transfer rate 2700 kg/s

</div>

- Two Transfer Lock Systems Required

- Unit Chamber Volume Required: 3.2 m^3/s

- Cycle Time: 30 sec Li_2O transfer (fill)
  (Hot Side)   10 sec   He pressurize
                 30 sec Li_2O transfer
                 <u>120</u> sec   Pumpdown
                 190 sec   Total

- Chamber Volume: 620 m^3 Each lock
                                 (multiple units. 2 minimum)

- Vacuum Pumps Required:

     120 unit sets of: 2   ES7500 backing pumps
                                   7800 1/m, 15 hp ea.
     <u>   </u>
     56 hot-side   1   EH4200 booster pump
     45 cold-side   80.000 1/m. 10 hp.

- Space Requirements: 2 m×3 m×2 m each set
                           approx. 1200 m^3

- Power Required: 2,100 kW   for vacuum pumps to
                                0.1 MPa receiver pressure

                  36,000 kW   for recompression to
                                5.1 MPa fluid-bed contact Hx

5.4. GRANULE TRANSPORT AND SYSTEMS INTEGRATION

5.4.1. Introduction

In this section we present the mechanical design and integration of the granule transport system. We follow the path of the Li_2O granules after their removal from the chamber via the scoops described in Section 2.2, their transport through the vacuum locks and heat exchangers, and their return to the reaction chamber inlet and we evaluate transport options. We assess the physical space requirements for transport. heat transfer. and nuclear radiation shielding. We also present potential component configurations which integrate the functional and space requirements of the reaction chamber. heat exchangers, vacuum locks, and associated systems.

5.4.2. Granule Transport Options

The granule transport system provides the interface between the Cascade reaction chamber and the power conversion system. The objectives imposed on this system are stringent and require that it

- Adequately remove material from the chamber shelf
- Minimize transport power requirements
- Minimize Li_2O inventory in transit
- Minimize granule attrition during transport (e.g., via abrasion)
- Minimize temperature drop during transport
- Address concerns of bearing cooling and lifetime in a radiation environment.

Material transport options for achieving the above objectives are presented in Table 5-9. Of these, the belt, bucket, and screw conveyor are commercially available and could be extrapolated to Cascade requirements. The vibrator conveyor would require development. but its low throughput capacity might result in high capital cost. The use of a gas to lift Li_2O is a novel idea with some representation in the literature (Ref. 5-16). Its advantage is that for heat transfer in a helium medium, the helium fluidization itself might also provide the necessary lift. However. it would be

TABLE 5-9

MATERIAL TRANSPORT OPTIONS FOR CASCADE

Method	Comment
Belt conveyor	• Many bearings
	• Bearings hot in vacuum
	• Metal belt necessary
	• Lubrication concerns
Bucket conveyor	• Good but complex
	• Less bearings
Screw conveyor	• Abrasive — passive particle pressures
Vibrator conveyor	• Low capacity but no bearings or passive pressures
Gas lift	• No equipment necessary once through vacuum locks
Centrifugal throw system	• No equipment necessary

limited to use outside of the reaction chamber vacuum boundary.

The centrifugal throw system best satisfies the established objectives. It uses the angular momentum imparted to the granules by the rotating chamber to effect particle transport and thus would not require any additional equipment. It would, however, be limited to heights determined by limitations on the chamber rotational speed.

For the Cascade gravity flow vacuum heat exchanger described in Section 5.2, the throw system can supply adequate height at the reference chamber speed of 40 rpm. For vacuum heat transfer, it is the recommended option and is detailed below. For heat transfer in a helium medium, the height requirement on the throw system is dictated by the vacuum lock transfer system components presented in Section 5.3. The conceptual mechanical design integration of these systems is described below and indicates that. in a helium medium, the centrifugal system must be augmented by

5-45

an additional lift system. Since this lift function might also be incorporated into the heat transfer enhancement function of the helium gas, this option is the recommended auxiliary lift system.

5.4.3. Centrifugal Throw Granule Transport System

The transport of the Li_2O granules begins with their removal from the chamber shelf by the scoop. In the interest of efficiency, the particles should be removed from the shelf as nearly simultaneously as possible. (This is a factor in the scoop design.) This will tend to minimize particle collisions and result in a homogeneous and efficient stream trajectory. Note that a 20% loss of rim speed will result in a 36% loss of kinetic energy.

Figure 5-10 shows a plot of the trajectories of particles forced off the shelf at various points along a removal arc. A 20% loss of rim speed was assumed in this figure. There will be no convergent flows until the line of the first released particle's trajectory starts to re-enter the stream. At this point, major energy loss due to collisions may be important.

The reaction chamber-heat exchanger arrangement is shown in Fig. 5-11. The particle stream ejected from the loaded shelf by the control scoop will be directed along the throw duct and will be caught in the heat exchanger or transfer lock system as it starts to fall back. A vacuum type heat exchanger will be bottom controlled, and a heap will be continuously deposited on its top, flooding down and cooling until released from the bottom. Upon release, material will undergo a top controlled high speed flow across the main return to the chamber entry point. Its speed should be arranged to match the minimum chamber surface speed. It is thus a design objective to have a low height heat exchanger and a short axial dimension for the chamber to economize in the fall height required to keep the system running. This provides guidance to future heat exchanger design efforts.

A heat exchanger which uses helium to enhance heat transfer from the particulate requires that the material be locked out of and back into the vacuum. The complexities

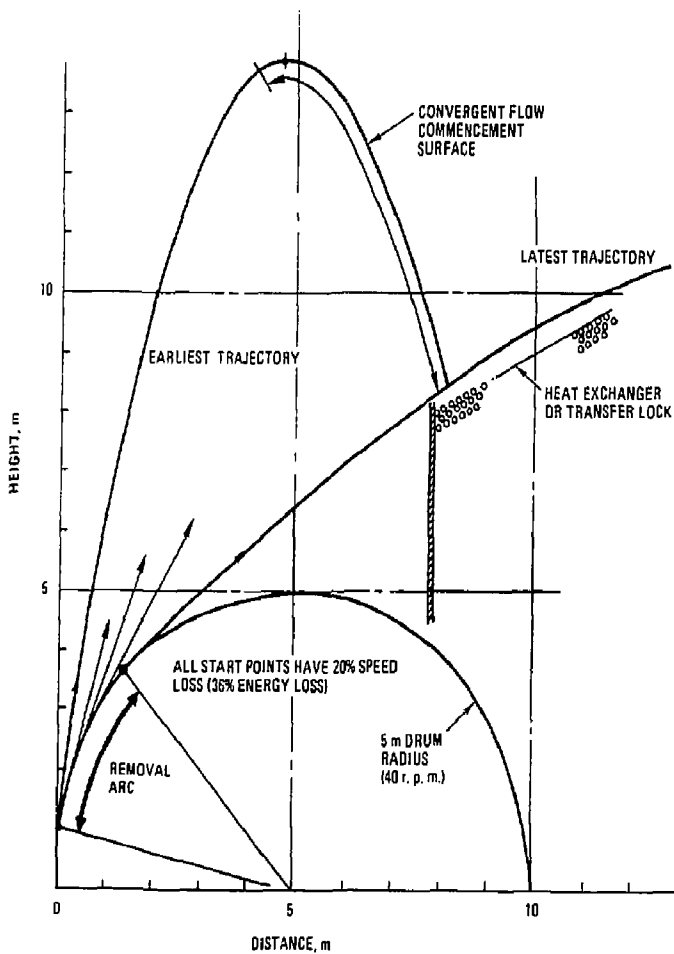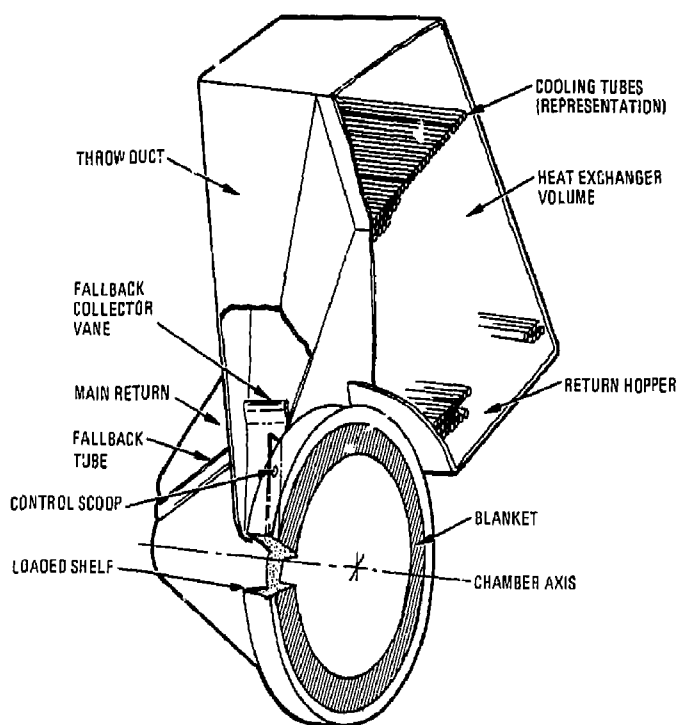*Fig. 5-10.* *Trajectory sketch of granules departing the chamber shelf via scoop action (non-optimized).*

Fig. 5-11. Reaction chamber — vacuum heat exchanger arrangement.

The figure is labeled with the following callouts:

- THROW DUCT
- FALLBACK COLLECTOR VANE
- MAIN RETURN
- FALLBACK TUBE
- CONTROL SCOOP
- LOADED SHELF
- COOLING TUBES (REPRESENTATION)
- HEAT EXCHANGER VOLUME
- RETURN HOPPER
- BLANKET
- CHAMBER AXIS

of this system are such that the simple throw and fall back transport system will suffice only inside the vacuum boundary. Thus the two heat exchange systems will look similar within the vacuum boundary, but the helium system will require additional transport outside the vacuum.

It is not expected that the material will move with zero error through its cycle. Opportunity exists for small quantities of material to randomly fail to complete a useful trajectory or to be poorly directed by the scoop. Even if design and experimental programs were to reduce this to a loss of better than one part per thousand, the volume loss rate would still be 10 m^3/hr. The throw box should have a collection vane at or near its base to gather any fallout and direct it to the chamber intake through the fallback tube. This should take care of most of the problem. However, an even less tractable residuum of a few cubic meters per day is still expected. The support rollers and drive seals must be protected from this material and the ring girder tracks will probably be continuously brushed. The floor of the vacuum room should be grilled and a sweeper system and hopper-and-drawer arrangement provided to handle the material loss.

5.4.3. Mechanical Design Integration

We now examine the physical space requirements and configuration of the components comprising the primary heat transport system of Cascade. Heat exchanger dimensions are as set forth in Section 5.2, vacuum transfer lock component dimensions are as presented in Section 5.3.

For vacuum heat transfer, the total height requirement on the throw system is that due to the heat exchanger and the distribution and collection plena above and below the heat exchanger. A conceptual component layout is shown in Figs. 5-12 and 5-13. The plena height are established by the 500 m^2 heat exchanger frontal surface area requirement and the angle of repose of the Li_2O granules.
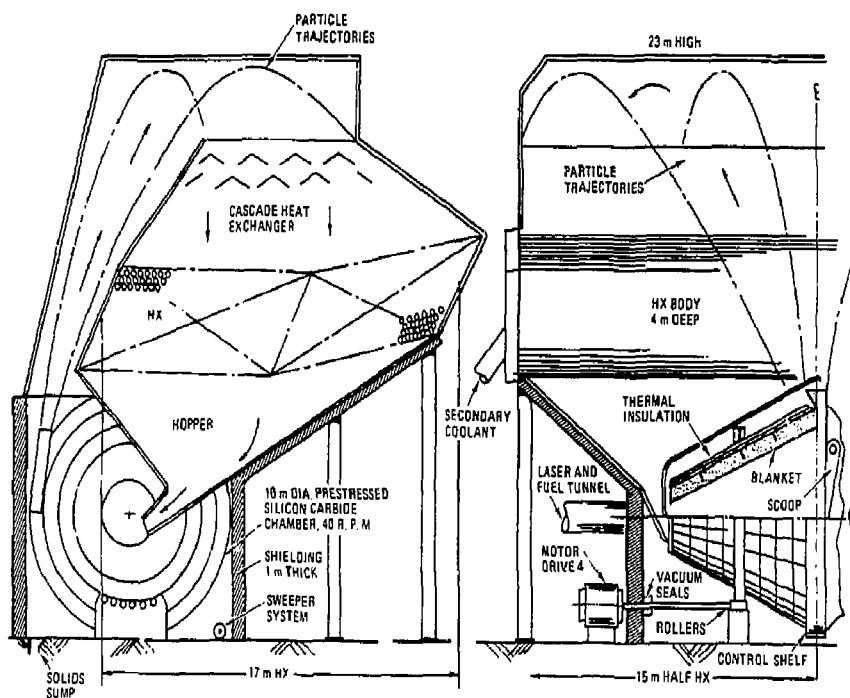
Fig. 5-12. Elevation views of an integrated Cascade reaction chamber and vacuum heat transfer heat exchanger system.
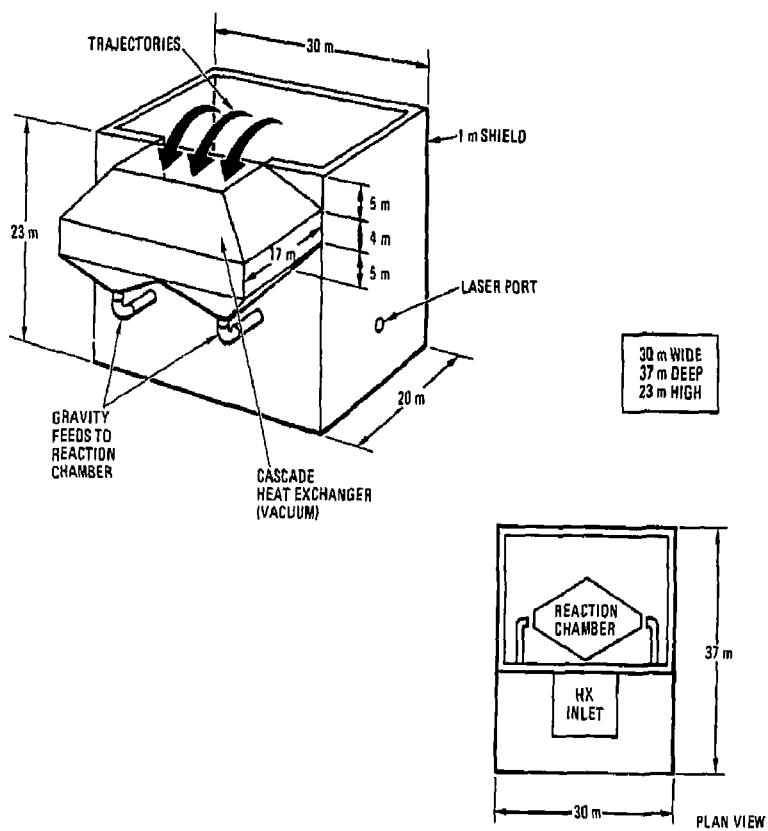
Fig. 5-13. Primary containment building layout for Cascade reactor with horizontal-tube Cascade-flow vacuum heat exchanger.

For the Cascade gravity flow vacuum heat exchanger, assuming frontal dimensions of 30 m width and 17 m depth, the plena height required for adequate distribution within the heat exchanger and transport back to the reaction chamber inlets are approximately 5 m each. These are combined with a 4 m heat exchanger active height and 3 m clearance for the particle trajectories for a total throw height requirement of 17 m. This can be provided by the 40 rpm chamber rotation speed if efficient use is made of the granule velocity. Alternately, the chamber speed can be increased to overcome losses in exit speed. The total vacuum boundary height is thus 23 m, assuming a 5 m radius reaction chamber and an additional 1 m for the granule exit shelf and ground clearance. These dimensions give a good indication of the size requirements of a Cascade reactor plant. Other configurations and system dimensions are certainly possible.

The configuration is not so straightforward with a helium heat transfer medium due to the vacuum lock system. An approximation for the total system height requirement can be obtained as follows. The hot and cold transfer locks are each approximately 10 m diameter. Since the reaction chamber and heat exchangers operate in a steady state, whereas the transfer locks operate in a batch mode, the four surge tanks must each also be of comparable dimension, 10 m diameter. Assuming 5 m distribution and collection plena heights above and below the heat exchanger, an additional 5 m height below the last surge tank for transport back to the reaction chamber inlets, 4 m height for valves, 3 m clearance for particle trajectories, and active heat exchange height requirements if all components were vertically stacked are 83 to 95 m. These heights would require chamber speeds of 77 to 82 rpm with 100% efficient use of the granule exit velocity. These speeds would be impractically high due to the centrifugal stresses which they would impose on the prestressing system and the increased "scatter" of the particle trajectories. Helium heat transfer must thus employ an auxiliary granule lift system.

If an auxiliary lift system is necessary, more compact (less height) component arrangements can be configured by using multiple lifts. Conceptual configurations are

shown in Figs. 5-15 to 5-16. System dimensions were established as presented above. Splitting the inlet surge system as shown in Figs. 5-15 and 5-16 saves about 10 to 12 m in height but requires additional cold transfer lock and surge tank. Compared to the vacuum heat transfer, the vacuum lock systems look formidable. However, with multiple lifts the physical dimensions are reasonable. Though other configurations are possible, the dimensions shown in Figs. 5-14 to 5-16 are representative of the building size requirements for the Cascade plant. As stated previously, it is conceivable that the lifts could be combined into the direct contactor heat exchangers, further decreasing their size. At present, from the systems integration perspective, we recommend vacuum heat transfer using the Cascade gravity flow heat exchanger.

References for Chapter 5

5-1. "Heat Exchanger Design Handbook, Volume 2, Fluid Mechanics and Heat Transfer." Hemisphere Publishing Corp., 1983 (a) Section 2.8.1, *Stagnant Packed Beds*, R. Bauer; (b) Section 2.8.3, *Packed and Agitated Beds*, E. Muchowski; (c) Section 2.8.4, *Fluidized Beds*, J.S.M. Botherill.

5-2. Kunii and Levenspiel, "Fluidization Engineering," Wiley, 1969.

5-3. J. Goodman *et al.*, "The Thermodynamic Properties of Helium," GA Technologies Report GA-A13400, October 1975.

5-4. Perry, Chilton, and Kirkpatrick, "Perry's Chemical Engineers' Handbook," 4th Ed., McGraw-Hill, 1963.

5-5. McAdams, "Heat Transmission," Third Edition, McGraw-Hill, 1954.

5-6. U.S. Department of Energy, "Materials Handbook for Fusion Energy Systems," Section B-E,p. 1.0, DOE/TIC-10/22.

5-7. J. Goodman *et al.*, "The Thermodynamic and Transport Properties of Helium," GA Technologies Report GA-A13400, October 1975.
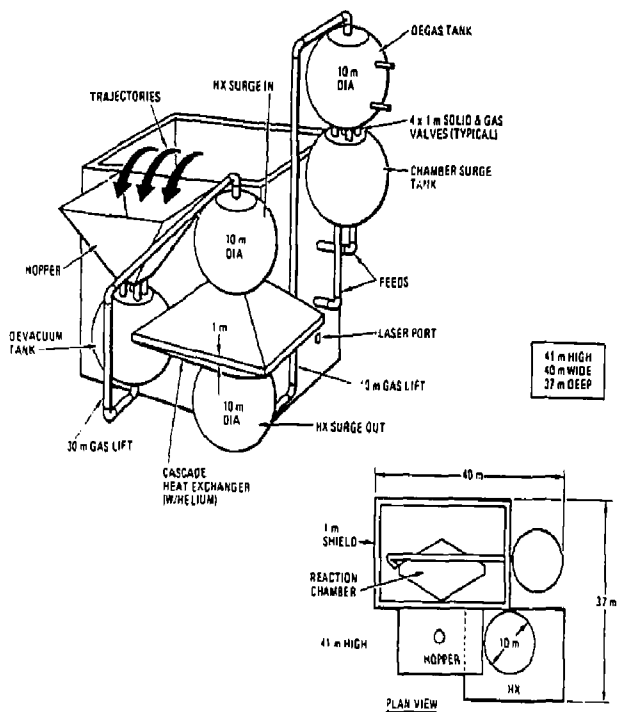
Fig. 5-14. *Primary containment building layout for Cascade reactor with horizontal-tube Cascade-flow helium heat exchanger and 3-min cycle vacuum transfer lock system.*
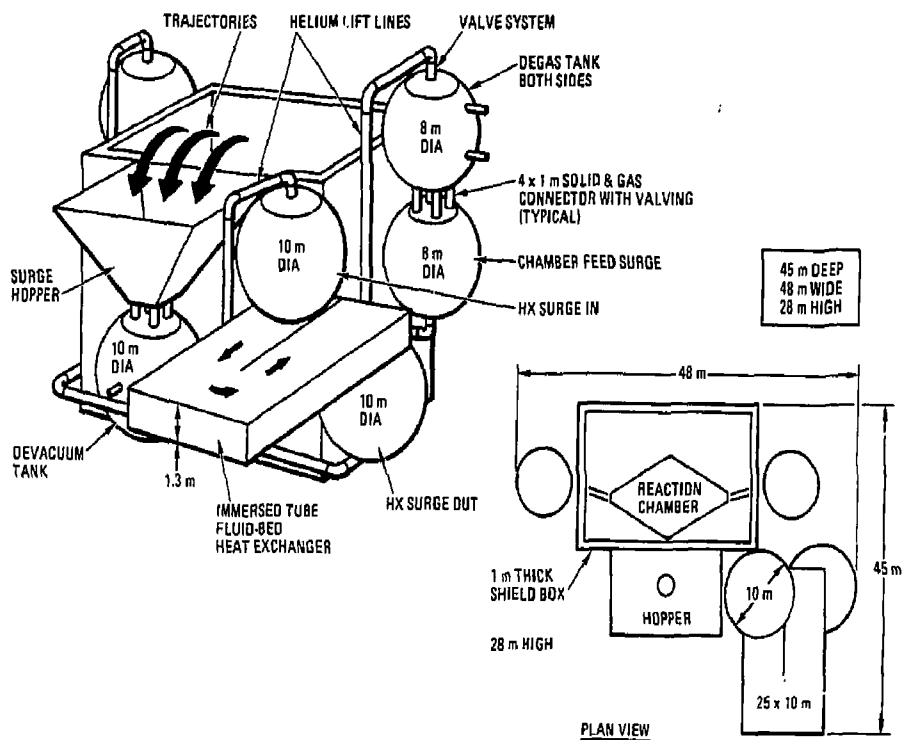
Fig. 5-15. Primary containment building layout for Cascade reactor with immersed-tube fluid-bed heat exchanger and 3-min cycle vacuum transfer locks with double feed/surge system.
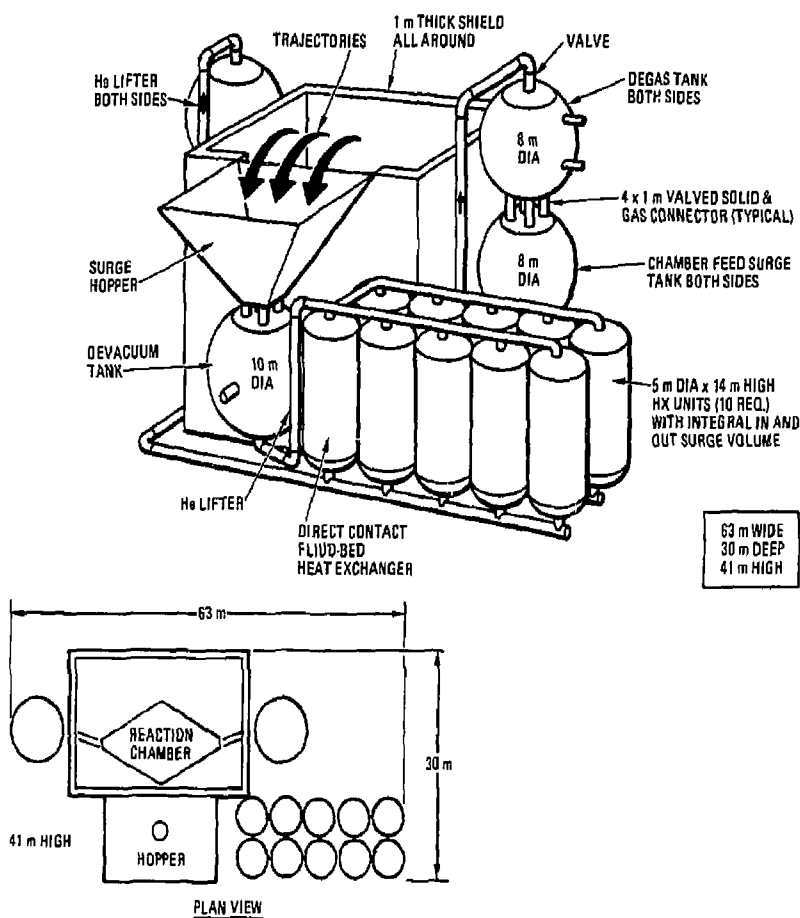
Fig. 5-16. Primary containment building layout for Cascade reactor with direct contact fluid-bed heat exchanger and 3-min cycle vacuum transfer with double feed, surge system.

5-8.   K. Tanaka, "International Conference on Radiation Effects and Tritium Recovery for Fusion Reactors." CONF. 750989, 1975.

5-9.   D.P. Carosella. Jr.. "Steam Generator Thermal Performance Model Verification by Use of Fort St. Vrain Nuclear Generating Station Test Data." *ASME* 79-WA NE-1, December 1979.

5-10. Keenan and Keyes. "Thermodynamic Properties of Steam." Wiley. 1936.

5-11. Fort St. Vrain Nuclear Generating Station. Updated Final Safety Analysis Report. Volume 1 of 7, Section 4.

5-12. Zeng and Othmer. "Fluidization and Fluid-Particle Systems." Reinhold. 1960.

5-13. Kern. "Process Heat Transfer." McGraw-Hill. 1950.

5-14. Edwards High Vacuum. Inc.. Personal communication and technical data sheets.

5-15. Young. "Basic Engineering Thermodynamics." McGraw-Hill. 1952.

5-16. J. Yerushalmi. "Flow Regimes II: High Velocity Fluidization." lecture prepared for short course on Fluidized Bed Technology. Department of Chemical Engineering. Stanford University. August 20. 1982.

References for Chapter 6

6-1. J. Robinson. Carborundum Company, vendor quotation to H.L. Schuster. January 1984.

6-2. Alcoa. High Purity Aluminum Cost Summary transmittal to G.R. Hopkins. April 1984.

6-3. Dow Corning Corporation. Nicalon SiC Fiber Product Cost Sheet, January 1983.

6-4. D.E. Schwarzer, "Quotes from Vendors — Current Price Schedules." GA Technologies Personal Communication, August 1980.

6-5. H L. Schuster. "Vendor Quotations — Energy Products Group." GA Technologies Personal Communication to J. Stanley, February 23, 1978.

6-6. Edwards High Vacuum, Inc., Telcon quotation to H.O. Winkler. December 19, 1983.

6-7. Richardson Engineering Services. Inc. *Process Plant Construction Estimating Standards.* San Marcos, CA. 1983.

6-8. 2240 MW(t) HTGR SC. C.

6-9. D.E. Schwarzer. "IHX Comparisons." GA Technologies Personal Communication. March 1980.

6-10. R.F. Bourque. "An Efficient, Low Temperature Steam Power Conversion System for Fusion Reactors." GA Technologies Report GA-A16783. June 1982.

6-11. C.F. McDonald. "The Nuclear Closed-Cycle Gas Turbine — A Utility Power Plant of the Future," GA Technologies Report GA-A15082. August 1978; also, *Energy International,* October 1978.

6-12. C.F. McDonald and C.P.C. Wong, "Closed Cycle Gas Turbine Applications for Fusion Reactors." GA Technologies Report GA-A16025. August 1980.

6-13. C.F. McDonald, GA Technologies, personal conversation. May 1984.

6. POWER CONVERSION SYSTEM EVALUA ION

6.1. INTRODUCTION

The Cascade concept offers the potential for a power-producing reactor which is inherently safe, environmentally attractive, simple, and highly efficient. Simplicity generally implies minimum cost and maximum reliability, whereas high efficiency generally implies higher capital cost and increased system complexity. Though the Cascade concept is inherently simple, it also offers the potential for very high blanket temperatures. It thus can potentially achieve both low cost and high efficiency. The sections below present a preliminary quantitative examination of the capital cost versus efficiency tradeoff. Capital cost evaluations of the Cascade reaction chamber and primary heat transport and exchange systems are presented in Section 6.2. Power conversion system options are explored in Section 6.3. A recommended reference power conversion system is developed consisting of technically simple vacuum heat transfer from moderate temperature (1170 K) Li_2O to a 43% net thermal efficiency steam cycle. A high temperature, high efficiency, but higher technical risk power conversion system option is also identified as an alternative, consisting of fluid-bed direct contact heat transfer from 1400 K Li_2O to helium gas driving a 49% net thermal efficiency closed cycle gas turbine (58% net efficiency with a Freon bottoming cycle).

6.2. CAPITAL COST ESTIMATES

This section presents a preliminary capital cost estimate of the components unique to the Cascade concept — the reaction chamber, heat exchangers, and the transfer lock system. The capital costs are based on the designs presented in Sections 2.2, 5.2, and 5.3 and are estimated on the basis of vendor estimates (Refs. 6-1 to

6-6) of unit costs per mass of material, scaled catalog prices (Ref. 6-7), and previous estimates of subcomponents scaled to Cascade conditions (Ref. 6-8).

A summary of the capital costs is presented in Tables 6-1 to 6-4, scaled to January 1984 constant dollars.

Inspection of Table 6-1 shows that the SiC tiles and SiC/Al composite prestressing tendons together cost $7.8M (including contingency), 60% of the total $13M chamber cost, and weight 38 MT. For comparison, a 2-1/4Cr - 1Mo steel chamber would weight 60 MT, and at a unit cost of $15/kg (machined and finished from rolled plate, Ref. 6-4), would cost $1.2M (including contingency), 25% of the total $5M installed cost. This increased cost of the ceramic chamber may be justified on the basis of its improved abrasion resistance, the elimination of active cooling requirements, and its low activation characteristics which allow for increased maintenance personnel access. In addition, if radiation damage is life-limiting for the chamber, the ceramic chamber would have a 30 year (full plant) life.

Tables 6-2 and 6-3 present the capital costs of the potential Cascade heat exchangers. Incoloy 800H is representative of a material with temperature capability up to 1000 K. Inconel 617 has a strength-at-temperature capability up to 1200 K. Both have been evaluated as the heat exchanger material in Ref. 6-9. Unit material costs for both I800H and I617 were obtained from Ref. 6-4. In the detailed breakdowns shown in Table 6-3, the heat exchangers were costed on the basis of both 2.5- and 4.0- cm feedwater tubes. In all cases, the 2.5 cm feedwater tube heat exchangers were of lower cost. This is mainly due to their lower heat exchange surface area requirements which in turn leads to less tube length and smaller shell dimensions. The costs in the summary of Table 6-2 are those of the 2.5 cm tube heat exchangers (where applicable). Smaller tubes could thus be expected to lead even lower costs and heat exchanger design tradeoffs .. .ld be examined. The direct contact heat exchanger was costed on the basis of Inconel 617 for both shell and internals. Its cost could be reduced by approximately 50% with an internal ceramic thermal insulator.

TABLE 6-1
PRELIMINARY CAPITAL COST OF CERAMIC (SiC)
CASCADE REACTION CHAMBER
($M, 1/84 Constant Dollars)

Material	Quantity (10^3 kg)	Unit Cost $/kg	Total Cost $M
1. Reaction chamber tiles silicon carbide	27	140	13.8
2. Prestressing tendons Nicalon SiC/Al composite	11	200	2.2
3. Thermal insulation			
Fiberfrax	1.0	1.5	0.0015
SiC/Al composite shroud	0.2	200	0.040
4. Support and drive girder			
SiC/Al composite	2.0	200	0.40
5. Ceramic shelf			
SiC	1.7	180	0.30
6. Internal vane			
SiC	7.3	270	2.0
Subtotal			**8.7**
7. Chamber drive			
24 rollers, 0.75 m dia. at $10,000 ea			0.24
4 motors, 150 kW ea at $12,000 ea			0.048
4 drive shafts, 0.05 m dia. at $15,000 ea			0.060
8. Assembly and installation fixture (Allowance)			0.15
9. Installation labor (Allowance)			0.55
Subtotal			**9.8**
10. Contingency (30%)			2.9
Total[a]			**$13.0**

[a]Not including:
   design and engineering
   management
   facility costs
   fees.

TABLE 6-2
PRELIMINARY CAPITAL COST SUMMARY
OF CASCADE HEAT EXCHANGERS
($M, 1/84 Constant Dollars)

	Incoloy 800H	Inconel 617
Immersed-tube, fluid bed	$27	$110
Direct contact, fluid bed		$120
Horizontal-tube, Cascade-flow		
in helium fluidization medium	$24	$100
in vacuum	$85	$360

or a cooled outer sleeve, which would allow the use of lower cost steels, *e.g.*, 2-1 4Cr - 1Mo ferritic steel or carbon steels.

The vacuum transfer lock system costs are summarized in Table 6-4. Chambers were sized to contain 0.1 MPa or 5.0 MPa pressure differentials as appropriate. The materials were I800H and I617 as above in high temperature applications and 2-1 2Cr - 1Mo at 770 K. Valve costs were scaled from previous estimates (Ref. 6-5) for Nuclear Class 2 qualified helium ball valves at 770 K. No adjustments for solids gating were made due to the lack of design detail. Vendor quotes were obtained for the pumps (Ref. 6-6). The system cost is dominated by the transport conveyor. Commercial screw conveyor costs (Ref. 6-7) were scaled to 3 m^3/sec volume flow rate and a 50 m transport distance and a cost factor of five for Nuclear Class 2 equipment at 800 K (Ref. 6-5). No major cost savings are expected for belt or bucket conveyors. The heat exchanger, helium receiver tank, and helium return compressor were scaled from similar components in Ref. 6-9.

The component and system capital costs developed in this section are used in the power conversion system option evaluation presented in the next section.

TABLE 6-3
PRELIMINARY CAPITAL COST BREAKDOWN
OF CASCADE HEAT EXCHANGERS
($M, 1/84 Constant Dollars)

Item	Quantity (MT)	Unit Cost I800H ($/kg)	Total Cost I800H ($M)	Unit Cost I617 ($/kg)	Total Cost I617 ($M)
A. Immersed-tube, fluid bed					
Case 1					
2.5 cm tubes	840	25	$ 21.0	110	$ 92.0
Shell	370	16	5.9	40	15.0
Total			$ **27.0**		$ **110.0**
Case 2					
4.0 cm tubes	1600	23	$ 37.0	100	$ 160.0
Shell	660	16	11.0	40	26.0
Total			$ 48.0		$ 190.0
B. Direct contact, fluid bed					
Shell	240			40	$ 9.6
Internals	45			40	1.8
Supports	3.9			16	0.06
Insulator (external)	220 (m²)		1300 m²		0.286
Subtotal					$ 11.7
Total (10 units)					$ 117.0
C. Horizontal-tube, Cascade flow					
in helium fluidization medium					
Case 1					
2.5 cm tubes	840	25	$ 21.0	110	$ 92.0
She"	170	16	2.7	40	6.8
Total			$ 24.0		$ 100.0
Case 2					
4.0 cm tubes	1700	23	$ 39.0	100	$ 170.0
Shell	210	16	3.4	40	8.4
Total			$ 42.0		$ 180.0
In vacuum					
Case 3					
2.5 cm tubes	3200	25	$ 80.0	110	$ 350.0
Shell	300	16	4.8	40	12.0
Total			$ 85.0		$ 360.0
Case 4					
4.0 cm tubes	550	23	$ 126.0	100	$ 550.0
Shell	270	16	4.3	40	11.0
Total			$ 130.0		$ 560.0

TABLE 6-4
PRELIMINARY CAPITAL COST SUMMARY
OF CASCADE VACUUM TRANSFER LOCK SYSTEM
($M, 1/84 Constant Dollars)

Hot-Side Material	Incoloy 800H	Inconel 617	Inconel 617
Transfer Lock Pressure	0.1 MPa	0.1 MPa	5.0 MPa
Hot-side transfer lock	$ 5.8	$ 16.7	$ 22.8
Hot-side surge tanks	1.2	1.9	14.8
Vacuum pumps	3.8	3.8	3.8
Precooler heat exchangers	0.3	0.3	0.3
Helium receiver tank	0.1	0.1	0.1
Helium return compressor	—	—	4.1
Cold-side transfer lock	5.6	5.6	12.9
Cold-side surge tanks	0.7	0.7	4.0
Li_2O transport conveyors	25.2	25.2	25.2
Piping, misc. valves and supports	3.5	3.5	3.5
Subtotal	$ 46.2	$ 57.8	$ 91.5
Contingency (15%)	6.9	8.7	13.7
Total	$ 53.0	$ 66.0	$ 105.0

6.3. POWER CONVERSION SYSTEM OPTIONS

In this section we survey various power conversion system options that could be used to convert the thermal energy of the Cascade reactor blanket to electricity. We compare several steam cycle and several helium gas turbine cycle options, using capital cost estimates and thermal efficiency to make an overall economic comparison. We recommend a steam cycle-based "reference design" and a helium gas turbine based "high efficiency option" for further design.

6.3.1. Introduction

The goals of the Cascade ICF Reactor Design study include development of a design that is simple and low cost, and that achieves high net efficiency operation. The power conversion system plays an important role in achieving these goals. The fusion energy produced in Cascade is deposited in the flowing Li_2O granule blanket as thermal energy -- heat. We have compared two options to convert this heat to electricity. The Rankine cycle using water as the working fluid ("steam cycle") and the Brayton cycle using helium ("gas turbine cycle").

For each of these two options we must consider the range of outlet temperatures that may be achieved in the Li_2O granule bed. The reference design is based on the assumption of a 1170 K Li_2O mixed mean outlet temperature. This "moderate temperature" is based on an upper Li_2O temperature limit of 1270 K and the assumption of flow mixing or flow zoning in the blanket. If flow mixing or zoning is not achieved, we may be limited to a "low temperature" design with 910 K Li_2O average outlet temperature (see Section 2.4). If higher Li_2O peak temperatures are allowed and excellent flow mixing is achieved, we may be able to use a "high temperature" design with 1400 K average outlet temperature. Use of a SiC granule protective layer on the blanket (see Section 3.2) may allow still higher outlet temperatures. We have considered low and moderate temperature designs for the steam cycle option, and moderate and high temperature designs for the gas turbine cycle option.

In addition, for each of the above combinations, we have evaluated the trade-off between vacuum transport of the Li_2O through the heat exchangers and helium transport. Helium transport improves the heat transfer and allows smaller, cheaper heat exchangers, but requires use of a vacuum lock system to transport the Li_2O in and out of the reaction chamber.

The list of options is shown on Table 6-5. The purpose of this scoping evaluation is to compare the overall relative system economics of the various power conversion system options to select the most attractive approach for more detailed design.

6-7

TABLE 6-5

TABLE 6-5
CASCADE POWER CONVERSION SYSTEM OPTIONS

	Power Cycle	Li₂O Temperature[a]	Secondary Coolant Temperature[b]	Li₂O Transport Medium
1.a	Steam	Moderate	Moderate	Vacuum
b.	"	"	"	Helium
c.	"	Low	Moderate or low	Vacuum
d.	"	"	"	Helium
2.a.	Gas Turbine	Moderate	Moderate	Vacuum
b.	"	"	"	Helium
c.	"	High	High	Vacuum
d.	"	"	"	Helium

[a]Low ~910 K Li₂O; Moderate ~1170 K Li₂O; High ~1400 K Li₂O

[b]Low ~610 K steam; Moderate ~810 K steam or 1130 K Helium; High ~1350 K Helium.

6.3.2. Steam Cycle

The steam cycle is an extensively developed, fully commercialized technology that can very effectively utilize steam temperatures up to ~820 K, giving thermal efficiencies of ~43%. The steam generator designs presented in Section 5.2 are based on delivering 810 K steam. The average Li₂O temperature assumed was 1170 K so there is capability for still higher steam temperature, but experience has shown there is little incentive to utilize it. The steam generator, piping, and turbine costs increase dramatically at higher temperature and component reliability drops. This experience has shown that it is best to utilize a large Li₂O-H₂O temperature difference to reduce the steam generator size and cost. Similarly, at these temperatures, use of multiple reheats is of little benefit. The power cycle chosen is shown on Table 6-6.

The cycle was developed using the code STMC, developed by GA Technologies (Ref. 6-10). It can analyze steam power cycles with zero to three reheats, six to eight

TABLE 6-8
MODERATE TEMPERATURE STEAM CYCLE

Li_2O temperatures, in/out, K	1170/770
Type	Superheat: no reheat
Peak pressure	16.5 MPa
Peak temperature	811 K
Steam extractions	7
Condensing temperature	305 K
Moisture extractions	1
Power conversion net thermal efficiency	0.429

steam extractions. and moisture extractions. Realistic pressure drops and temperature differentials are included. as is a correction for turbine efficiency drop due to moisture. The code has been benchmarked to an existing power plant to within 0.05 efficiency percentage points.

The moderate temperature steam cycle option uses an Incoloy 800H steam generator. It may be used with vacuum or helium transport of the Li_2O through the heat exchanger. Using the cost data developed in Section 6.2. the cost data shown on Table 6-7 was generated which shows a small cost advantage for helium transport. No temperature degradation in the vacuum lock system was assumed and its power requirements are small so the efficiency of the two systems is the same.

If we are unable to achieve flow mixing or flow zoning of the Li_2O. the mixed mean outlet temperature will drop to 910 K. To keep the Li_2O flow rate to reasonable levels. we would lower its inlet temperture as low as possible within the constraints of LiOH formation. about 610 K. There are two ways to accommodate the lower Li_2O temperatures. We can increase the heat exchanger area and cost. use a smaller Li_2O-to-H_2O temperature difference. and retain the same moderate temperature steam cycle. Alternately. we can keep the same heat exchanger area. and drop the temperature and efficiency of the steam cycle. The characteristics of a low temperature steam cycle are shown on Table 6-8.

TABLE 6-7
MODERATE TEMPERATURE STEAM CYCLE
COST AND PERFORMANCE

	Vacuum Transport	Helium Transport
Heat exchanger		
Material	Incoloy 800H	Incoloy 800H
Cost	$85M	$24M
Vacuum lock -- cost	0	$51M
Total cost	**$85M**	**$75M**
Efficiency	42.9%	42.9%

TABLE 6-8
LOW TEMPERATURE STEAM CYCLE

Li_2O temperatures, in/out	810 610 K
Type	Saturated vapor
Peak pressure	6.4 MPa
Peak temperature	553 K
Steam extractions	6
Condensing temperature	305 K
Moisture extractions	3
Power conversion efficiency	0.340

Both the low and moderate temperature steam cycles can be used with the temperature Li_2O option and both may use helium or vacuum transport of the Li_2O in the steam generator. The heat exchange area and cost of the steam generator be scaled from the data in Section 6.2 on the basis of the Li_2O-to-H_2O temperature difference. The vacuum lock cost may be scaled from the Li_2O flow rate by adjusting component diameters and volumes. The results are shown on Table 6-9

TABLE 6-9

LOW TEMPERATURE Li₂O STEAM CYCLE
COST AND PERFORMANCE

	Moderate Steam Temperature		Low Steam Temper: 'ure	
	Vacuum	**Helium**	**Vacuum**	**Helium**
Heat exchanger				
Material	─────────────Incoloy 800H ───────────			
Cost	$ 170M	$ 48M	$ 85M	$ 24M
Vacuum lock cost	–	102M	–	102M
Total cost	$ 170M	$ 150M	$ 85M	$ 126M
Efficiency	42.9%	42.9%	34.0%	34.0%

6.3.3. Gas Turbine Cycle

Gas turbine cycles are also a well developed and fully commercialized technology, but primarily for open cycle application. Closed cycle gas turbines are still in a developmental state, although significant successful experience has been achieved in Europe (Ref. 6-11). Gas turbine cycles can use effectively the high temperatures that fusion is capable of delivering (Ref. 6-12). With a turbine inlet temperature of 1300 K a closed cycle gas turbine could deliver ~47% net efficiency. Addition of a bottoming cycle to the gas turbine could boost this to ~55%. The limiting factor in using closed cycle gas turbines at high temperatures to achieve high efficiency is the heat exchanger. These become very expensive at high temperature and cause a temperature drop between the heat source and the turbine. Use of large heat exchange surface areas to minimize this ΔT results in still higher costs.

The direct contactor heat exchanger avoids these concerns. Although presently expensive, it need not have large internal pressure differentials. It allows the helium temperature a very close approach to the maximum Li₂O temperature. The direct

contactor does require vacuum locks in the Li_2O transport system and raises concerns about Li_2O dust and $LiOH$ vapor transport into the turbine.

We have investigated two gas turbine cycles for use on Cascade. The moderate temperature cycle uses the same Li_2O temperatures as the moderate temperature steam cycle. The direct contactor allows a turbine inlet helium temperature of 1130 K (see Section 5.2). An Inconel 617 heat exchanger and vacuum locks are needed which are expensive. Both are areas where innovative design could result in future cost savings. If we can achieve still higher Li_2O temperatures, higher efficiencies may be possible with a high temperature gas turbine cycle. A ceramic direct contactor would be needed. The gas turbine cycle characteristics are shown on Table 6-10.

TABLE 6-10
GAS TURBINE CYCLES FOR CASCADE

	Moderate Temperature	High Temperature
Li_2O temperatures, in/out, K	1170/770	1400/770
Pressure, MPa		
Turbine inlet	5.1	5.1
Compressor inlet	2.0	2.0
Precooler temperatures, in/out, K	570/300	570/300
Power conversion efficiency	42%	49%
Efficiency with Freon bottoming cycle	50%	58%

These characteristics may be combined with the costs developed in Section 6.2 to get performance estimates for the gas turbine systems. Because of the large temperature drop associated with nondirect contactor heat exchangers, we have not included the vacuum transport option. It is possible that use of very high temperature blanket materials such as the SiC protective layer discussed in Section 3.2, and use of ceramic heat exchangers could make a vacuum transport gas turbine cycle attractive. This is discussed further in Section 6.3.5 below. The performance of the helium transport gas

6-12

turbine cycle systems is summarized in Table 6-11. Again, the heat exchanger and vacuum lock costs have been scaled to reflect different areas, diameters, and volumes.

TABLE 6-11
GAS TURBINE CYCLE PERFORMANCE

	Moderate Temperature	High Temperature
Direct contactor		
Material	Inconel 617	SiC
Cost	$ 121M	$ 196M
Vacuum locks	84M	53M
Total cost	$ 205M	$ 249M
Efficiency	42%	49%
Efficiency with bottoming cycle	50%	58%

6.3.4. Economic Comparison

To compare the performance of the various options. we must compare capital cost and efficiency. We have done this by listing all the capital cost increments for the various options relative to the reference moderate temperature steam cycle vacuum transport option. We have converted the differences in cycle efficiency to an equivalent capital cost by assuming the difference in electricity production is worth 50 mills kWh. the plant operates at 70% capacity factor. the capital recovery period is 30 years (plant life). and the effective cost of capital to the utility is 12% (public utility). Note that to compare on an equal basis. we must include indirect capital costs. These are assumed to be 85% of direct costs. The results of this economic evaluation are shown on Table 6-12. The gas turbine cycles with bottoming cycles are not included. Previous experience has generally indicated that the additional capital cost of the bottoming cycle counterbalances the increased efficiency it adds, resulting in approximately a break-even (Ref. 6-13). Similarly. the capital cost of the steam turbine system and the g turbine system were assumed to be the same.

6-13

TABLE 6-12
CASCADE POWER CONVERSION SYSTEM COST SUMMARY

Option	Efficiency	Additional Capital Cost[a] (Direct + Indirect) ($)	Additional Capital Cost[a] Equivalent of Efficiency ($)	Net Extra Cost[a] ($)
1. Moderate temperature Li$_2$O, moderate temperature steam cycle, vacuum transport (reference)	43%	—	—	—
2. Moderate temperature Li$_2$O, moderate temperature steam cycle, helium transport	43%	-18.5M	0	-18.5M
3. Low temperature Li$_2$O, moderate temperature steam cycle, vacuum transport	43%	-157M	0	-157M
4. Low temperature Li$_2$O, moderate temperature steam cycle, helium transport	43%	-120M	0	-120M
5. Low temperature Li$_2$O, low temperature steam cycle, vacuum transport	34%	0	-584M	-584M
6. Moderate temperature Li$_2$O, moderate temperature, gas turbine cycle, helium transport	42%	-222M	-73M	-295M
7. High temperature Li$_2$O, high temperature gas turbine cycle, helium transport	49%	-303M	-511M	-208M

[a]Relative to reference design

6.3.5. Conclusions

A number of interesting and very useful conclusions can be drawn from this preliminary comparison of Cascade power conversion system options. First, relative to the reference option, the use of a helium transport system results in a capital cost savings of $19M. This is at the expense of greatly increased complexity. We believe that detailed design and costing of the vacuum lock system will result in cost increases and thus recommend that the vacuum transport system be retained as the reference system.

Flow mixing or zoning of the Li_2O increases outlet temperature by $260^\circ C$. This is worth $120 to $157M on capital cost and thus is well worth working toward. If flow mixing cannot be achieved, it is better to use larger heat exchangers and vacuum transport at a cost of $157M rather than to operate with lower efficiency at an equivalent capital cost of $584M. At the low temperature conditions the relative penalty of using vacuum heat exchangers is increased to $37M. We still believe this penalty is worth the improvement in system simplicity.

The moderate temperature gas turbine cycle results in a small decrease in efficiency and an increased capital cost due to the need for high temperature materials in the heat exchanger and vacuum lock. This results in a net overall penalty of $295M.

If high temperature can be achieved, the gas turbine system can achieve net thermal efficiencies of 50% to 60%. Effective cost savings of $208M can result. This gives strong incentive to pursue this goal, but the present system concept using a direct contactor and vacuum locks greatly increases system complexity and technical risk.

On the basis of these conclusions, we make the following recommendations for the Cascade power conversion system. Retain the moderate temperature, steam cycle, vacuum transport option as the reference design. This system is simple, uses proven power conversion system materials and technology, and offers reasonably high efficiency.

The high temperature gas turbine cycle is exciting and offers the potential for very high efficiency. We recommend that some additional scoping work be done to determine if a self-consistent system can be assembled that uses a SiC blanket layer to get high peak outlet temperatures and ceramic heat exchangers to avoid the need for a vacuum lock system. If this is possible, and if preliminary performance and cost estimates look favorable, the high temperature gas turbine system could make an attractive advanced power conversion system for Cascade.

7. ACKNOWLEDGMENTS